THE UNIVERSITY OF
WARWICK

AUTHOR: **Azadeh Khajeh Alijani** DEGREE: **Ph.D.**

TITLE: **Deterministic and stochastic dynamics of multi-variable neuron models: resonance, filtered fluctuations and sodium-current inactivation**

DATE OF DEPOSIT: .....

I agree that this thesis shall be available in accordance with the regulations governing the University of Warwick theses.

I agree that the summary of this thesis may be submitted for publication.

I **agree** that the thesis may be photocopied (single copies for study purposes only).

Theses with no restriction on photocopying will also be made available to the British Library for microfilming. The British Library may supply copies to individuals or libraries. subject to a statement from them that the copy is supplied for non-publishing purposes. All copies supplied by the British Library will carry the following statement:

> "Attention is drawn to the fact that the copyright of this thesis rests with its author. This copy of the thesis has been supplied on the condition that anyone who consults it is understood to recognise that its copyright rests with its author and that no quotation from the thesis and no information derived from it may be published without the author's written consent."

AUTHOR'S SIGNATURE: .....

USER'S DECLARATION

1. I undertake not to quote or make use of any information from this thesis without making acknowledgement to the author.
2. I further undertake to allow no-one else to use this thesis while it is in my care.

DATE SIGNATURE ADDRESS

.....

.....

.....

.....

.....

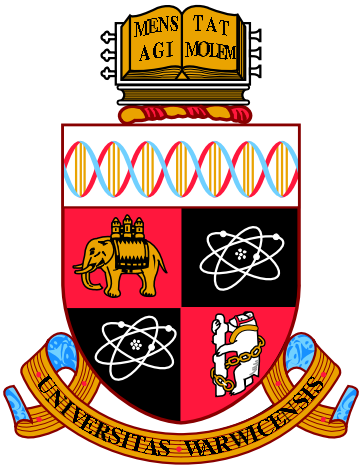

Deterministic and stochastic dynamics of multi-variable neuron models: resonance, filtered fluctuations and sodium-current inactivation

by

Azadeh Khajeh Alijani

Thesis

Submitted to the University of Warwick

for the degree of

Doctor of Philosophy

Mathematics

January 2011

THE UNIVERSITY OF WARWICK

Contents

List of Figures

Acknowledgments

I would first of all like to thank my supervisor Claude Baesens for her constant support and inspiration.

I am indebted to Magnus Richardson for all his great encouragement, advice and support throughout my PhD. I have been hugely fortunate to have him as my supervisor.

Thanks also go to Yulia Timofeeva for suggesting the RF neuron model (Chapter 2), for her collaboration and many helpful discussions.

I am grateful to Stephen Coombes for many helpful discussions on the RF neuron model and Carlo Laing for careful reading of the initial draft of Chapter 2 before being published.

Special thanks to my family, in particularl my sister Maryam, for their ever-present support and encouragement.

I would like to thank my friends at Warwick for good times we had together.

This PhD was funded by a Warwick Postgraduate Research Fellowship and an Overseas Research Students Award.

Declarations

I Declare that, to the best of my knowledge, the material contained in this thesis is original and my own work except otherwise indicated, cited, or commonly known. Chapter 2 is published in *Physical Review E* **80**: 5, 051922 (2009), and Chapters 3 and 4 is submitted.

Abstract

Neurons are the basic elements of the networks that constitute the computational units of the brain. They dynamically transform input information into sequences of electrical pulses. To conceive the complex function of the brain, it is crucial to understand this transformation and identify simple neuron models which accurately reproduce the known features of biological neurons. This thesis addresses three different features of neurons.

We start by exploring the effect of subthreshold resonance on the response of a periodically forced neuron using a simple threshold model. The response is studied in terms of an implicit one-dimensional time map that corresponds to the Poincaré map of the forced system. Qualitatively distinct responses are found, including mode locking and chaos. We analytically find the stability regions of mode-locking solutions, and identify the transition to chaos through period-adding bifurcations. We show that the response becomes chaotic when the forcing frequency is close to the resonant frequency.

Then we will consider an experimentally verified model with realistic spike-generating mechanism and study the effect of filtered synaptic fluctuations on the firing-rate response of the neuron. Using a population density method as well as an efficient numerical method, we find the steady-state firing rate in two limits of fast and slow synaptic inputs and present the linear response theory for the firing rate of the model in response to both time-dependent mean inputs and time-dependent noise intensity.

Finally, a novel model is introduced that incorporates threshold variability of neurons. We determine the modulation of the input-output properties of the model due to oscillatory inputs and in the presence of filtered synaptic fluctuations.

Chapter 1

Introduction

It is well known that neurons transform external stimuli into trains of electrical pulses referred to as spikes. Understanding the mechanisms by which neurons respond to stimuli, how neurons encode properties of input signals into their output spike trains, and what affects this encoding of information are still key topics of research in computational neuroscience. Theoretical analysis and computational modeling provide useful tools to answer these questions. The Hodgkin-Huxley model is the starting point of the neuron modeling. It is the base for detailed neuron models which can include numerous ion channels, synaptic fluctuations, and many other characteristics to produce the biophysical behavior observed in real neurons. The Hodgkin-Huxley model is also a reference model for the derivation of simplified neuron models such as the family of integrate-and-fire models.

The purpose of this thesis is to apply mathematical tools to neuron models to examine the response of neurons to stimuli, in particular, to periodic and stochastic forcing. I present the work in self-contained chapters, each dealing with

a specific question.

Here, the Hodgkin-Huxley model, detailed and simplified neuron models, and synaptic current models are briefly reviewed. Before turning to the Hodgkin-Huxley model, I need to give some information on neuronal structure and electrical properties.

1.1 Membrane potential and electrical properties of neurons

A neuron is composed of the cell body (soma), dendrite and axon. The soma and axon initial segment are largely responsible for when and how to produce action potentials. Dendrites, similar to a receiver device, are able to receive signals, and the axon acts as a sender of signals to other neurons. Axons terminate at synapses through which electrical or chemical signals transfer to another neuron [37].

Like all cells, around a neuron is a membrane separating its internal and external environment and on which are embedded ion channels. Inside and outside of the neuron are a variety of ionic species with different concentrations between inside and outside of the membrane, causing a potential difference across the membrane. The concentration of sodium outside the neuron is greater than inside, and that of potassium is greater inside the neuron. Because of this potential difference, ions can flow into or out of the cell through ion channels and generate ionic currents.

Without any input current, the neuron is at resting potential (the flow of ions into and out of the neuron balances each other). This potential is regulated by opening and closing of ion channels [59]. At resting potential, the inside of the membrane has a polarization (around -65 mV), so that if an input current causes a

positive change in the membrane potential, it is called *depolarizing* current and the corresponding process is depolarization. Similarly, an input that makes negative changes in the membrane potential is a *hyperpolarizing* current and the process is hyperpolarization.

During depolarization, if the membrane potential reaches a specific level (known as a threshold level), an action potential occurs which is fast (around $1-2$ ms duration), followed by a hyperpolarization returning it to the resting potential.

1.2 Neuron models

The cell membrane is full of ion channels and pumps which are embedded in the lipid bilayer shape of the membrane [37]. Each channel has special conductivity for transmitting ions and may just transmit selected ions. These channels are often sensitive to voltage changes and may respond to these changes by opening and closing their entrance gates. Furthermore, the semipermeable cell membrane separates charges (due to the difference in ions concentration) along its inside and outside surface and acts as a capacitor [59]. Therefore, an electrical model that describes the cell membrane can be considered as a capacitor in parallel with a resistor (not necessarily ohmic). The membrane current, then, satisfies

$$C\frac{dV}{dt} + I_{ion} = I_{app}, \tag{1.1}$$

where V is the membrane potential (inside potential minus outside potential), C is the membrane capacitance, I_{ion} is the total amount of the current passing through all ionic channels, and I_{app} is the applied current (either external or

synaptic current). The total ionic current can be described as

$$I_{ion} = \sum_k I_k, \tag{1.2}$$

where sum is over all ion channels. While the dynamics of each individual channel is stochastic, the large number of channels allows to describe them as below: the component I_k which passes through channel k, can be written as

$$I_k = g_k(V - E_k), \tag{1.3}$$

where g_k is the conductance of channel type k and E_k is the reversal potential of the channel. At reversal potential, the direction of the current flowing through the channel changes. It should be noted that conductance g_k is not constant and for most channel types depends on the membrane voltage and time. The current of those channels which have constant conductance is called *leakage* current and is defined by $g_L(V - E_L)$. The leakage current is also called *passive* current and the others are called *active* currents.

One of the most important discussions is about the dynamics of channels, and that how their passing currents depend on the membrane potential and time. Hodgkin and Huxley [68] are famous in studying the behavior of ionic currents and their model is still an important reference model for the derivation of other simple models.

1.2.1 Hodgkin-Huxley model

Hodgkin and Huxley [68] obtained a model for membrane potential by performing experiments on the giant axon of the squid. This model is briefly reviewed here. From the previous section, the membrane potential satisfies Eq. (1.1). The basic

and the main ionic currents that Hodgkin and Huxley considered were sodium (Na^+) and potassium (K^+) currents, and other ionic currents were included in the leakage current. The Hodgkin-Huxley (HH) model satisfies

$$C\frac{dV}{dt} = -g_L(V - E_L) - g_{Na}(V - E_{Na}) - g_K(V - E_K) + I_{app}, \tag{1.4}$$

where all parameters have the same biophysical meaning as mentioned before. Using the experimental data, they derived the following equation for the ionic conductance

$$g_K = \bar{g}_K n^4, \text{ and } \ g_{Na} = \bar{g}_{Na} m^3 h, \tag{1.5}$$

where $\bar{g}_K$ and $\bar{g}_{Na}$ are maximum conductance of the corresponding ion channel and n, m, and h are gating variables in the interval [0,1]. Each gating variable is responsible for activation (turning the current on) or inactivation (turning the current off), e.g., n is the activation variable of potassium and $m(h)$ is the activation (inactivation) variable of the sodium current. Activation and inactivation gates define the state of the ion channel and control the flow of current. The dynamics of each gating variable satisfies

$$\frac{dw}{dt} = \alpha_w(V)(1 - w) - \beta_w(V)w, \quad w = n, m, \text{or } h, \tag{1.6}$$

where α_w and β_w are empirical functions of V, see Appendix B. In order to get a better understanding, a simple implication of Eq. (1.6) is as below. Assuming that each gate has only two possible states as open or closed and w be the probability that the gate is open, then α_w and β_w describe, respectively, the rate at which the gate become open and closed. It is also conventional to write Eq. (1.6) as

$$\tau_w(V)\frac{dw}{dt} = w_\infty(V) - w, \tag{1.7}$$

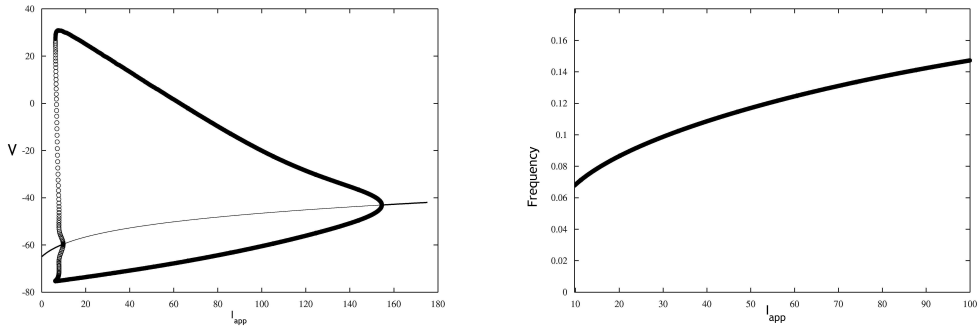

(a) (b)

Figure 1.1: Bifurcation diagram (a) and frequency-input curve (b) of the HH model under constant input I_{app}. (a): bifurcation diagram as a function of constant input current showing fixed points (lines) and limit cycles (circles) of the model. (b): frequency of the limit cycles of the model revealing Type II excitability.

where $\tau_w = [\alpha_w + \beta_w]^{-1}$ is the time constant of w and $w_\infty = \alpha_w/[\alpha_w + \beta_w]$ is the final (steady-state) value of w for a particular voltage.

Due to different time constants of these gating variables, if an input is strong enough, it makes an action potential (depolarization, crossing threshold, hyperpolarization, and recovery to rest) or even trains of action potentials. All the events in an action potential are determined by the systems gating variables.

The excitable properties of neurons can be determined by their firing-rate responses to constant input. A neuron has Type II excitability, if increasing input current causes repetitive action potentials (periodic responses) with a non-zero frequency. The transition from quiescence to periodic firing occurs via a Hopf bifurcation [78]. The HH model with standard parameters has Type II dynamics. This can be seen in Fig. 1.1 representing the bifurcation diagram (left panel) and the fiirng rate (right panel) of the HH model. As can be seen, periodic responses emerge with finite frequency when excitable state looses stability via a

Hopf bifurcation (circles in the left panel). Type I neurons make this transition via a saddle-node on invariant circle bifurcation [78] and repetitive action potentials emerge at arbitrary low frequency. An example of Type I neurons is Moris-Lecar model which will be introduced later.

1.2.2 Conductance-based neuron models

The action potential mechanism of the HH model provides a good description of the electrophysiological properties of the giant axon of the squid. However, cortical neurons in vertebrates exhibit much richer electrophysiological properties than the squid axon [59]. This is mostly because of the existence of a large variety of different ion channels [102, 87]. In this case, *conductance-based* neuron models are used which have the same structure as the HH model. The membrane voltage of these neurons satisfy Eqs. (1.1)-(1.3) and the conductance of a typical ion channel k follows the form of

$$g_k = \bar{g}_k m^{i_k} h^{j_k}, \tag{1.8}$$

where i_k is the number of activation gates and j_k is the number of inactivation gates. The gating variables m and h, also, satisfy Eq. (1.6).

An important model of the conductance-based family is Wang-Buzsáki (WB) model [160] used to model hippocampal and neocortical fast-spiking interneurons. Its dynamics is defined in Appendix B.

Although in conductance-based models, each variable has a well-defined biophysical meaning and even could be measured experimentally, the governing dynamics is a high-dimensional nonlinear ordinary differential equation and is difficult to analyze. Therefore, it is important to find methods of simplifying conductance-

based neuron models which will enable us to understand better the dynamics of single neurons and neuronal networks. Since the HH model, several reduction models [88, 49, 122, 119, 143, 145, 1, 83] based on different time scales of the gating variables (slow and fast dynamics) have been introduced. In [88, 143, 145], a reduction model is proposed by assuming that the sodium activation variable, m is an instantaneous function of V and the linear combination of the slower gating variables, h and n remain approximately constant during the time evolution. A more systematic reduction was also given by Kepler et al., [1, 83] by considering the instantaneous sodium activation variable and using the fact that the h and n variables have similar time scales. Their method is called *equivalent potentials* which reduces the HH model to a two dimensional model. Other two-dimensional reduction models of the HH equations are Moris-Lecar [119] and FitzHugh-Nagumo [49, 122] models. In the next sections, we describe these models.

1.2.3 The slow-fast model

The slow-fast model of the HH equations is based on two observations [88, 143]. One that the sodium activation variable m is fast ($\tau_m(V)$ is small relative to $\tau_h(V)$ and $\tau_n(V)$), therefore m can be replaced by its steady-state value m_∞ in Eqs. (1.4) and (1.5). The other assumption is that h and n satisfy a linear relationship as $n = b - rh$, where b and r are constants and depend on the input current. Therefore, if one substitutes $(b-n)/r$ instead of the h variable in Eqs. (1.4) and (1.5) the following two-dimensional fast-slow system can be obtained

$$\begin{aligned} C\frac{dV}{dt} &= -\bar{g}_{Na}m_\infty^3\big((b-n)/r\big)(V-E_{Na}) - \bar{g}_K n(V-E_K) - I_L + I_{app}, \\ \tau_n(V)\frac{dn}{dt} &= n_\infty(V) - n, \end{aligned} \tag{1.9}$$

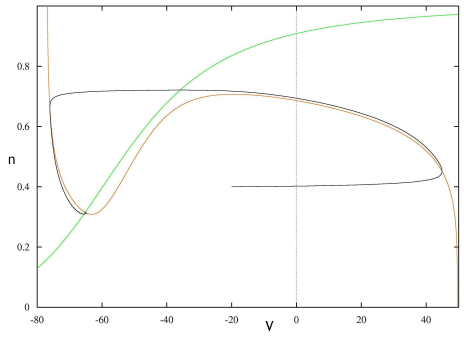

Figure 1.2: Phase portrait of the excitable slow-fast (V, n)-system given in (1.9) for $I_{app} = 0$.

where $I_L = g_L(V - E_L)$ is the leakage current. In Fig. 1.2, a phase portrait of the slow-fast (V, n)-system is shown. The V-nullcline (red line) has a cubic shape and the n-nullcline (green line) is n_∞, which is monotonically increasing function of V. As voltage is the fast variable and n is the slow one, the trajectories (a sample is shown with black line) are mostly horizontal except on the V-nullcline which is called the slow manifold [82]. We have chosen excitable regime ($I_{app} = 0$) where the fixed point is stable.

1.2.4 Equivalent potentials

Kepler et al., [83] proposed a method for comparing all gating variables with different time scales. As we mentioned before, a voltage-dependent gating variable $w \in \{m, r, h\}$ satisfies Eq. (1.7). The function $w_\infty(V)$ is monotonic and therefore invertible. Thus one can introduce a new variable V_w such that

$$w(t) = w_\infty(V_w(t)), \quad w = n, m, \text{or } h. \tag{1.10}$$

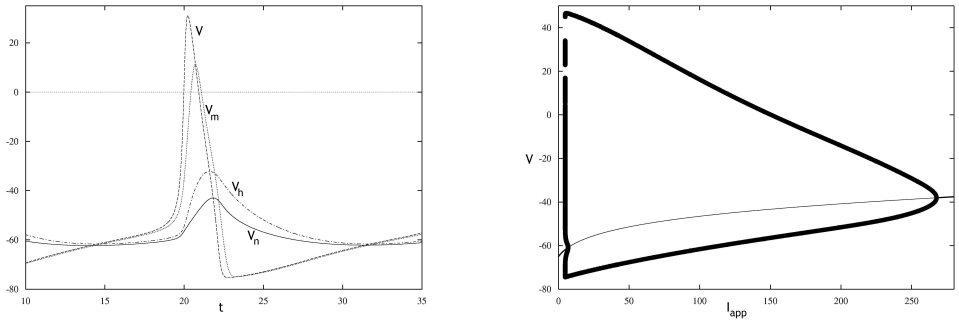

(a) (b)

Figure 1.3: The evolution and bifurcation diagram of the equivalent potential. (a): the evolution of the voltage and the equivalent voltages for the m, h, and n variables. (b): bifurcation diagram for (V, V_h)-system, which shows similar features as in the HH model, Fig. 1.1.

An equivalent dynamical system can be found such that each variable has the dimensions of voltage. This can be done by differentiating Eq. (1.10) with respect to time and using Eq. (1.7) which gives

$$\frac{dV_w}{dt} = \frac{w_\infty(V) - w_\infty(V_w)}{\tau_w(V)(dw_\infty(V_w)/dV)}, \quad w = n, m, \text{or } h. \tag{1.11}$$

Now, one can use Eq. (1.10) and replace the gating variable w in the HH equations with $w_\infty(V_w(t))$ and consider Eq. (1.11) instead of Eq. (1.7). No reduction has yet been made, the new system is entirely equivalent to the original HH model.

We can then plot and compare the amplitude and the time course of the responses of all the variables V_w and the membrane voltage V. Figure 1.3 (a) shows the equivalent potentials for the four gating variables in the HH model. As can be seen, V_m and V have similar temporal dynamics while V_h and V_n have similar time courses.

Therefore, the reduction in the HH model can be done by substituting

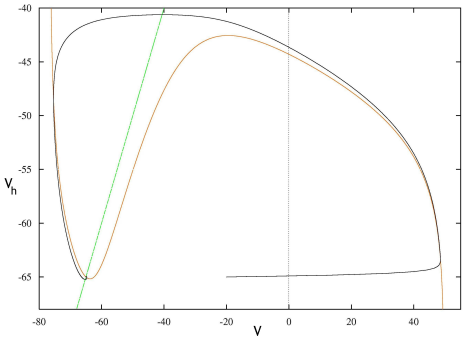

Figure 1.4: Phase portrait of the excitable system (1.12) for $I_{app} = 0$.

$V_m = V$ and $V_h = V_n$. This would results in the following (V, V_h)-system (the (V, V_n)-system gives similar result)

$$\begin{aligned} C\frac{dV}{dt} &= -g_L(V - E_L) - \bar{g}_{Na} m_\infty^3(V) h_\infty(V_h)(V - E_{Na}) \\ &\quad - \bar{g}_K n_\infty(V_h)(V - E_K) + I_{app}, \\ \frac{dV_h}{dt} &= \frac{h_\infty(V) - h_\infty(V_h)}{\tau_h(V)(dh_\infty(V_h)/dV)}. \end{aligned} \tag{1.12}$$

In Fig. 1.3 (b), we show the bifurcation diagram for the reduced model (1.12). There is a subcritical Hopf bifurcation at $I_{app} \approx 6.8$, then the system continues to oscillate on an extremely large applied current. Then at $I_{app} \approx 267$, the second Hopf bifurcation occurs. Note that this reduced model can not have any more fixed points than the full HH equations. Figure 1.4 shows the phase portrait of the (V, V_h)-system, where the V_h-nullcline (green line) is just $V = V_h$ and the V-nullcline (red line) has a cubic shape which is typical in many neural models and necessary in order to get oscillations [48]. We have considered the case that the fixed point is stable, on the left branch of the V-nullcline. Therefore, if a perturbation moves the initial condition to the right side of the middle branch, the trajectory (black line) go through a long excursion (an action potential) before

returning to the stable fixed point. increasing I_{app} moves the fixed point to the middle branch of the V-nullcline (the V_h-nulcline remains unchanged) where the system have oscillatory behavior.

1.2.5 Moris-Lecar model

It is known that the barnacle muscle fibers respond to a constant current injection with oscillatory voltage waveforms. Moris and Lecar [119] proposed the following two-variable model to describe the membrane potential of the barnacle muscle fibers

$$C\frac{dV}{dt} = -g_L(V - E_L) - \bar{g}_{Ca}m_\infty(V)(V - E_{Ca}) - \bar{g}_K x(V)(V - E_K) + I_{app},$$
$$\frac{dx}{dt} = \phi\lambda(V)\big(x_\infty(V) - x(V)\big),$$

where x is the fraction of open potassium channels and ϕ is the maximum rate for closing potassium channels. Also the calcium channels are assumed to respond to voltage changes rapidly, therefore the activation variable can be replaced by its steady state value $m_\infty(V)$ and

$$m_\infty(V) = \frac{1}{2}\Big(1 + \tanh\big(\frac{V - V_1}{V_2}\big)\Big), \tag{1.13}$$
$$x_\infty(V) = \frac{1}{2}\Big(1 + \tanh\big(\frac{V - V_3}{V_4}\big)\Big), \tag{1.14}$$
$$\lambda(V) = \cosh\big(\frac{V - V_3}{2V_4}\big). \tag{1.15}$$

Typical rate constant in the above equations are given in Appendix B. This model has Type I excitability. Figure 1.5 (a) shows a number of interesting feature in bifurcation theory. First that the stable and unstable fixed points coalesce at $I_c \approx 39.9$ and give rise to a saddle-node limit cycle bifurcation, leading to the creation of a stable limit cycle. In fact, the frequency of the limit cycle is zero at

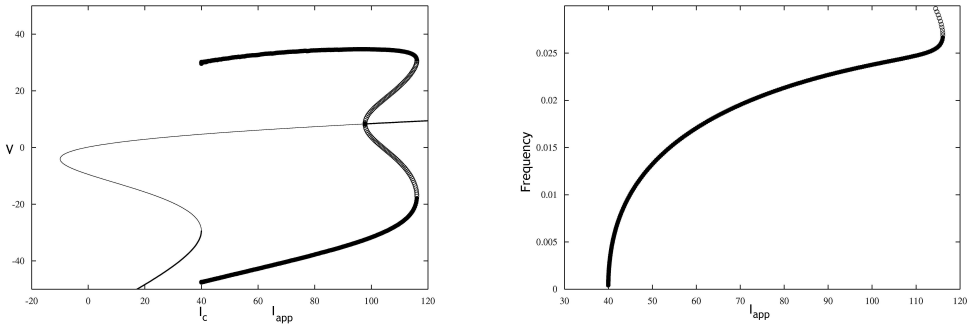

(a) (b)

Figure 1.5: (a): One-parameter bifurcation diagram showing fixed points and limit cycles of the Moris-Lecar model. (b): Frequency of both the stable and unstable limit cycles of the Moris-Lecar model.

the bifurcation point. This can also be seen in the right plot showing the frequency of the periodic orbits. Then for a small range of I_{app}, there is bistability between the upper unstable fixed point and the stable limit cycle (solid circles). Thereafter at $I_{app} = 97.79$, a Hopf bifurcation occurs such that unstable fixed point becomes stable and an unstable limit cycle (open circles) is created. Finally, the stable and unstable limit cycle coalesce which gives rise to a stable fixed point.

1.2.6 Fitzhugh-Nagumo model

The reduced (V, n)-system (also known as Rinzel reduced model) of the HH model described in Sec. 1.2.3, as well as the (V, V_h) system using the equivalent potential, Sec. 1.2.4, have a common feature in their nullclines. In both cases, the V-nullcline has a cubic shape and the nullcline of the recovery variable is monotonically increasing function of the voltage, see Figs. 1.2 and 1.4. The Fitzhugh-Nagumo model (FHN) [49, 122] captures the slow-fast dynamics of the HH model while

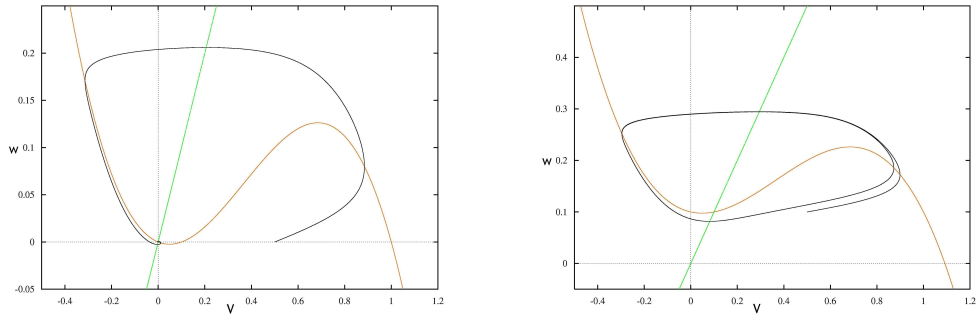

(a) (b)

Figure 1.6: Phase portrait of the FHN model. (a): the system is excitable, that is the fixed point is stable, $I_{app} = 0$. (b): the fixed point is on the middle branch of the V-nullcline (red) and the system is oscillating, $I_{app} = 0.1$. Other parameters are $\alpha = 0.1$, $\epsilon = 0.02$, and $\gamma = 1$.

keeping the cubic nature of the V-nullcline and the monotonic behavior of the slow recovery variable. Its dynamics is give by

$$\frac{dV}{dt} = f(V) - w + I_{app}, \tag{1.16}$$

$$\frac{dw}{dt} = g(V, w), \tag{1.17}$$

where $f(V) = V(V - \alpha)(1 - V)$ with $0 < \alpha < 1$, w is the slow recovery variable, and $g(V, w) = \epsilon(V - \gamma w)$ with $\gamma > 0$. The FHN model retains many of the qualitative features of the HH equations and have Type II dynamics. The planar FHN model can be studied using phase-plane techniques [82]. In Fig. 1.6, phase portraits of the system are shown. The nullclines of the FHN cross at one point (intersection of green and red curves). If the fixed point lies on the left (or right) branch of the V-nullcline (red curve), it is stable (panel (a)). If changing parameters (such as I_{app}) cause the fixed point passes through the minimum (maximum) value of the cubic curve, a Hopf bifurcation occurs, giving rise to a stable limit

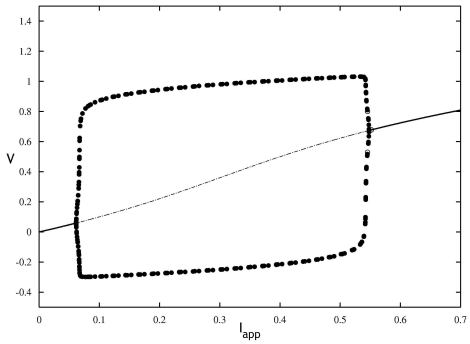

Figure 1.7: Bifurcation diagram of the FHN model, showing Hopf bifurcations at $I_{app} = 0.061$ and $I_{app} = 54$, the rest of parameters are as in the caption of Fig. 1.6.

cycle (panel (b)). This can be see in bifurcation diagram Fig. 1.7 where transition from excitable to oscillatory regime occurs via a Hope bifurcation.

With $\epsilon \ll 1$, the membrane voltage is the fast and w is the slow variable. Figure 1.6, also shows evolution of V and w. Starting with an initial condition on the right side of the middle branch (called threshold curve), V goes rapidly to the upper branch with w remaining nearly constant. While V stays on the upper branch, w increases slowly until it reaches the top of the upper branch. Then V returns to the lower branch and stays on this branch while w is decreased. If the fixed point lies on the lower branch (panel (a)), then w gradually returns to the fixed point. If the fixed point lies on the threshold curve, it is unstable. Therefore, the trajectory instead of returning to the fixed point moves to the right branch and repeats as before (panel (b)). This results in periodic action potentials.

1.2.7 Piecewise linear neuron models

In general, planar reduced models of the HH equations are described by two coupled nonlinear equations, one for voltage and the other for a gating variable. The

nullcline for the voltage equation has a cubic shape typical of many excitable systems. The difficulty of the analysis of such models in the presence of the cubic nonlinearity can be reduced by the introduction of the piecewise linear models (PWL) [112]. In PWL models, the cubic form of the V-nullcline is replaced by piecewise linear functions, allowing explicit solutions of many interesting problems. One of such model is McKean [112] model which is a piecewise linear version of the FHN model. Its dynamics satisfies Eqs. (1.16) and (1.17) with $f(V)$ given by

$$f(V) = \begin{cases} -V, & \text{for } V < \alpha/2, \\ V - \alpha, & \text{for } \alpha/2 < V < (1+\alpha)/2, \\ 1 - V, & \text{for } V > (1+\alpha)/2, \end{cases} \tag{1.18}$$

where $0 < \alpha < 1$. Another choice for $f(V)$ is [112] $f(V) = -V + \Theta(V - \alpha)$, where Θ is the Heaviside function. For the analysis of the former model see [33, 32] and for the latter one see [154, 155]. A third PWL model of FHN model is Pushchino model [82], proposed as a model for ventricular action potentials. The description of $f(V)$ for this model is given in Appendix B. A PWL model of the Moris-Lecar model has also been introduced [155] (showing Type I excitability). This model has been studied in [32, 33].

The family of integrate-and-fire models is other known example of reduced models with piecewise smooth dynamics. In such models, the neuron is considered to be isopotential and the difficulty of high dimensionality is reduced to a one-dimensional relation between voltage and current (see Secs. 1.2.8 and 1.2.10) or two-dimensional equations capturing effects of an additional subthreshold current (see Sec. 1.2.9). Their importance comes from the fact that they are computationally efficient and suitable for simulations of large networks of spiking neurons.

In the next sections, a review of these models are given.

1.2.8 Integrate-and-fire model

The leaky-integrate-and-fire (LIF) neuron model [21, 84, 156] is perhaps the simplest spiking model providing a good description of the neuron with passive membrane properties. Its dynamics is based on a single variable V and satisfies

$$C\frac{dV}{dt} = -g_L(V - E_L) + I_{app}(t), \tag{1.19}$$

where the parameters are the same as introduced previously and I_{app} can be external current and/or synaptic current from presynaptic neurons. Equation (1.19) is supplemented by a threshold voltage V_{th} above which a spike is registered and then the voltage is instantly reset to a subthreshold voltage V_{re}.

Despite the efficiency and popularity of the LIF neuron in the studies of neural coding, memory, and network dynamics [59], it suffers from the lack of a realistic spike generating mechanism. This weakness can lead to unrealistic responses, for example, in the coding of fast fluctuating inputs [52, 124].

Furthermore, its passive subthreshold behavior cannot capture the resonant behavior observed in certain neurons [72, 103] and in almost all biophysically detailed HH type neuron models [74, 72]. To describe more accurately these types of subthreshold behavior, the resonate-and-fire model can be used.

1.2.9 Resonate-and-fire model

The resonate-and-fire (RF) model was introduced by Izhikevich [76] and has been studied in [19, 138]. The spiking process of the RF model, similar to that of the IF model, includes threshold and resetting mechanism such that firing rates occur

instantaneously. However, it renders a neuro-computational property that is not present in the IF system [76]. It exhibits resonance in the sense that the membrane potential is more responsive near a given frequency. The RF dynamics is obtained by linearization of the HH equations around the steady-state potential and satisfies the following two-dimensional differential equations

$$\begin{aligned} C\frac{dV}{dt} &= -V(G+g_L) - I, \\ L\frac{dI}{dt} &= V - \frac{I}{g}. \end{aligned} \tag{1.20}$$

The exact derivation of the model is given in Chapter 2. Here, variable I represents a linearized ionic current with an equivalent electrical circuit composed of an impedance line with conductance g and inductance L in parallel with a conductance G (see the general case plotted in Fig 2.2). The dynamics of the RF system in response to periodic inputs is studied in Chapter 2.

1.2.10 Non-linear integrate-and-fire models

The IF and RF models can provide a good quantitative approximation of the HH model. However, they cannot produce a real spike as they do not have an explicit spike mechanism. In the following, another type of reduced models known as nonlinear IF models is introduced.

Non-linear integrate-and-fire (NLIF) neuronal models are one variable models that generalize the classic LIF model by including an additional nonlinear current with aiming to capture the voltage-dependent ionic current. The dynamics of the membrane potentials of the NLIF model satisfies

$$\tau_m \frac{dV}{dt} = f(V) + I_{app}(t), \tag{1.21}$$

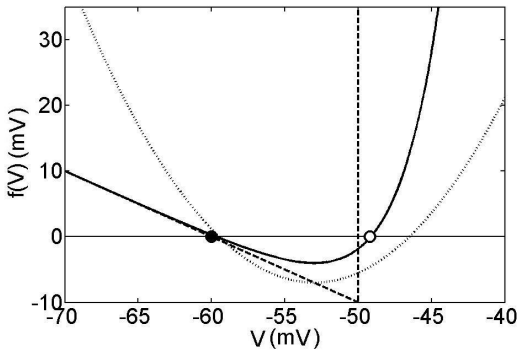

Figure 1.8: The $I-V$ curve of the EIF (solid line), QIF (dotted line), and LIF (dashed line) neurons. The EIF neuron has two fixed points, a stable (•) and an unstable (○).

where $\tau_m = C/g_L$ is the membrane time constant, $f(V)$ is a nonlinear function of voltage, and I_{app} is the applied current. Similar to the IF model, when the membrane voltage reaches threshold potential V_{th}, a spike is emitted and the voltage is reset to V_{re}. The LIF model [21, 84, 156] is the special case of this model with $f(V) = E_L - V$. Different nonlinear forms of $f(V)$ have been proposed to explicitly describe spike initiation.

Quadratic-integrate-and-fire model

The quadratic-integrate-and-fire (QIF) neuron [44, 45, 64] is an example of the NLIF model for which

$$f(V) = \frac{1}{2\Delta_T}(V - V_T)^2 + (E_L - V_T). \tag{1.22}$$

If one chooses $V_{re} = -\infty$, it represents the normal form of type I neurons [44, 45].

Exponential integrate-and-fire model

Another model for nonlinear $f(V)$ obtained in a more biophysically-motivated way is the exponential integrate-and-fire (EIF) model [52]. It includes the activation of

sodium current and is obtained by fitting the region of the spike onset to the WB model. The function $f(V)$ is given by

$$f(V) = E_L - V + \Delta_T \exp\big((V - V_T)/\Delta_T\big). \tag{1.23}$$

As defined in [52], the parameter V_T for both QIF and EIF models is the largest steady-state voltage at which the neuron driven by constant input can stay in subthreshold regime. For the EIF model, the corresponding current is $I_{th} = V_T - E_L - \Delta_T$ above which repetitive firing occurs. The parameter Δ_T is defined as the spike slope factor and it measures the sharpness of the spike initiation. In the limit $\Delta_T \to 0$ (a very sharp spike), the EIF neuron becomes equivalent to the LIF model with $V_{th} = V_T$. In both QIF and EIF models when the input current reaches the threshold, the membrane potential diverges to infinity in finite time, therefore V_{th} can be taken to be infinity.

In Fig. 1.8, the function $f(V)$, $I - V$ curve, is plotted for the EIF, QIF, and LIF models. The EIF model has two fixed points, a stable node representing resting potential and an unstable node for spike-initiation threshold. They divide $f(V)$ into two regions of linear, arising from the passive property of the neuron and nonlinear with rapid exponential increase at high voltage [9].

It has been shown [53] that the nonlinear form of the function $f(V)$ is a crucial determinant for the neuronal response to fast fluctuating inputs. In *vivo*, such an input is produced by an ongoing synaptic bombardment originated from thousands of other neurons. This synaptic input acts as a source of noise and can be described by stochastic models. In Chapters 3 and 4, the effects of these fluctuating inputs on the response properties of the EIF neuron are studied. In the next section, some models of synaptic inputs are described.

1.3 Models of synaptic currents

Neurons in the central nervous system exhibit stochastic behavior as a consequence of membrane channel noise and synaptic noise. The membrane channel noise arises due to the finite number of ion channels. As it was mentioned earlier, most ion channels have two states of open or close. The conductivity of the membrane for typical ion is proportional to the number of open channels of that ion. The actual number of open channels fluctuates and these fluctuations can be neglected under assumption of a large number of ion channels. In all HH-type models, this assumption is considered. This kind of noise is called intrinsic noise.

Another source of noise of our interest is synaptic noise. It is due to signal transmission and network effects (external noise) [59]. It is generated by action potentials carried by thousands of afferent fibers. Many mathematical descriptions of synaptic currents have been proposed, from simple to realistic [38]. Realistic models are based on the fact that synapses modify the conductances of their neuronal targets rather than simply injecting current [91]. In this case, the synaptic current is given by

$$W(V,t) = g_s(t)(V - E_s), \tag{1.24}$$

where the synaptic conductance g_s is a time-dependent random variable and E_s is the synaptic reversal potential. In the following, I review simple models of synaptic current which are based on the current changes at synaptic sites rather than conductance changes.

1.3.1 Instantaneous synaptic kinetics

Consider the situation in which a neuron receives input through N synapses. If one neglects the synaptic time constant as being short when compared to the neuronal time constant τ_m, the postsynaptic input can be modeled as a train of delta functions as

$$W(t) = \sum_{i=1}^{N} J_i \sum_k \delta(t - t_i^k)\tau_m,$$

where the first sum is over N synapses and the second, over all firing times t_i^k of each synapse. The efficacy of the synapse i is J_i describing the amplitude of the postsynaptic current and t_i^k is the random time of the kth presynaptic spike from the ith synapse. In this description, the $(V - E_s)$ term used in the synaptic current (1.24) is neglected [156]. The input spike train causing a sequence of synaptic currents is often assumed to be a Poisson process with mean activation rate $N\nu$. If ν is large and the synaptic weights, J_i, are small, many synaptic events must add up to fire the cell. Further, if $N\nu \gg 1$, the Poisson process can be approximated by a diffusion process (Gaussian white noise) with the same mean and variance. Thus, the synaptic input can be approximated [156, 3, 51] by Gaussian white additive noise as

$$W(t) = \mu + \sigma\sqrt{2\tau_m}\xi(t), \tag{1.25}$$

where $\mu = \langle J_i \rangle N\nu\tau_m$, with $\langle\cdot\rangle$ indicating the average over all synapses, $\sigma^2 = \langle J_i^2 \rangle N\nu\tau_m$, and ξ is a Gaussian white noise characterized by its mean, $\langle \xi(t) \rangle = 0$ and the autocorrelation $\langle \xi(t)\xi(s) \rangle = \delta(t - s)$. The parameter σ stands for the intensity of the white noise, while μ denotes the mean of the input current.

A limitation of this model is the assumption that the synaptic current is in-

stantaneous. However, the massive input received by cortical neurons, for instance, is filtered by a first order synaptic dynamics (see below), leading effectively to an Ornstein-Uhlenbeck (OU) process, i.e., the input is an exponentially correlated (coloured) Gaussian noise [14, 51].

1.3.2 Non-instantaneous synaptic kinetics

Synapses transmit input action potentials with a very rapid rise time (often less than 1 ms) but a slower exponential decay with time constant τ_s (in the range of 2 to 100 ms depending on the type of the receptor [40]). Therefore, the synaptic current is defined [51] by

$$\tau_s \frac{dW}{dt} = -W + \sum_{i=1}^{N} J_i \sum_k \delta(t - t_i^k)\tau_m.$$

In this description, the rise time of the synaptic current is neglected and τ_s is assumed to be identical for all synapses. If the diffusion approximation is valid, the synaptic current dynamics is an OU process defined by

$$\tau_s \frac{dW}{dt} = -W + \mu + \sigma\sqrt{2\tau_m}\xi(t). \tag{1.26}$$

This OU process, known as coloured noise, has a Gaussian stationary probability density

$$P(W) = \frac{1}{\sqrt{2\pi\sigma^2(\tau_m/\tau_s)}} \exp\Big(-\frac{-(\mu - W)^2}{2\sigma^2(\tau_m/\tau_s)}\Big),$$

and an exponential correlation function

$$\langle (W(t) - \mu)(W(s) - \mu)\rangle = \sigma^2 \frac{\tau_m}{\tau_s} \exp\big(-|t - s|/\tau_s\big). \tag{1.27}$$

1.4 Outline

Now a brief outline of each chapter is given.

Chapter 2 studies the periodically driven RF system which is based on the firing map formulation, analyzing the mode-locked solutions, and constructing their instability borders in parameters space leading to the Arnol'd tongues structure. Further, the Liapunov exponents are calculated allowing one to identify the existence of chaotic solutions. Of particular interest will be the identification of period-adding bifurcations leading to chaos. The chapter ends with a discussion on numerical techniques both direct numerical methods and numerical continuation which have been used throughout the chapter for the dynamics of the system and calculation of the bifurcation diagrams.

Chapter 3 considers the EIF model with filtered synaptic fluctuations. Using a population density approach, the role of fast and slow synaptic currents on the steady-state firing rate is discussed. Throughout this chapter, both analytical techniques including a perturbative expansion of the Fokker-Planck equation and an efficient numerical scheme (threshold integration method) are used to approximate the firing rate.

Chapter 4 contains results on the effects of synaptic fluctuations on signal coding of the EIF neuron. Here, the analysis of the previous chapter is generalized to deal with the question of how the instantaneous firing rate of neurons is modulated by a small time-dependent perturbation of the input mean as well as of noise intensity. For each case, first the response of the neuron in the low-frequency input limit is treated, then the high-frequency asymptote is derived.

Chapter 5 introduces the EIFh and EIFh$_\infty$ neuron models in which the spike-generation mechanism is suppressed respectively by the inactivation of the sodium current, the h variable and its steady-state variable h_∞. The significance of the

fast sodium inactivation in modulating input-output properties of neurons in the presence of filtered synaptic fluctuations is studied. Methods used in this chapter are mainly identical with those presented in Chapters 3 and 4.

In Chapter 6 mode locking of the EIF neuron model in deterministic and stochastic cases are shown.

Chapter 7 concludes with a discussion and an outlook of all chapters.

Chapter 2

Mode locking in a periodically forced resonate-and-fire neuron model

2.1 Introduction

Biological neurons have a wide range of ionic currents. The interaction of these currents generates action potentials and may also lead to complex dynamics including resonance and damped oscillations. Our concern in this chapter is to explore the effects of periodic forcing on the firing dynamics of resonant neurons. In particular, we are interested in studying the precise timing of firing events. Here, our focus is on the resonate-and-fire (RF) neuron model which is the simplest model exhibiting subthreshold resonance.

The response of neurons to periodic input can include mode-locking patterns as well as chaotic patterns. We study the existence of both periodic and chaotic solutions and look at the transitions between these states.

The outline of the chapter is as follows. We begin in Sec. 2.2.1 with biological evidence for resonant neurons as well as the motivation for the model. Then in Secs. 2.4 and 2.5, we introduce the RF model using the linearization theory of Koch [87] on the HH equations and analyze the subthreshold response of the system to periodic input. In Sec. 2.6, we express the firing times of the model in terms of an implicit one-dimensional time map and find mode-locked solutions. These solutions can be created or destroyed in smooth or nonsmooth bifurcations. We look at the stability of solutions in Secs. 2.8 and 2.9 by finding conditions for the existence of tangent and grazing bifurcations and in Sec. 2.10 show our results on Arnol'd tongues. Sec. 2.11 investigates the invertibility of the firing map. We then proceed to derive the largest Liapunov exponents of the model in Sec. 2.12. This allows one to determine the existence of chaos. Interestingly, we show that the model has chaotic behavior (positive Liapunov exponent) when the forcing frequency is close to the resonant frequency. Sec. 2.13 contains results of the chapter, in particular the identification of period-adding behavior leading to chaotic solutions. Numerical methods for simulation, parameter continuation and bifurcation detection are given in Sec. 2.14. The chapter ends with a brief discussion in Sec. 2.15 of the results and suggests some extensions of our work.

2.2 Background

2.2.1 Experimental evidence for resonance

Resonant behavior, in which the response of the induced oscillating voltage peaks at a preferred input frequency, has been observed in many biological neurons. For example, in thalamic [71, 131], cortical neurons [61, 72, 79], hippocampal CA1

pyramidal cells [93], and interneurons [130]. It is known that receptor cells in auditory and electro-receptive systems of many species show electrical resonance; also in amphibian cochlea, hair cells behave like small electrical resonant elements [87]. The resonant and oscillatory behavior are also believed to play an important role in brain activities, e.g., the possible functional importance of resonance and oscillations observed in thalamic and cortical neurons lies in the known participation of these neurons in various brain rhythms. The low-frequency resonances in the cortex and thalamus appear suited to support the thalamocortical delta wave oscillations which are particularly prominent during deep sleep [74]. The higher-frequency oscillatory behavior and underlying resonance in pyramidal and inhibitory neurons of the neocortex might have some involvement with higher-frequency rhythms that appear in the cortex during cognition [74].

To understand these nontrivial phenomena, neurodynamical models based on spiking neurons are used. They play an increasing role in the interpretation of neurophysiological data [30].

2.2.2 Motivation of the model

The response of neurons to periodic forcing has long been investigated [54, 158]. There are many interesting analysis of the response of spiking neurons to periodic stimuli [81, 12, 30, 159, 35, 90, 26, 80, 94]. Among them, the leaky IF models and the modified IF models are of particular interest, as they are the simplest spiking neuron models capable of reproducing a great deal of known features of real neurons. For example, the periodically forced LIF model reproduces rectification and phase-locking behavior [150, 132, 7] and can display quasiperiodic and

periodic firing trains [30], integrate-and-fire-or-burst reproduces temporal tuning of both postinhibitory rebound bursting and tonic spiking [35], the ghostbursting model can exhibit chaotic bursting [90], and the IF model with threshold fatigue [26] can exhibit chaotic behavior. However, these simple models fail to generate subthreshold damped oscillations and resonance that have been observed in certain neurons [72, 103] and in almost all biophysically detailed HH-type neuron models [74, 72]. This motivated the introduction of the RF model [76, 19, 138] (called the generalized IF model in [19, 138]) to describe more accurately these types of subthreshold properties.

The RF model is perhaps the simplest possible model exhibiting subthreshold resonance. It has piecewise smooth dynamics such that the effect of the flow reaching threshold is to cause an instantaneous jump in the flow, so that a complete description in terms of smooth differential equations is no longer possible. This kind of dynamics is described in the context of impact oscillators or more generally of hybrid systems [11]. Our approach to study this model is similar to those used in [30, 90].

The RF dynamics is obtained by linearization of the HH equations around the steady-state potential. First, we describe this linearization.

2.3 Linearization of ion currents with voltage-dependent conductance

It is a well known fact that a small excitatory synaptic input in the presence of certain voltage-dependent channels will lead to a local depolarization, followed by hyperpolarization [87]. Such an overshooting response indicates the presence of

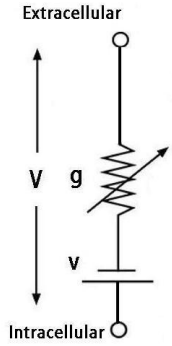

Figure 2.1: Equivalent electrical circuit for voltage-gated current I with nonlinear conductance g and reversal potential V.

the so called RLC circuits which include resistances, capacitances as well as inductances [87]. Although a real neuron does not have any elements like inductance, neuron membranes within certain types of voltage and time-dependent conductances can behave as if they contained inductances [87]. This phenomenological inductance, was first described by Cole [28, 29] in the squid axon. The Koch theory [87, 86] is used to explain how an inductance like behavior can arise from a membrane by linearizing the HH equations.

In order to demonstrate the principle behind this linearization, we consider the HH type model with N ion channels and use Eqs. (1.1) and (1.2) to write

$$C\frac{dV}{dt} = -g_L(V - E_L) - \sum_{k=1}^{N} I_k, \tag{2.1}$$

where I_k satisfies Eq. (1.3) with g_k given in Eq. (1.8).

Instead of the total ionic current in Eq. (2.1), we consider a generic current $I(V, n_1, \cdots, n_M)$ as a function of membrane voltage V and M gating variables $(n_1, \cdots, n_M)$ and demonstrate the corresponding voltage-dependent conductance with g. The equivalent electrical circuit of the current I with nonlinear conductance

g is shown in Fig. 2.1. The conductance is shown with an arrow to indicate that it can vary with the membrane voltage. The gating variable n_k is given by Eq. (1.6) as

$$\frac{d}{dt}n_k = \alpha_k(V)(1-n_k) - \beta_k(V)n_k, \quad k = 1, \ldots, M. \tag{2.2}$$

We consider a small perturbation δV of the membrane voltage around the steady-state voltage V_{ss}. This causes variations in the ionic current I as

$$\delta I = \left(\frac{\partial I}{\partial V}\right)_{ss} \delta V + \sum_{k=1}^{M} \left(\frac{\partial I}{\partial n_k}\right)_{ss} \delta n_k, \tag{2.3}$$

where subscript ss denotes that derivatives are evaluated at the steady state. From Eq. (2.2) and to linear order, δn_k satisfies

$$\frac{d}{dt}(\delta n_k) = \delta\alpha_k - (\delta\alpha_k + \delta\beta_k)n_k - (\alpha_k + \beta_k)\delta n_k. \tag{2.4}$$

Since both α_k and β_k are just voltage dependent, their variations can be written as

$$\delta\alpha_k = \left(\frac{d\alpha_k}{dV}\right)\delta V, \quad \delta\beta_k = \left(\frac{d\beta_k}{dV}\right)\delta V. \tag{2.5}$$

Therefore, substituting Eq. (2.5) into Eq. (2.4) gives

$$\frac{d}{dt}(\delta n_k) = \frac{d\alpha_k}{dV}\delta V - (\alpha_k + \beta_k)\delta n_k - n_k\frac{d(\alpha_k + \beta_k)}{dV}\delta V. \tag{2.6}$$

This expression can be rewritten as

$$\left[\frac{d}{dt} + \alpha_k + \beta_k\right]\delta n_k = \left[\frac{d\alpha_k}{dV} - n_k\frac{d(\alpha_k + \beta_k)}{dV}\right]\delta V. \tag{2.7}$$

Now, one can substitute Eq. (2.7) into Eq. (2.3) to get the following equation for the first order of variation of current I

$$\delta I = \left[G + \sum_{k=1}^{M} \frac{a_k}{\dfrac{d}{dt} + b_k}\right]\delta V, \tag{2.8}$$

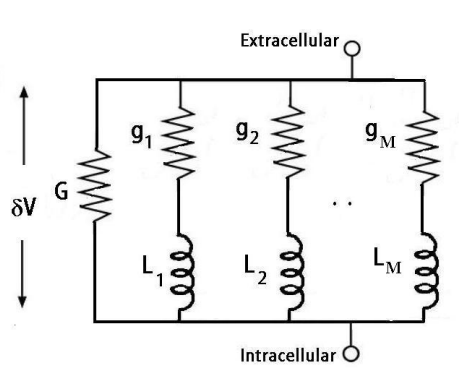

Figure 2.2: Equivalent electrical circuit for linearized current I.

where $G = (\partial I/\partial V)_{ss}$. Parameters a_k and b_k are given by

$$\begin{aligned} a_k &= \left(\frac{\partial I}{\partial n_k}\right)_{ss} \left[\left(\frac{d\alpha_k}{dV}\right)_{ss} - n_{k,\infty}\left(\frac{d(\alpha_k+\beta_k)}{dV}\right)_{ss}\right]\delta V, \\ b_k &= (\alpha_k+\beta_k)_{ss}, \end{aligned} \tag{2.9}$$

with $n_{k,\infty}$ the steady-state value of n_k, see Eq. (1.7). The current δI in Eq. (2.8) is similar to the current passing through the electrical circuit shown in Fig. 2.2 with M inductance branches parallel with a conductance G. To see this, we write the voltage of each inductance branch as

$$\delta V = \left(\frac{1}{g_k} + L_k\frac{d}{dt}\right)\delta\bar{I}_k, \qquad k = 1,\ldots,M, \tag{2.10}$$

where $\delta\bar{I}_k$ is the current through both conductance g_k and inductance L_k. Therefore, the total current of the circuit is given by

$$\delta\bar{I} = \left[G + \sum_{k=1}^{M}\frac{1}{L_k\dfrac{d}{dt} + \dfrac{1}{g_k}}\right]\delta V. \tag{2.11}$$

A comparison between Eqs. (2.8) and (2.11) shows that δI and $\delta\bar{I}$ are identical if

$$g_k = \frac{a_k}{b_k}, \quad L_k = \frac{1}{a_k}, \quad k = 1,\ldots,M.$$

Hence for a small perturbation δV, the ionic current $I(V, n_1, \ldots, n_M)$ responds as if the conductance G is in parallel with M impedance lines.

Therefore, using Eqs. (2.1), (2.8) and (2.10), the linearized HH equations are given by

$$C\frac{dV}{dt} = -\tilde{G}V - \sum_{k=1}^{M} I_k, \qquad \tilde{G} = G + g_L, \tag{2.12}$$

$$L_k\frac{dI_k}{dt} = -\frac{I_k}{g_k} + V, \qquad k = 1, \ldots, M. \tag{2.13}$$

2.4 The resonate and fire neural model

The RF system corresponds to Eqs. (2.12) and (2.13) with only one inductive path way. Therefore, the subthreshold behavior of the periodically forced system satisfies

$$\begin{aligned} C\frac{dV}{dt} &= -\frac{V}{R} - I + I_{app}(t), \qquad R = \frac{1}{\tilde{G}}, \\ L\frac{dI}{dt} &= V - rI, \qquad r = \frac{1}{g}, \end{aligned} \tag{2.14}$$

where V is the membrane voltage, the current I is a resonant current, e.g., delayed rectifier K^+ or I_h, and $I_{app}(t)$ is periodic applied current such that $I_{app}(t+T) = I_{app}(t)$. The specific case we will study for our numerical simulations is $I_{app}(t) = I_0 + \epsilon\sin(\omega t)$, where ϵ is the amplitude of forcing, I_0 is a constant current, and ω is the forcing frequency. It should be noted that when r is large, the RF model reduces to the LIF model (the RLC circuit practically become a RC circuit).

System (2.14) is supplemented with the condition that whenever voltage reaches the threshold potential, a spike is registered, the system state is instantly reset according to a reset map, and the dynamics continues. Therefore, its dynamics is piecewise smooth but event driven, in the sense that smoothness is lost

at instantaneous events, for example, upon application of the reset map. Below, we define the threshold potential and the reset map.

It proves convenient to consider system (2.14) in the following form,

$$\frac{d\mathbf{x}}{dt} = A\mathbf{x} + f(t), \tag{2.15}$$

where

$$A = \begin{pmatrix} -(RC)^{-1} & -C^{-1} \\ L^{-1} & -rL^{-1} \end{pmatrix}, \tag{2.16}$$

and

$$\mathbf{x} = \begin{pmatrix} V \\ I \end{pmatrix}, \; f(t) = \begin{pmatrix} \frac{I_{app}(t)}{C} \\ 0 \end{pmatrix}.$$

We assume the threshold potential can be defined by the zero set of a smooth function $h(\mathbf{x}, t) = V - k(t)$ as

$$\text{threshold} = \{\mathbf{x}(t) : h(\mathbf{x}(t), t) = 0\}, \tag{2.17}$$

where $k(t)$ is a continuous function and in the simplest case is a constant. Therefore, the nth firing time t_n is defined by

$$t_n = \inf\{t | h(\mathbf{x}(t), t) \geq 0, t \geq t_{n-1}, V'(t) \neq k'(t)\}, \tag{2.18}$$

where a prime denotes a derivative. Whenever the RF orbit intersects the threshold transversely, the instantaneous transition from threshold takes place, which in fact changes the position of the orbit according to a reset map $\mathbf{R}$,

$$\text{if} \quad h(\mathbf{x}, t) = 0 : \qquad \mathbf{x} \mapsto \mathbf{R}(\mathbf{x}, t).$$

Assuming that a spike occurs at time t_n, we represent the intersection of the flow with threshold immediately before the crossing with $\mathbf{x}^-$ and immediately after the

crossing with $\mathbf{x}^+$. Hence, $\mathbf{x}^- = \lim_{t\to t_n^-} \mathbf{x}(t)$ and $\mathbf{x}^+ = \lim_{t\to t_n^+} \mathbf{x}(t)$. Therefore, one can write the resetting mechanism of the trajectory at each firing time as

$$\mathbf{x}^+ = \mathbf{R}(\mathbf{x}^-, t). \tag{2.19}$$

2.5 The subthreshold behavior

The subthreshold behavior of system (2.15) is linear and therefore easy to analyze. Its solution is given by

$$\mathbf{x}(t) = G(t)\mathbf{x}(0) + \int_0^t G(t-s)f(s)\,\mathrm{d}s, \tag{2.20}$$

where $G(t)$ is the matrix exponential (Green's function) $G(t) = \exp(At)$.

System (2.15) can show different types of subthreshold behavior associated with different neuronal characteristics. We are interested in resonant behavior and its corresponding region of parameters. In the parameter region where resonant behavior occurs, the system has either a stable node or a stable focus. As we want to focus on the occurrence of the mode-locked solutions and chaos, we do not describe different regimes here. For a complete classification of the subthreshold regime, see [138, 19].

If the system has a stable focus then matrix A has a complex-conjugate pair of eigenvalues $\alpha \mp i\beta$, with $\alpha = -(rCR + L)/(2CRL)$ and $\beta^2 = (R + r)/(CRL) - \alpha^2$. For $\lambda = \alpha + i\beta$, the associated complex eigenvector is ν such that $\nu = \nu_R + i\nu_I \in \mathbb{C}^2$,

$$\nu = \begin{pmatrix} r + L\alpha \\ 1 \end{pmatrix} + i \begin{pmatrix} L\beta \\ 0 \end{pmatrix}.$$

Therefore, we have $G(t) = e^{\alpha t} P R_\beta P^{-1}$, where

$$R_\beta = \begin{pmatrix} \cos(\beta t) & -\sin(\beta t) \\ \sin(\beta t) & \cos(\beta t) \end{pmatrix},$$

$$P = \begin{pmatrix} \nu_I & \nu_R \end{pmatrix} = \begin{pmatrix} L\beta & r + L\alpha \\ 0 & 1 \end{pmatrix}.$$

Now, one can write the explicit form of $G(t)$ as

$$G(t) = \begin{pmatrix} G_{11}(t) & G_{12}(t) \\ G_{21}(t) & G_{22}(t) \end{pmatrix}, \tag{2.21}$$

with

$$G_{11}(t) = \frac{e^{\alpha t}}{L\beta}\big[L\beta\cos(\beta t) + (r + L\alpha)\sin(\beta t)\big], \tag{2.22}$$

$$G_{12}(t) = -\frac{e^{\alpha t}}{L\beta}\big[(L\beta)^2 + (r + L\alpha)^2\big]\sin(\beta t), \tag{2.23}$$

$$G_{21}(t) = \frac{e^{\alpha t}}{L\beta}\sin(\beta t), \tag{2.24}$$

$$G_{22}(t) = \frac{e^{\alpha t}}{L\beta}\big[L\beta\cos(\beta t) - (r + L\alpha)\sin(\beta t)\big]. \tag{2.25}$$

Similarly, in the case of a stable node, one can calculate eigenvalues $\lambda_{1,2} = \alpha \pm \sqrt{-\beta^2}$ and write $G(t) = P R_{\alpha,\beta} P^{-1}$, where

$$R_{\alpha,\beta} = \begin{pmatrix} e^{\lambda_1 t} & 0 \\ 0 & e^{\lambda_2 t} \end{pmatrix}, \text{ and}$$

$$P = \begin{pmatrix} r + L\lambda_1 & r + L\lambda_2 \\ 1 & 1 \end{pmatrix}.$$

Therefore, we obtain

$$G_{11}(t) = \frac{\exp(\lambda_1 t)(r + L\lambda_1) - \exp(\lambda_2 t)(r + L\lambda_2)}{L(\lambda_1 - \lambda_2)}, \tag{2.26}$$

$$G_{12}(t) = \frac{(r + L\lambda_1)(r + L\lambda_2)\big[\exp(\lambda_2 t) - \exp(\lambda_1 t)\big]}{L(\lambda_1 - \lambda_2)}, \tag{2.27}$$

$$G_{21}(t) = \frac{\exp(\lambda_1 t) - \exp(\lambda_2 t)}{L(\lambda_1 - \lambda_2)}, \tag{2.28}$$

$$G_{22}(t) = \frac{\exp(\lambda_2 t)(r + L\lambda_1) - \exp(\lambda_1 t)(r + L\lambda_2)}{L(\lambda_1 - \lambda_2)}. \tag{2.29}$$

2.6 Firing time map

For simplicity, we assume that the RF oscillator is driven by a constant input I_0 such that in the absence of any periodic forcing it still oscillates. The system evolves smoothly between firing times so that we can define a discrete firing-times map that expresses the system state at one firing time as a function of the state at the previous firing time. Therefore, using Eq. (2.20) one can write

$$\mathbf{x}(t_{n+1}) = G(\Delta^n)\mathbf{x}(t_n) + \int_0^{\Delta^n} G(s) f(-s + t_{n+1})\, \mathrm{d}s, \tag{2.30}$$

where $\Delta^n = t_{n+1} - t_n$ is the interspike interval (ISI). Now, we assume a simple case of the threshold function

$$h(\mathbf{x}, t) = V - 1, \tag{2.31}$$

and define the resetting mechanism by

$$\mathbf{x}^+ = \mathbf{R}(\mathbf{x}^-, t) = \mathbf{0}. \tag{2.32}$$

Using conditions (2.31) and (2.32), Eq. (2.30) gives a one-dimensional time map in the implicit form of

$$F(t_n, t_{n+1}) \equiv \int_0^{\Delta^n} G_{11}(s) I_{app}(-s + t_{n+1})\, \mathrm{d}s - C = 0, \tag{2.33}$$

as well as an expression to evaluate the current at firing time t_{n+1},

$$I(t_{n+1}) = C^{-1} \int_0^{\Delta^n} G_{21}(s) I_{app}(-s + t_{n+1})\, \mathrm{d}s. \tag{2.34}$$

Efficient numerical methods exist to compute the firing times and to follow these as the system parameters vary. These firing times can exhibit periodic patterns. Next we focus on these solutions.

2.7 Mode-locked solutions

To classify possible rhythms of the firing time of the system, we use the theory of mode locking, which relates the period of the output spike train to the period of forcing rationally. When the RF orbit repeats exactly after a fixed number, p, of spikes and a fixed number, q, of forcing period T, the resulting train is called a $p : q$ mode-locked solution, where $p, q \in \mathbb{Z}$. Therefore, the winding number of a $p : q$ mode-locked solution is p/q, that is the average number of firing events per period of the forcing. We can construct mode-locked solutions explicitly and analyze how their existence changes as the system parameters vary.

It is convenient to introduce the nth firing time of a $p : q$ mode-locked solution as in [30, 90] as

$$t_n = \left(\left[\frac{n}{p} \right] + \phi_{n(p)} \right) qT, \qquad n = 0, 1, 2 \ldots, \tag{2.35}$$
$$n(p) = n \mod p,$$

where $\phi_0, \ldots, \phi_{p-1} \in [0, 1)$ are a collection of firing phases and $[\cdot]$ denotes the integer part. A $p : q$ mode-locked solution is determined by the p firing phases $(\phi_0, \ldots, \phi_{p-1})$. These firing phases can be found by substituting Eq. (2.35) into

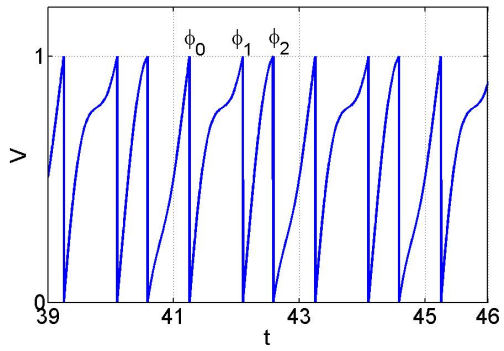

Figure 2.3: A 3:2 mode-locked solution arising in a sinusoidally driven RF system. The membrane voltage trajectory shows that the system fires three spikes (with phases ϕ_0, ϕ_1, and ϕ_2) for every two periods of I_{app} with $I_{app}(t) = 2.23 + \sin(2\pi t)$, $R = C = L = 1$, and $r = 0.1$.

Eq. (2.33) and solving the p equations

$$F_n(\Phi, qT) \equiv \int_0^{\Delta^n} G_{11}(s) I_{app}\Big(-s + \phi_{n+1(p)} qT \Big)\, \mathrm{d}s - C = 0,\ \ n = 0, \ldots, p-1, \tag{2.36}$$

where $\Phi = (\phi_0, \phi_1, \ldots, \phi_{p-1})$.

However, not all of the values of Φ obtained by such a procedure correspond to a $p : q$ mode-locked solution. They must also satisfy conditions that guarantee that such an orbit is physically possible. From the definition of firing times (2.18), we already know that one such restriction is

$$\frac{dV}{dt}(t_n) \neq 0, \qquad n = 0, \ldots, p-1.$$

As parameters in the system vary, this condition may be broken at certain isolated values, giving rise to *grazing bifurcation* points, at which the qualitative properties of the solution change, often in a dramatic manner. This kind of bifurcation, which is the result of crossing and resetting rules, is called [11] a *discontinuity-induced-bifurcation* (DIB) and we address them later.

As an example, a 3:2 mode-locked solution of the system is shown in

Fig. 2.3. It shows the voltage trajectory in response to $I_{app}(t) = 2.23 + \sin(2\pi t)$. Within each two periods of the driving signal, three spikes are fired with corresponding phases ϕ_0, ϕ_1, and ϕ_2. The average of the firing period is also defined by $\langle \Delta \rangle = \lim_{N\to\infty} 1/N \sum_{n=0}^{N} \Delta^n$. Therefore, using Eq. (2.35), the average of the firing times of the $p : q$ mode-locked solution per period of the input satisfies $\langle \Delta \rangle = q/p$.

For periodically forced systems, there typically exist regions in parameters space in which mode-locked solutions exist. These regions are called *Arnol'd tongues*, emanating from rational points on the zero forcing ($\epsilon = 0$) and opening up into regions where the forcing strength is turned on. Each tongue corresponds to a $p : q$ mode-locked solution for which the ratio of the forcing frequency to the firing frequency is q/p. The boundaries of these tongues are determined by finding the conditions of instability of the relevant mode-locked orbit. By mapping out these boundaries, we can try to partition the parameter space in terms of the qualitative behavior of the system.

2.8 Stability

The structure of Arnol'd tongues can be affected by various bifurcations. We can classify them as smooth bifurcations of the firing map when mode-locked solutions lose their stability, and nonsmooth bifurcations arising from the discontinuity of the system (DIBs) [30, 90].

To detect smooth bifurcation, we perturb the nth firing time of the system about a mode-locked solution such that $t_n \to t_n + \delta_n = t_n^*$. Therefore, the

perturbation of firing map (2.33) is given by

$$F(t^*_{n+1}, t^*_n) \equiv \int_0^{t^*_{n+1}-t^*_n} G_{11}(s) I_{app}(-s + t^*_{n+1}) \mathrm{d}s - C = 0. \tag{2.37}$$

Using the linear expansion of Eq. (2.37), we find

$$\frac{\partial F}{\partial t_{n+1}} \delta_{n+1} + \frac{\partial F}{\partial t_n} \delta_n = 0, \tag{2.38}$$

where the partial derivatives are evaluated at the mode-locked solution. Eq. (2.38) can be rewritten as

$$\delta_{n+1} = \frac{\Gamma_n}{\Phi_n} \delta_n \equiv \kappa_n \delta_n, \tag{2.39}$$

where the coefficients are

$$\begin{aligned} \Gamma_n &= -\frac{\partial F}{\partial t_n} = G_{11}(\Delta^n) I_{app}(t_n), \\ \Phi_n &= \frac{\partial F}{\partial t_{n+1}} = \Gamma_n + \int_0^{\Delta^n} G_{11}(s) \frac{dI_{app}}{dt}(-s + t_{n+1}) \mathrm{d}s. \end{aligned} \tag{2.40}$$

Therefore, the stability of a $p : q$ mode-locked state [30] is determined by the behavior of the map

$$\delta_{n+1} = \kappa(p) \delta_{n+1-p}, \tag{2.41}$$

where

$$\kappa(p) = \kappa_0 \kappa_1 \ldots \kappa_{p-1}. \tag{2.42}$$

If $|\kappa(p)| < 1$, the corresponding mode-locked solution is stable. By varying a parameter, $|\kappa(p)|$ may pass through 1 which results in some bifurcations. Specifically, we expect to observe tangent bifurcation when

$$\kappa(p) = 1, \tag{2.43}$$

and period-doubling bifurcation when

$$\kappa(p) = -1. \tag{2.44}$$

2.9 Grazing bifurcations

Tangent bifurcation is not the only way in which the periodic orbits of the RF system can change their qualitative behavior as the parameters governing the system vary. If periodic solutions have tangential intersections with threshold, grazing bifurcation occurs [11] in which we see changes in the system behavior that are different from those of the smooth system. The linear stability analysis of the firing map cannot detect such kinds of bifurcations that occur when mode-locked solutions interact with discontinuities of the firing map. In general, there could be two types of grazing bifurcations [11, 90].

Type 1 grazing arises when varying a system parameter causes a local maximum to increase through the firing threshold, leading to a new firing event that occurs at some time earlier than usual and between two existing firing times [see Fig. 2.5 upper panels]. Therefore, assuming that $F(t_n, t_{n+1}) = 0$, type 1 nonsmooth bifurcation occurs if

$$V(t_{new}) = 1, \qquad t_n < t_{new} < t_{n+1}, \tag{2.45}$$

$$\frac{dV}{dt}(t_{new}) = 0, \tag{2.46}$$

where at t_{new}, a tangential crossing with the threshold function occurs.

For $p : q$ mode-locked solutions, we can find the graze phase and p firing phases by solving $p + 2$ nonlinear algebraic equations. These are the p equations (2.36) defining the mode-locked solutions with the extra two being Eqs. (2.45) and (2.46). The conditions on type 1 grazing bifurcation can be written in the

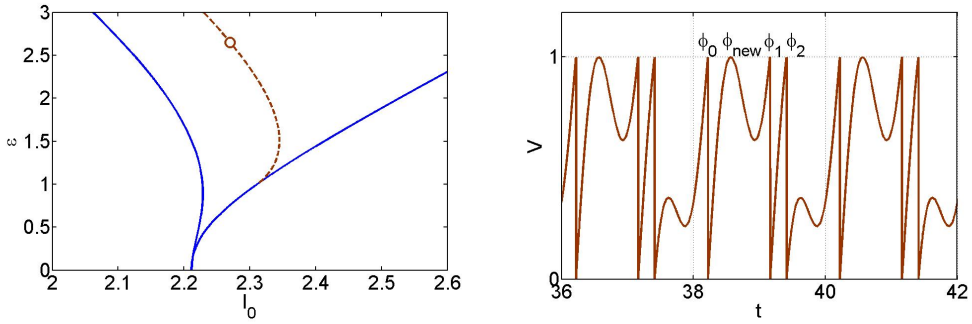

Figure 2.4: Boundary of a 3:2 mode-locked solution in (ϵ, I_0) plane (a) and voltage trajectory on the graze locus (b). (a) The solid line (blue) represents the tangent bifurcation of map (2.41) and the dashed line (red) represents type 1 grazing bifurcation induced by the discontinuity of the RF flow. (b) Voltage trajectory for $I_0 = 2.27$ and $\epsilon = 2.65$ on the graze locus shown with circle in plot (a). The voltage orbit crosses the threshold at phases ϕ_0, ϕ_1, and ϕ_2 transversely and, as we expect it tangentially touches threshold between ϕ_0 and ϕ_1 at a new phase ϕ_{new}. In both plots, other parameters are as in Fig. 2.3.

following form

$$\int_0^{t_{new}-t_n} G_{11}(s) I_{app}(-s + t_{new})\, \mathrm{d}s - C = 0, \tag{2.47}$$

$$\int_0^{t_{new}-t_n} G_{11}(s) \frac{dI_{app}}{dt}(-s + t_{new})\, \mathrm{d}s + G_{11}(t_{new} - t_n) I_{app}(t_n) = 0. \tag{2.48}$$

It should be noted that for this kind of nonsmooth bifurcation, we should specify between which two existing firing times the graze occurs. For small changes in parameters, it is then possible to have $p+1 : q$ mode-locked solution from $p : q$ solution.

In Fig. 2.4(a), we show an analytical solution for 3:2 Arnol'd tongue. As one can see, grazing bifurcation (dashed line) constructs part of the 3:2 tongue and modifies the border of the tongue which originally was constructed by tangent bifurcation (solid line). We can also verify the occurrence of the graze by looking at the voltage trajectory on the graze locus. An example is shown in Fig. 2.4(b)

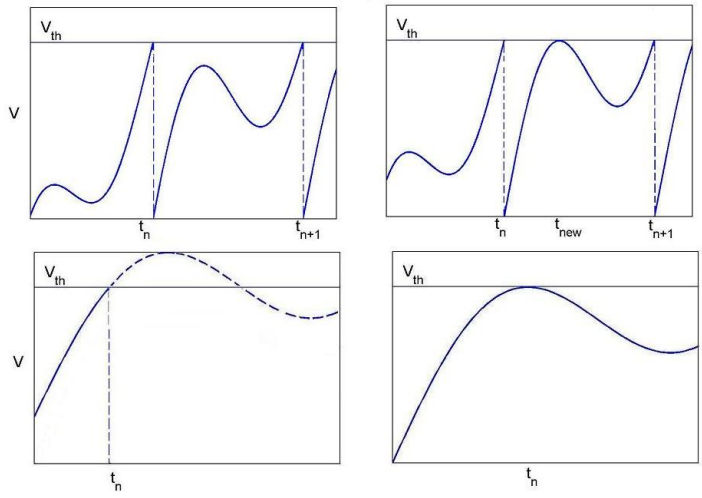

Figure 2.5: Grazing bifurcations whenever a tangential crossing of the firing threshold occurs [90]. Upper panels: type 1 grazing where a local maximum increases through the firing threshold (left) and creates a new firing time (right). Lower panels: type 2 grazing when a local maximum decreases through the threshold (left), causing the solution to be lost in a nonsmooth bifurcation (right).

by choosing the parameters $I_0 = 2.27$ and $\epsilon = 2.65$ on the graze locus of the 3:2 tongue (circle in plot (a)). As expected, three spikes occur, namely, ϕ_0, ϕ_1, and ϕ_2, within every two periods of $I_{app}(t)$. It is clear that the graze as a local maximum arrives between ϕ_0 and ϕ_1 while touching the threshold surface tangentially. This is a bifurcation point for the creation of a new firing time where the 3:2 mode-locked solution may turn into the 4:2 mode-locked solution.

Grazing of type 2 also occurs whenever varying a parameter causes the voltage to reach the threshold but with $dV/dt = 0$ at that time, rather than $dV/dt > 0$ [see Fig. 2.5 lower panels]. This may also cause the solution to be lost in a nonsmooth bifurcation [11, 30] where for small variation of parameters, the $p : q$ mode-locked solution can turn into the $p - 1 : q$ mode-locked solution. This

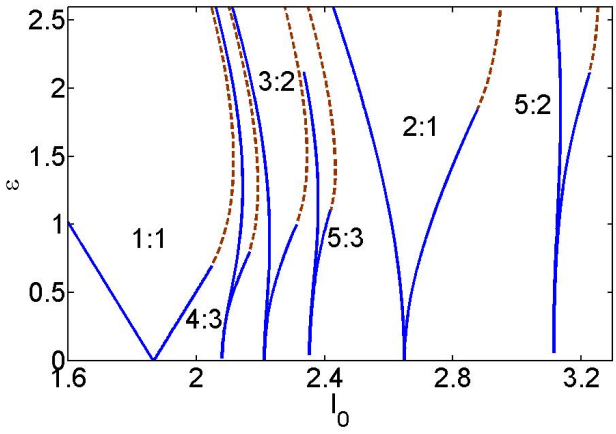

Figure 2.6: The analytical Arnol'd tongues structure. We show boundaries of 1:1, 4:3, 3:2, 5:3, 2:1, and 5:2 tongues, constructed from the union of smooth bifurcations of the firing map and nonsmooth bifurcations induced by discontinuity of the system. Solid lines (blue) indicate a tangent bifurcation of the firing map and dashed lines (red) a nonsmooth grazing bifurcation of the underlying flow. Parameters are as in the caption of Fig. 2.3.

bifurcation is detected by appending the condition

$$\frac{dV}{dt}(t_n) = 0, \tag{2.49}$$

to the p equations (2.36) defining the mode-locked orbit. Equation (2.49) can be translated as

$$G_{11}(\Delta^{n-1})I_{app}(t_{n-1}) + \int_0^{\Delta^{n-1}} G_{11}(s)\frac{dI_{app}}{dt}(-s+t_n)\,\mathrm{d}s = 0.$$

Care must be taken to determine at which firing time the graze takes place.

2.10 Arnol'd tongues

In Fig. 2.6, we exhibit the analytical Arnol'd tongues structure. The boundaries of Arnol'd tongues are determined by both tangent bifurcations (solid lines) and type 1 grazing bifurcations (dashed lines). In the determination of the tongues,

period-doubling bifurcation does not occur and type 2 grazing bifurcation does not seem to play a large role, although it is present. As can be seen, unlike the case of the smooth circle map [110, 13], the tongues do not intersect each other anymore.

Figure 2.6 also illustrates another feature of the Arnol'd tongues, namely that those emanating from the zero forcing amplitude are arranged such that between the $p_1 : q_1$ and the $p_2 : q_2$ tongues, one can expect to see the $p_1+p_2 : q_1+q_2$ tongue, e.g., between 3:2 and 2:1, the 5:3 tongue, between 2:1 and 3:1, the 5:2 tongue, and between 1:1 and 3:2, the 4:3 tongue can be seen. This concatenation of the periodic orbits shows a striking resemblance with the well-known series in number theory proposed by Farey and this phenomenon is referred as Farey arithmetic. It has been shown [11] that periodic orbits of one-dimensional discontinuous piecewise linear map exhibit the same interesting relationship between nearby periodic orbits.

The method to exhibit a $p : q$ Arnol'd tongue in the (I_0, ϵ)-parameter plane is to find a p-periodic point on the tangent-bifurcation curve. It can be done by simultaneously solving p equations (2.36) which satisfy $\kappa(p) = 1$. Continuation of this solution on the tangent-bifurcation locus in the ϵ and I_0 plane constructs part of the boundary of the tongue. Similarly, we find a point on the grazing bifurcation curve by solving $p + 2$ equations (2.36), (2.47), and (2.48) and then use continuation of this solution to find locus of the graze. Details of the numerical methods are described in Sec. 2.14. The continuations of Arnol'd tongues are one-parameter continuations in two-parameter space. A complete discussion on the computing of Arnol'd tongues is given in [146] and for studies on the smooth circle map, its bifurcations, and the corresponding Arnol'd tongues see [110, 13].

Therefore, considering both the smooth bifurcations of the firing map and the grazing bifurcations of the underlying discontinuous flow, we were able to construct the Arnol'd tongue structure of the periodically driven RF system.

2.11 Invertibility

Whenever the grazing bifurcations occur, the map of firing times becomes discontinuous. This discontinuity situation close to a grazing point is due to the fact

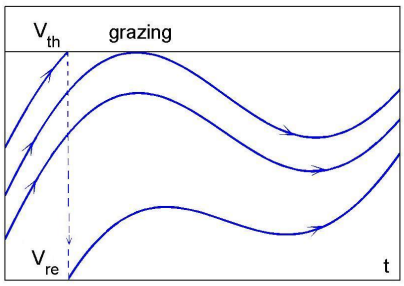

Figure 2.7: Dynamics close to the grazing point.

that a trajectory starting close to the graze either intersects the threshold with a small value of dV/dt or does not intersect the threshold locally, see Fig. 2.7. This causes a drastic difference in subsequent behavior of the trajectories close to the graze. Here we discuss the effect of the grazing bifurcation on the properties of the firing times map.

Using Eq. (2.39), the derivative of the firing times map is given by

$$\frac{\partial t_{n+1}}{\partial t_n} = \frac{\Gamma_n}{\Phi_n}, \tag{2.50}$$

and it becomes unbounded whenever $\Phi_n = 0$. In both types of the grazing bifurcations, the derivative of the map becomes unbounded and the map of firing times is discontinuous. For example, in the case of 1:1 mode-locked solutions,

using the fact that $t_{n+1} - t_n = T$ and $t_n = T(n + \phi_0)$, the discontinuity condition for the firing map reads

$$G_{11}(T)I_{app}(T\phi_0) + \int_0^T G_{11}(s)\frac{dI_{app}}{dt}(-s + T\phi_0)\,\mathrm{d}s = 0,$$

which is satisfied if

$$\int_0^T \frac{d}{dt}G_{11}(s)I_{app}(-s + T\phi_0)\,\mathrm{d}s + I_0 < \epsilon. \tag{2.51}$$

In general, it is complicated to determine the parameter regions in which $\Phi_n = 0$. For a $p : q$ mode-locked solution, the firing map is discontinuous on the locus of the graze, this is shown with dashed lines in the analytical Arnol'd tongue structure, Fig. 2.6. If the firing map is continuous, it is only invertible if $\Gamma_n \neq 0$. In this case, from firing map (2.33), we know that if $F(t, s) = 0$ then $F(t+qT, s+nqT) = 0$ for $n = 1$, indicating that F is a lift associated to a degree one circle map. Therefore, the firing map is an invertible circle map when $I_{app}(t_n) \neq 0$ and $G_{11}(\Delta^n) \neq 0$. It is straightforward to see that $I_{app}(t_n) \neq 0$ when $I_0 > \epsilon$. Given that the RF system has stable node and using Eq. (2.26), the condition $G_{11}(\Delta^n) \neq 0$ is satisfied if $(r + L\lambda_2)/(r + L\lambda_1) < 1$, for $\lambda_2 < \lambda_1$ and for the system with stable focus, using Eq. (2.22), the condition translates into

$$\frac{L\beta}{r + L\alpha} \neq -\tan(\beta\Delta^n).$$

Therefore in the region of 1:1 mode-locked solutions and for the case of stable node, the firing map is an invertible circle map if

$$\int_0^T \frac{d}{dt}G_{11}(s)I_{app}(-s + \phi_0)\,\mathrm{d}s \geq 0, \tag{2.52}$$

and for the case of stable focus, both Eq. (2.52) and condition $L\beta/(r + L\alpha) \neq -\tan(\beta T)$ must satisfy. The map of firing times is not necessarily onto. To ensure

that the firing map is onto, the slope of the voltage at the firing times must be larger than the slope of the threshold, that is $dV/dt(t_n) > 0$.

The firing times of the periodically forced RF system may become irregular. It is believed that variability in the firing times is not necessarily due to noise but could be also due to chaotic behavior [2, 65]. Next, we examine the dynamics of the system in terms of chaotic behavior. This is achieved by calculation of the *Liapunov exponents*.

2.12 Liapunov exponents

For our purpose which is to determine the existence of chaos, we establish that there are regions in parameters space in which the RF model displays sensitive dependence on initial conditions as indicated by a positive Liapunov exponent. To this end, we calculate an expression for the largest Liapunov exponents of the system of equations (2.15).

Liapunov exponents of the RF model can be derived by determining the slopes of the firing map at successive firing times. While the subthreshold dynamics of the system is continuous, the effect of the flow reaching threshold is to cause an instantaneous jump in the flow and introduces a discontinuity into the dynamics. Therefore, the standard approach of calculation of Liapunov exponents is not applicable here. Instead, we use the ideas developed for the study of impact oscillators [120] to estimate Liapunov exponents. This method has been previously used for the IF model [31] and the IF model with threshold fatigue [26]. The main step in this method is to evaluate the consequence of these discontinuities on solutions starting from nearby initial conditions.

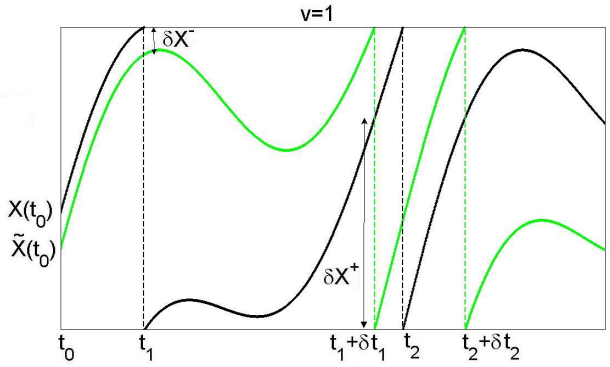

Figure 2.8: Illustration of the method for calculating the Liapunov exponents of the RF model. The unperturbed solution (black), $\mathbf{x}(t)$, intersects the threshold at times t_n while the perturbed solution (green), $\tilde{\mathbf{x}}(t)$, intersects at times $t_n + \delta t_n$. In order to calculate Liapunov exponents, we trace $\delta\mathbf{x}^+ = \tilde{\mathbf{x}}(t_n + \delta t_n^+) - \mathbf{x}(t_n + \delta t_n^+)$ as explained in the text.

We consider system (2.15) with threshold and resetting conditions given in Eqs. (2.31) and (2.32). Given a solution $\mathbf{x}(t) = \big[V(t), I(t)\big]^T$ (the superscript T denotes vector transposition) with initial condition $\mathbf{x}(t_0) = \big[V(t_0), I(t_0)\big]^T$, we define a small perturbation of the solution at time t_0 by $\delta\mathbf{x}(t_0) = \big[\delta V(t_0), \delta I(t_0)\big]^T$. In the absence of firing in the interval $[t_0, t]$, the initial perturbation evolves to the value

$$\delta\mathbf{x}(t) = \begin{pmatrix} \delta V(t) \\ \\ \delta I(t) \end{pmatrix} = G(t - t_0)\delta\mathbf{x}(t_0),$$

where $G(t)$ is given in Eq. (2.21). To calculate the Liapunov exponents, we follow the temporal generation of this perturbation and trace it immediately before the unperturbed orbit crosses the threshold, denoted by $\delta\mathbf{x}^-$ and immediately after the perturbed orbit crosses the threshold, denoted by $\delta\mathbf{x}^+$. We assume the unperturbed solution reaches threshold before the perturbed one at time t_1 and the perturbed solution, $\tilde{\mathbf{x}}(t)$, intersects threshold at time $t_1 + \delta t_1$. The situation is illustrated in

Fig. 2.8. Now we consider the second spike occurs at t_2, therefore we have

$$\delta\mathbf{x}(t) = G(t-t_1)\underbrace{B(t_1)\overbrace{G(t_1-t_0)\delta\mathbf{x}(t_0)}^{\delta\mathbf{x}^-}}_{\delta\mathbf{x}^+}, \quad t < t_2 \tag{2.53}$$

where $\delta\mathbf{x}^+ = \delta\mathbf{x}(t_1 + \delta t_1^+)$ is the new initial condition of $\delta\mathbf{x}$ after the perturbed orbit is reset and the matrix B is related to the derivation of $\delta\mathbf{x}^+$ as explained below.

The goal is to derive an expression for $\delta\mathbf{x}^+ = \delta\mathbf{x}(t_1 + \delta t_1^+)$ as a function of $\delta\mathbf{x}^- = \delta\mathbf{x}(t_1^-)$ by keeping only first-order terms. Using the crossing condition (2.31) and the facts that $\tilde{\mathbf{x}}(t) = \left[\tilde{V}(t), \tilde{I}(t)\right]^T$, $\delta V(t) = \tilde{V}(t) - V(t)$, and $\delta I(t) = \tilde{I}(t) - I(t)$, at time $t_1 + \delta t_1$, we have

$$\begin{aligned} 0 =& h\big(\tilde{\mathbf{x}}(t_1+\delta t_1)\big) = \tilde{V}(t_1+\delta t_1) - 1 \\ \approx& \tilde{V}(t_1) + \delta t_1 \tilde{V}'(t_1) - 1 \approx \delta V(t_1) + \delta t_1 V'(t_1), \end{aligned} \tag{2.54}$$

where a prime denotes a derivative. Therefore, the perturbation of firing time t_1 is approximately given by

$$\delta t_1 = \frac{-\delta V(t_1)}{V'(t_1)}, \tag{2.55}$$

where we have assumed the denominator is not zero. At $t = t_1 + \delta t_1^+$, using resetting condition (2.32), we find

$$\begin{aligned} \delta V^+ = \delta V(t_1+\delta t_1^+) &= \tilde{V}(t_1+\delta t_1^+) - V(t_1+\delta t_1^+) \\ &\approx -\delta t_1 V'(t_1^+). \end{aligned} \tag{2.56}$$

Furthermore, we have

$$\begin{aligned} \delta I^+ &= \tilde{I}(t_1+\delta t_1^+) - I(t_1+\delta t_1^+) \\ &\approx -I(t_1^+) - \delta t_1 I'(t_1^+) = 0. \end{aligned} \tag{2.57}$$

Equations (2.55)-(2.57) result in

$$\delta V^+ = \gamma(t_1)\delta V(t_1), \qquad \delta I^+ = 0,$$

where

$$\gamma(t) = \frac{I_{app}(t)}{I_{app}(t) - R^{-1} - I(t)}, \tag{2.58}$$

with $I(t)$ given in Eq. (2.34). In this way, we find

$$B(t) = \begin{pmatrix} \gamma(t) & 0 \\ 0 & 0 \end{pmatrix}. \tag{2.59}$$

Now for the general case where there are n spikes at times $0 \leq t_1 < \ldots < t_n < t$, we obtain

$$\delta\mathbf{x}(t) = G(t-t_n)B(t_n)G(t_n - t_{n-1})\ldots G(t_2 - t_1)B(t_1)G(t_1 - t_0)\delta\mathbf{x}(t_0). \tag{2.60}$$

The Liapunov exponents measure the average rate of expansion or compression of the above quantity and are defined by

$$\lambda = \lim_{t\to\infty} \frac{1}{t} \ln\left(\frac{|\delta\mathbf{x}(t)|}{|\delta\mathbf{x}(t_0)|}\right).$$

It proves convenient to estimate the Liapunov exponents by starting and ending the computation at firing times, therefore using Eq. (2.60) and the definition of the matrix B we have

$$\delta\mathbf{x}(t_n) = M_n\delta\mathbf{x}(t_0),$$

where

$$M_n = \begin{pmatrix} M_{n,1} & 0 \\ 0 & 0 \end{pmatrix},$$

with

$$M_{n,1} = \prod_{i=1}^{n} \gamma(t_i)G_{11}(t_i - t_{i-1}). \tag{2.61}$$

The two Liapunov exponents are determined from the eigenvalues of matrix $L_n = M_n M_n^T$. If λ_n is an eigenvalue of the matrix L_n, its corresponding Liapunov exponent, λ is defined by

$$\lambda = \lim_{n\to\infty} \frac{1}{2n} \ln(\lambda_n). \tag{2.62}$$

One of the eigenvalues of the matrix L_n is zero resulting the Liapunov exponent μ such that $\mu \to -\infty$. Therefore, using Eqs. (2.58), (2.61), and (2.62), the largest Liapunov exponent is given by

$$\lambda = \lim_{n\to\infty} \frac{1}{t_n} \ln \prod_{i=1}^{n} \left|\gamma(t_i) G_{11}(\Delta^{i-1})\right|. \tag{2.63}$$

We note that when the RF orbit has subthreshold oscillations, Eq. (2.22) implies

$$\lambda = \alpha + \lim_{n\to\infty} \frac{1}{t_n} \ln \prod_{i=1}^{n} \left|\gamma(t_i)\left[\cos(\omega\Delta^{i-1}) + (L\omega)^{-1}(r + L\alpha)\sin(\omega\Delta^{i-1})\right]\right|, \tag{2.64}$$

and if it has stable node with eigenvalues $\lambda_2 < \lambda_1 < 0$, Eqs. (2.63) and (2.26) gives

$$\begin{aligned}\lambda = \lambda_1 + \lim_{n\to\infty} \frac{1}{t_n} \ln \prod_{i=1}^{n} \Big|(2L\omega)^{-1}\gamma(t_i)\big[(r + L\lambda_1) \\ - (r + L\lambda_2)\exp\left((\lambda_2 - \lambda_1)\Delta^{i-1}\right)\big]\Big|.\end{aligned} \tag{2.65}$$

Therefore, two factors contribute to Liapunov exponent λ; one from the smooth flow between successive firing events and the other from the discontinuity induced by the resetting map.

2.13 Results

Figures 2.9 and 2.11 show the Liapunov exponent (colour coded) associated with Eq. (2.63). At each point in the parameter plane, the Liapunov exponent is approximated over 3000 firing times and the first 100 firing times were ignored as

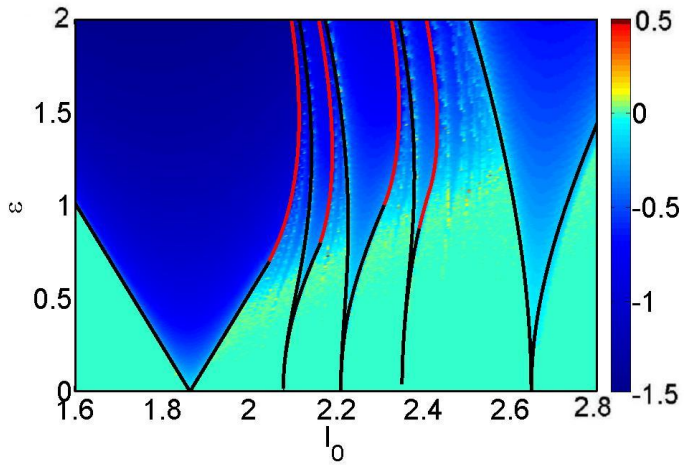

Figure 2.9: The Liapunov exponent of the RF model as a function of I_0 and ϵ. The Liapunov exponent is plotted using Eq. (2.63) for $\omega = 2\pi$ on a mesh of size 300×300. The analytical Arnol'd tongues (lines), as in Fig. 2.6, are also plotted for comparison.

transients. Figure 2.9 shows the Liapunov exponent as a function of I_0 and ϵ for $\omega = 2\pi$. When $\epsilon = 0$, i.e., there is no temporal modulation of the input current, the model displays periodic or quasi-periodic behavior ($\lambda \leq 0$). We observe the Arnol'd tongues emanating from the ϵ axis (compare with analytical Arnol'd tongues (lines)), the largest being the 1:1 tongue. As can be seen, the model does not show chaotic behavior.

Figure 2.10 represents the winding number diagram, the ISI bifurcation diagram, and the Liapunov exponent λ, corresponding to the Arnol'd tongue structure in Fig. 2.9 with $\epsilon = 1$. In panel (a), every step on the devil's staircase is associated with a rational value of $\langle \Delta \rangle^{-1}$ and the winding number in mode-locked regions follows the Farey sequence. In panel (b), we observe periodic solutions at different values of I_0, for example by increasing I_0, we have period-1, period-4, period-3, period-5, and period-2 solutions indicated by labels in the figure. As expected, their corresponding regions exhibit negative Liapunov exponent in panel (c). The

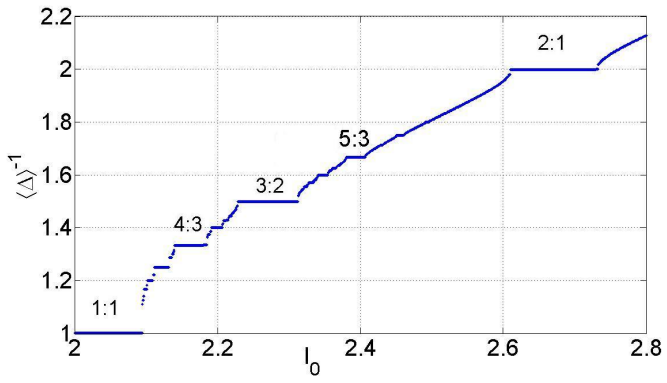

(a)

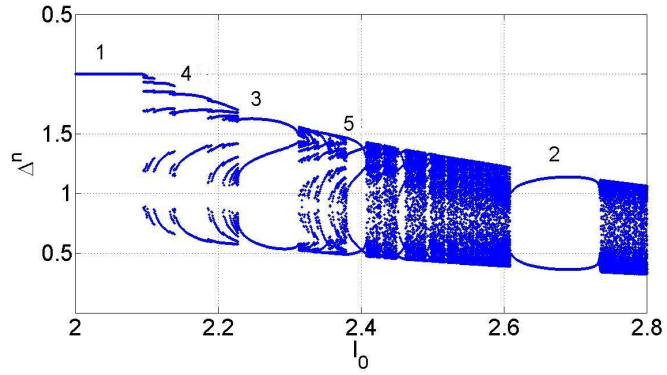

(b)

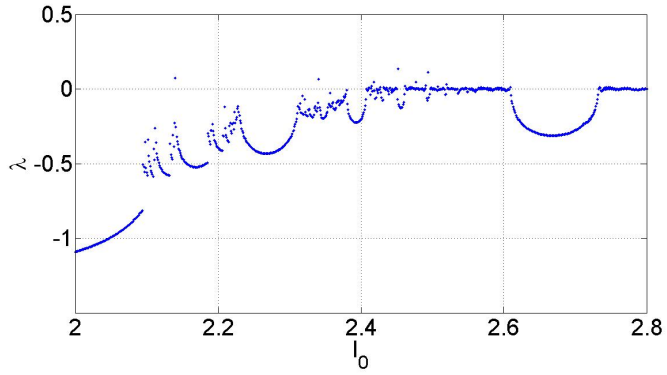

(c)

Figure 2.10: Devil staircase, ISI bifurcation diagram, and Liapunov exponent as a function of I_0 with $\epsilon = 1$. (a) The average firing rate of the RF model. With increasing I_0, we see the dominant mode-locked solutions which are 1:1, 4:3, 3:2, 5:3, and 2:1. (b) The bifurcation diagram ISI, $\Delta^n = t_{n+1} - t_n$ in which lines correspond to periodic solutions. Some periodic regions are indicated with labels showing their period. (c) The Liapunov exponent, λ is either negative or zero. We used 1000 firing times to estimate λ at each value of I_0. Other parameters are as in the caption of Fig. 2.3.

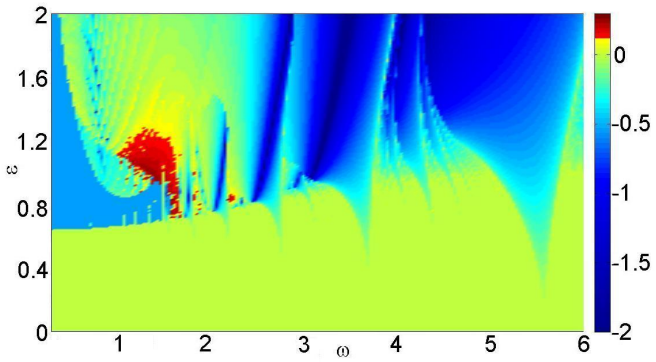

Figure 2.11: The Liapunov exponent of the RF model given in Eq. (2.63) as a function of ϵ and ω with $I_0 = 2.45$. The Liapunov exponent is positive for windows of ω between 1 to 1.86. Other parameters are as in the caption of Fig. 2.3.

Liapunov exponent in panel (c) is either negative or zero and no chaotic behavior is observed. To examine the effect of input frequency on the response properties of the system, we show in Figure 2.11 (colour coded) the Liapunov exponent as a function of the input frequency, ω and the forcing amplitude, ϵ for $I_0 = 2.45$. As seen in Fig. 2.9, when $I_0 = 2.45$, the system does not show chaotic behavior, however here the behavior of the system can move from periodic to chaotic as ω increases and passes through the resonant frequency at approximately $\omega \approx 1.2$. We fix $\epsilon = 1.02$ and represent the impact of varying ω on the interspike interval bifurcation diagram and the Liapunov exponent λ in Fig. 2.12. In the regions of periodic solutions, as expected, we observe negative Liapunov exponents in panel (b). Some intervals of values of ω for which periodic solution exists are indicated with labels in panel (a) of the figure. As ω is reduced, we have windows of periodic solutions alternating with windows of chaotic dynamics.

Besides the existence of chaos, Fig.2.12(a) gives valuable information about the transitions between periodic and chaotic solutions. It reveals the phenomenon of *period adding* [11] bifurcation leading to chaos. As ω is decreased, we see

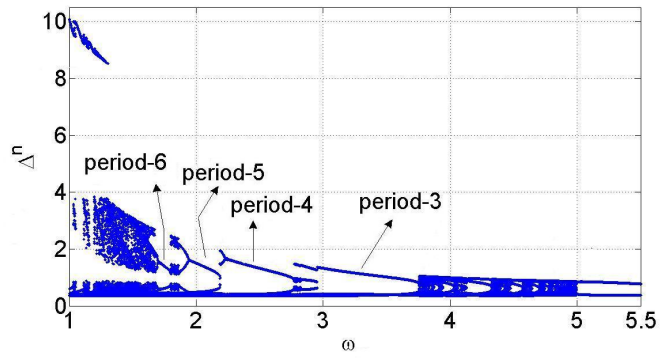

(a)

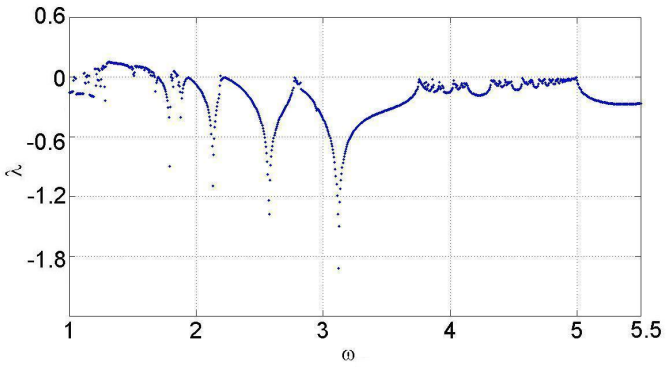

(b)

Figure 2.12: Bifurcation diagrams for ISI and the Liapunov exponent as a function of the input frequency ω with fixing $\epsilon = 1.02$ and $I_0 = 2.45$ in Fig. 2.11. (a) Varying ω, we observe regions of periodic solutions alternating with regions of chaotic solutions. Some of these regions are shown with arrows. (b) For ω near to the resonant frequency, $1.2 < \omega < 1.6$, we observe chaotic behavior corresponds to $\lambda > 0$.

periodic solutions such that their period increases in an arithmetic sequence. In this situation, between periodic solutions of period n and $n+1$, we either observe an interval of ω for which chaotic dynamics occurs or no chaotic behavior occurs and periodic solutions overlap for small intervals of ω. A similar dynamics is observed in square-root map arising as local approximation to the Poincaré maps associated with grazing bifurcations in impacting systems [11]. We discuss this behavior below.

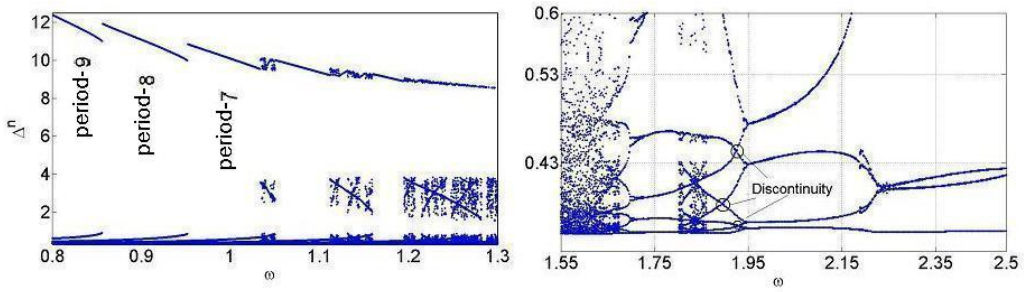

Figure 2.13: The transition leading to chaos. Enlargement of the bifurcation diagram shown in Fig. 2.12(a) in the range of $\omega = 0.8$ to $\omega = 1.3$ (left) and $\omega = 1.55$ to $\omega = 2.5$ (right). The ISI bifurcation diagrams show period-adding phenomenon together with windows of chaotic behavior. The circles indicate the discontinuity points of the firing map.

The transition between periodic and chaotic solutions can be understood more clearly in Fig. 2.13. It shows an enlarged section of Fig. 2.12(a) in the range of $0.8 < \omega < 1.3$ (left) and $1.55 < \omega < 2.5$ (right). At $\omega = 2.5$, there is a period-4 solution. By decreasing ω, the period-4 orbit undergoes period doubling at $\omega \approx 2.24$ and thereafter the orbit evolves to period-5 orbit at $\omega \approx 2.19$. Between period-4 and period-5 intervals, there is a small interval of ω where the periodic solutions overlap. Further decreasing ω, the period-5 orbit doubles at $\omega \approx 1.94$ and the orbit then passes through the discontinuities at $\omega \approx 1.93$, $\omega \approx 1.92$, and $\omega \approx 1.85$ (shown with the circles), where we see the intersections in the ISI diagram. At these points, the orbit crosses threshold tangentially which corresponds to the discontinuities of the firing map. The dynamics within the range of $1.8 < \omega < 1.86$ becomes chaotic. As ω is lowered from 1.8, period-6 orbit appears. Then the orbit doubles at $\omega \approx 1.7$, giving rise to a chaotic interval in the range of $1.3 < \omega < 1.67$.

For $1 < \omega < 1.3$, we observe alternating windows of periodic and chaotic solutions as ω is decreased. Thereafter, decreasing ω in the range of $\omega = 1$ to

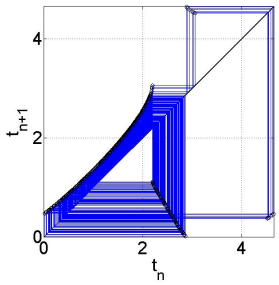

(a) $I_0 = 2.45, \epsilon = 1.02, \omega = 1.35$.

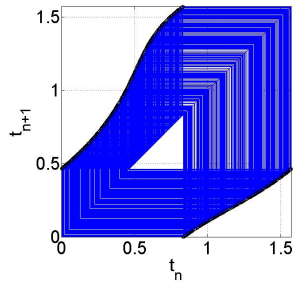

(b) $I_0 = 2.42, \epsilon = 0.5, \omega = 4$.

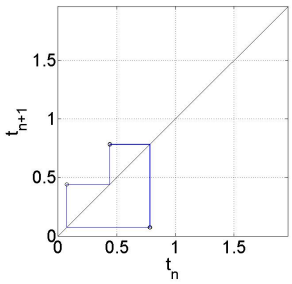

(c) $I_0 = 2.45, \epsilon = 1.23, \omega = 3.21$.

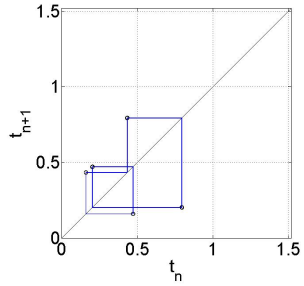

(d) $I_0 = 2.45, \epsilon = 1.97, \omega = 4.14$.

Figure 2.14: Cobweb diagrams for the firing map (2.33). (a) Chaotic solution, (b) quasi-periodic behavior, (c) period-3 solution, and (d) period-5 solution. Other parameters are as in Fig. 2.3.

$\omega = 0.8$, we have period-adding scenario without chaotic intervals. At $\omega = 1$, we have period-7 orbit which evolves smoothly to period 8 at $\omega \approx 0.95$, then the period-8 orbit gives rise to a period-9 orbit at $\omega = 0.85$. Notice that there is overlapping between these periodic orbits for small range of ω. A useful way of studying one-dimensional maps is via cobweb diagrams which plot t_{n+1} against t_n. Examples of cobweb diagram for the RF firing map are shown in Fig. 2.14. As can be seen by varying parameters, the system may have (a) chaotic, (b) quasi-periodic, and (c,d) periodic behavior.

Finally we examine the fact that RF model neurons can be reduced to LIF neurons in large r limit. We consider the parameters $r = 800$, $L = 0.01$, and $C = 1$ with forcing frequency $\omega = 2\pi$ and constant current $I_0 = 2$. For the

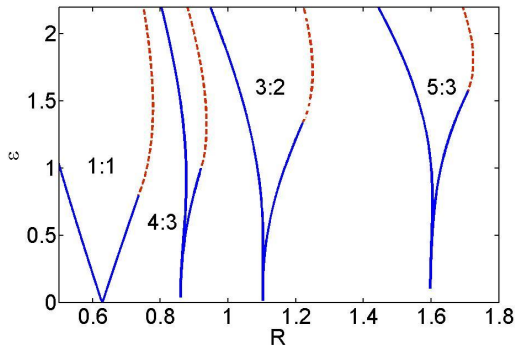

Figure 2.15: The Arnol'd tongues of the RF system in the limit of large r. The boundaries of the tongues are determined by both tangent bifurcations (solid lines) and grazing bifurcations (dashed lines). The parameters are $\omega = 2\pi$, $I_0 = 2$, $r = 800$, $L = 0.01$, and $C = 1$. This result is compatible with that of the IF system shown in [34].

sake of consistency with the result on Arnol'd tongues for the IF system given in [30, 34], we show the bifurcation diagram in (ϵ, R) plane. The analytical result is given in Fig. 2.15 where solid and dashed lines demonstrate tangent and grazing bifurcations respectively. This is in good agreement with the results shown in [34].

2.14 Numerical methods

The numerical methods we have used for the analysis of the RF system are composed of direct numerical simulations and numerical continuations.

To determine the solution of the RF system, direct numerical simulation methods can be used in an event-driven manner. That is for a given initial state $\mathbf{x}_0$ satisfying $h(\mathbf{x}_0, t_0) < 0$, the RF system is solved either exactly or via a higher-order accurate time-stepping scheme such as the Runge-Kutta method. Then, the threshold function $h(\mathbf{x}, t) = V - k(t)$ is monitored and a change of sign is determined using an in-built threshold crossing detector of the time-stepping

algorithm. Therefore, the firing time is calculated accurately and after resetting the solution, it is used as the initial condition for the next calculation. A key requirement for this method is the ability to define the threshold as the zero set of a smooth function h. Thus, the time-integration of the trajectory of the RF system is reduced to the finding of a set of firing times t_n such that $h(\mathbf{x}(t_n), t_n) = 0$. We used this direct numerical simulation for computing the bifurcation diagrams. As an example, in ISI bifurcation diagrams we have taken a fixed parameter value and computed Δ^n for a large number of spike trains, after ignoring some initial spikes for transients, the ISI was plotted. The parameter was then changed slightly and the same process was repeated [see Figs. 2.10(b) and 2.12 (a)].

The numerical simulation, however, cannot pinpoint bifurcation points accurately. Hence, there is a real need for direct methods to compute specific types of solutions of the system. These comprise methods for detecting bifurcation points (either smooth or nonsmooth) and the numerical continuation of these points as one parameter varies in two-parameter (or more) space. A general explanation of these methods are given in [147] and [89] (chapter 10) and the most efficient softwares are XPPAUT [47] and AUTO [41].

Here, we explain key ideas applied to the continuation of solutions, for example in constructing Arnol'd tongues in Figs. 2.6 and 2.15. As we discussed before, a $p : q$ mode-locked solution is determined by simultaneous solving of p equations (2.33) and computing p firing phases $\Phi = (\phi_0, \ldots, \phi_{p-1})$. The mode-locked solution can lose stability either via smooth or nonsmooth bifurcations. The problem of finding the stability region of the $p : q$ mode-locked solution is entirely

equivalent to computing equilibrium solutions of the following smooth system

$$\frac{d\phi_n}{dt} = F_n(\Phi, \epsilon), \qquad n = 0, \dots, p-1, \tag{2.66}$$

$$\frac{d\epsilon}{dt} = H(\Phi, \epsilon), \tag{2.67}$$

where F_n is given in Eq. (2.36) and function H is for detection of smooth or grazing bifurcations which is defined as below.

To determine tangent bifurcation, we define $H = \kappa(p) - 1$, see Eq. (2.43), and in the case of period-doubling bifurcation, we have $H = \kappa(p) + 1$, see Eq. (2.44). When type 2 grazing occurs, we have $H = V'(\phi_n)$, with $n \in \{0, \dots, p-1\}$. In this way, care should be taken to determine at which firing phase ϕ_n, the graze arises and each case should be considered separately. In the case of type 1 grazing, the graze occurs at a new firing phase, ϕ_{new} and between two existing phases of ϕ_n and ϕ_{n+1} where $n \in \{0, \dots, p-1\}$. Therefore, we define $\Phi = (\phi_0, \dots, \phi_n, \phi_{new}, \phi_{n+1}, \dots, \phi_{p-1})$ and instead of Eq. (2.67), we append two differential equations to Eq. (2.66). These equations are

$$\frac{d\phi_{new}}{dt} = H_1(\Phi, \epsilon), \quad \phi_n < \phi_{new} < \phi_{n+1}.$$
$$\frac{d\epsilon}{dt} = H_2(\Phi, \epsilon),$$

where $H_1 = V(\phi_{new}) - 1$ and $H_2 = V'(\phi_{new})$ (see Eqs. (2.47) and (2.48) for details). Again, we should specify between which two existing phases, the phase ϕ_{new} occurs.

Therefore, for each three cases of tangent, period doubling, and type 2 grazing bifurcations, we have a system of $p+1$ nonlinear equations and for type 1 grazing bifurcation, we have a system of $p+2$ nonlinear equations. It proves

convenient to write a general form for all the above cases as below

$$\frac{dX}{dt} = \mathcal{F}(X, \mu), \quad \mathcal{F} : \mathbb{R}^n \times \mathbb{R} \to \mathbb{R}^n, \tag{2.68}$$

where μ is a system parameter. The general setting is to find paths in the parameter space of the smooth parametrized system that takes the form of

$$\mathcal{F}(X, \mu) = 0, \tag{2.69}$$

given some initial solutions X_0 and μ_0. The key idea behind numerical continuations is based on the Implicit Function Theorem to compute sequences of points at small interval along the solution curve

$$X(\mu) \cong \{(X_k, \mu_k), k = 0, \ldots, N\}.$$

Note that in our results on Arnol'd tongues, μ is either I_0 or ω. We find continuation of solutions when μ changes and then plot the results in (ϵ, μ) space.

The most commonly used method for solving systems of nonlinear equations is Newton's method, but it is well known that this requires a sufficiently good initial guess in order to converge. For this reason, we first find an equilibrium point for n nonlinear equations (2.68) with another program and then take it as the initial guess for continuations. All features of Arnol'd tongues in Figs. 2.6 and 2.15 are constructed using this method. We use the continuation package AUTO in XPPAUT [47] to compute such fold curves for each tongue.

2.15 Discussion

We have analyzed the response of the RF neuron model to an arbitrary periodic modulation of its input current. The focus was on the occurrence of the

mode-locked solutions and chaotic patterns. We have found that the analytically calculated regions of stability of mode-locked solutions, the Arnol'd tongues, are in excellent agreement with those of the numerical integration of the model [compare Figs. 2.6 and 2.9]. The behavior of the system when periodically forced can be largely understood by tracing boundaries of the Arnol'd tongues. The boundaries of these tongues correspond to either local bifurcations of the firing time map, or grazing bifurcations induced by the discontinuity of the flow. We showed that the behavior of the system can become chaotic when the input frequency is close to the resonant frequency. This is an important result as it was shown that the periodically driven leaky IF oscillators fail to reproduce chaotic behavior [30], whereas this form of behavior has been observed experimentally. Although it is known that some modified IF neuron models subjected to periodic forcing such as the ghostbursting model [90] and IF with threshold fatigue [26] can exhibit chaotic behavior, they cannot describe resonant behavior and are not suitable for modeling resonant neurons. Further, the RF model can be reduced (by choosing a large r) to the leaky IF neuron model and in this case there is a good agreement between the results, see Fig. 2.15. Therefore, we can say the analysis of the periodically forced RF model is a good extension of the previous work related to mode-locked solutions of IF models.

The effect of resonance on the response properties of the periodically forced RF model with noise has been studied in [19, 138]. It was shown that a sufficient amount of noise was necessary for the subthreshold resonance to cause a firing rate resonance. Our results highlight that even in response to the non-noisy periodic inputs, the subthreshold resonance generates chaotic firing events.

As the RF model is a simple neuron model reproducing resonant behavior, it is suitable for further mathematical analysis of network phenomena involving resonant neurons. It is certainly of great interest to understand the effect of noise on the firing events, mode-locked solutions, and the structure of Arnol'd tongues of the RF system. Also, considering the resetting map to reset just the voltage would give a two-dimensional firing map. In this case, it is worth understanding the properties of the firing times and the dynamics in terms of chaotic or periodic behaviors. For two strongly coupled RF models, the synchronization state and the effect of the resetting function have been studied in [121]. Another interesting issue we would like to address is to analyze the response of a weakly connected population of firing RF neurons. One may then investigate the underlying conditions for synchronized or desynchronized states.

Chapter 3

Steady-state EIF neuron subject to fast and slow fluctuations

3.1 Introduction

Cortical neurons receive trains of excitatory and inhibitory inputs originated from presynaptic spikes and produced by a large number of neurons [39]. These presynaptic inputs act as a source of noise and produce substantial subthreshold fluctuations of membrane potentials [6, 39]. Due to the large number of inputs, the diffusion approximation [156, 38, 3] allows one to replace the synaptic inputs by a mean current plus fluctuations around the mean. These inputs are filtered by synapses [14, 18, 40] with a characteristic time τ_s. τ_s can take a wide range of values depending on the type of receptor. It can be small when compared to the membrane time constant τ_m, as for the excitatory AMPA receptor ($\tau_s \approx 2$ ms) or large as for the excitatory NMDA receptor ($\tau_s \approx 50 - 100$ ms). An important question may arise is what is the effect of synaptic filtering on the response properties of a neuron. It has been shown that synaptic filtering can affect spike count

statistics [114], signal transmission features [17] and can be used to detect rare synaptic fluctuations [116]. The aim of this chapter is to study this question for a neuron with a realistic spike generating mechanism; the exponential-integrate-and-fire (EIF) model [52].

There is a long history of the study of synaptic fluctuations in neuron models going back to the work of Knight [84] where the interest was in the LIF neuron response to a noise model. It was shown [84] that noise can simplify the dynamics of the neuronal firing rate. The steady-state firing rate of LIF neurons with white noise has also been known [133, 156] for a long time and the firing rate at network level is analytically studied in references [4, 5, 16].

When white noise is filtered, the analytical calculations become complex and it is no longer possible to find the exact solution for the steady-state firing rate. However, using a population density method introduced in [15], the calculation can be done in two limits of $\tau_s \ll \tau_m$ [14, 17, 51] and $\tau_s \gg \tau_m$ [115, 116]. Brunel and Latham [18] used this method to determine the steady-state firing rate of the QIF neurons receiving fast synaptic fluctuations and Moreno-Bolt and Parga [115, 116] applied similar methods for IF neurons with one type of slow synaptic input and also for the combination of fast and slow synaptic inputs. For other works on the probability density approaches dealing with the effect of synaptic input on the firing-rate response of neuron models see references [127, 85, 16, 66, 123].

Most of these studies, however, consider the class of IF models which are idealized models of real neurons. For this reason, we choose the EIF neuron model, a reduced version of the conductance-based Wang-Buzsáki (WB) model, see Chapter 1. Its dynamics comprises a spike-generating current that increases

exponentially with membrane potential [52]. Recent experimental results have shown that the EIF model can accurately predict spike trains recorded from layer-5 pyramidal cells [8] and in fast spiking interneurons [9].

Our focus in this chapter concerns how synaptic fluctuations both slow and fast affect the firing rate of the EIF neuron in steady state. Then in Chapter 4, we will extend the study to the case of stimulus-dependent synaptic fluctuations and investigate the dynamical response of the model.

The overall organization of this chapter is as follows. First, we give an overview of the EIF neuron and its dynamics in Sec. 3.2. Using a population density method given in Sec. 3.3, we calculate the steady-state firing rate for fast synaptic inputs in Sec. 3.4. This is done mainly by following the analytical approach in [18] which is based on a perturbative expansion [62, 51, 52] of the probability density and the rate density in powers of $\sqrt{\tau_s/\tau_m}$ and finding corrections at each order. In particular, the first correction to the steady-state firing rate of order τ_s/τ_m is computed. Further, the recently developed threshold integration scheme [135, 136] is extended to compute these corrections numerically. Then in Sec. 3.5, we examine how slow noise affects the firing rate. Here, a zeroth-order approximation for the firing rate is given at subthreshold regime. The chapter ends with a discussion in Sec. 3.6.

3.2 The EIF neuron model driven by coloured noise

We consider the EIF model which captures the dynamical properties of neurons where the activation variable of the fast sodium current responsible for the spike initiation can be well described by an exponential function close to spike threshold,

as in the standard HH model [52, 53]. As introduced in Chapter 1, the EIF neuron driven by a filtered synaptic noise satisfies the following differential equations

$$\begin{aligned} \tau_m \frac{dV}{dt} &= f + W, \\ \tau_s \frac{dW}{dt} &= -W + \sigma\sqrt{2\tau_m}\xi(t), \end{aligned} \tag{3.1}$$

where V is the membrane voltage with time constant τ_m, W is an exponentially decaying synaptic current with time constant τ_s and variance $\sigma^2(\tau_m/\tau_s)$ and $\xi(t)$ is a Gaussian white noise with autocorrelation $\langle \xi(t)\xi(s)\rangle = \delta(t-s)$. The function f is defined by $f(V) = E - V + \Delta_T \exp\left((V - V_T)/\Delta_T\right)$ where the first term holds the leakage property of the neuron with resting potential E, and the exponential term represents the spike-generating factor. The parameter V_T is the threshold potential and Δ_T is the sharpness of the spike onset. The voltage is reset to the reset potential V_{re}, once it reaches the threshold potential V_{th}, without resetting $W(t)$. Here, we take the limit $V_{th} \to \infty$. The synaptic current W is considered as noisy input due to the background synaptic activity. Although, in *vivo*, oscillatory inputs also arrive through synapses and should then be included in W, it proves convenient to consider them separately (see Chapter 4).

Our goal is to study the firing rate of the stochastic system (3.1) in two limits of fast ($\tau_s \ll \tau_m$) and slow ($\tau_s \gg \tau_m$) synaptic inputs. In the limit of $\tau_s \to 0$, $W(t)$ becomes white noise and when $\tau_s \to \infty$, we have the noiseless input. Since the input W is fluctuating, the firing rate is determined by averaging the response of the neuron over different realization of the input. It is useful to consider the equivalent case which is the average response of a population of such neurons, non-interacting and each receiving an independent realization of the input noise. The population of these neurons can be described by a probability density

function, $P(V, W, t)$ that is determined by a Fokker-Planck equation [144].

3.3 The Fokker-Planck equation

The Fokker-Planck [144] formalism provides a convenient method to calculate the firing-rate dynamics. The related analytical calculations are complex and it is sometimes impossible to find the exact solution for constant or time-dependent inputs. To treat the problem, an analytical approximation has been proposed in both short [14, 17, 51, 18, 52] and long [18, 116, 118] τ_s limits to calculate corrections to the firing rate in orders of $\sqrt{\tau_s/\tau_m}$ or its inverse (depending on synaptic time constant). Therefore, we define a small parameter $\kappa = \sqrt{\tau_s/\tau_m}$ and a new variable $z = \big(\kappa/\sigma\big)W$ which has unit variance. With this new variable, system (3.1) can be rewritten as

$$\begin{aligned} \tau_m \frac{dV}{dt} &= f(V) + \frac{\sigma}{\kappa} z, \\ \tau_s \frac{dz}{dt} &= -z + \kappa\sqrt{2\tau_m}\xi(t). \end{aligned} \tag{3.2}$$

The two-dimensional Fokker-Planck equation associated with the stochastic equations (3.2) satisfies

$$\partial_t P(V, z, t) + \partial_V J_V(V, z, t) + \partial_z J_z(V, z, t) = \varrho(z, t)\left\{\delta(V - V_{re}) - \delta(V - V_{th})\right\}, \tag{3.3}$$

where $P(V, z, t)$ is the probability density of voltage and current at time t, $J_V(V, z, t)$ is the probability flux of P through V at fixed z and $J_z(V, z, t)$ is the probability flux of P through z at fixed V. The rate density $\varrho(z, t)$ is injected at reset potential V_{re} and it equals the probability flux escaping at threshold V_{th}. The source

and sink terms in Eq. (3.3) are equivalent to boundary conditions

$$J_V(V_{re^+}, z, t) - J_V(V_{re^-}, z, t) = \varrho(z, t), \tag{3.4}$$

$$J_V(V_{th}, z, t) = \varrho(z, t). \tag{3.5}$$

From system (3.2), the probability fluxes take the following form

$$\tau_m J_V(V, z, t) = \big[f(V) + \frac{\sigma}{\kappa} z\big] P(V, z, t), \tag{3.6}$$

$$-\tau_s J_z(V, z, t) = zP(V, z, t) + \partial_z P(V, z, t). \tag{3.7}$$

As $f(V)$ diverges at V_{th}, Eqs. (3.5) and (3.6) give $P(V_{th}, z, t) = 0$ which implies $V = V_{th}$ is an absorbing boundary. Therefore, the instantaneous rate density is defined by

$$\varrho(z, t) = \frac{1}{\tau_m} \lim_{V \to \infty} f(V) P(V, z, t). \tag{3.8}$$

We are interested in the steady-state case, $t \to \infty$, therefore we set $\partial_t P(V, z, t) = 0$ in Eq. (3.3) and consider the time-independent probability density. The steady-state Fokker-Planck equation can then be written as

$$\mathcal{L}P(V, z) = \kappa\sigma z \partial_V P + \kappa^2 \partial_V (fP) - \kappa^2 \tau_m \varrho(z) \delta(V - V_{re}), \tag{3.9}$$

where $\mathcal{L}P(V, z) = \partial_z^2 P(V, z) + \partial_z z P(V, z)$. We solve the two-dimensional Eq. (3.9) using the methods given in [15, 51, 18] which are based on an expansion of the probability density and the rate density in κ and finding the corresponding corrections at successive orders. First we consider the fast synaptic input, $\tau_s \ll \tau_m$.

3.4 Fast synaptic inputs

To solve Fokker-Planck equation in short synaptic time constant ($\kappa \ll 1$), we expand the probability density and rate density as below

$$P(V,z) = \sum_{n=0}^{\infty} \kappa^n P_n(V,z), \tag{3.10}$$

$$\varrho(z) = \sum_{n=0}^{\infty} \kappa^n \varrho_n(z), \tag{3.11}$$

All coefficients of expansion (3.10) have to satisfy the following conditions

$$\int\int P_n(V,z)\,\mathrm{d}z\mathrm{d}V = \delta_{n,0}, \tag{3.12}$$

$$P_n(V_{th},z) = 0, \tag{3.13}$$

$$\lim_{z\to\pm\infty} zP_n(V,z) = 0, \quad \lim_{z\to\pm\infty} \partial_z P_n(V,z) = 0, \quad \lim_{V\to-\infty} VP_n(V,z) = 0, \tag{3.14}$$

where $\delta_{n,0}$ is the Kronecker delta function that is one for $n = 0$ and otherwise it is zero.

An important property of the probability density P is that it has symmetry with respect to z and κ. This is obvious from the Fokker-Planck equation (3.9) by taking $z \to -z$ and $\kappa \to -\kappa$ which imply $P(V,-z)$ is a solution of it. Therefore by noting that

$$P(V,-z) = \sum_{n=0}^{\infty} (-1)^n \kappa^n P_n(V,-z),$$

and matching powers of κ with those in Eq. (3.10), we find for n even, $P_n(V,z)$ is an even function and for n odd is an odd function. In the next sections, this property is used to simplify our calculations.

3.4.1 Steady-state firing probability

We look for the probability density $P(V,z)$ and the rate density $\varrho(z)$ which satisfy Fokker-Planck equation (3.9) and in the form of the power series in κ. At order zero in κ, $P_0(V,z)$ and $\varrho_0(z)$, correspond to the white noise case and each of the next orders gives corrections to $P(V,z)$ and $\varrho(z)$. Substitution of expansions (3.10) and (3.11) into Eq. (3.9) gives the following system of equations

$$\mathcal{L}P_0(V,z) = 0, \tag{3.15}$$

$$\mathcal{L}P_1(V,z) = \sigma z \partial_V P_0(V,z), \tag{3.16}$$

$$\mathcal{L}P_n(V,z) = \sigma z \partial_V P_{n-1} + \partial_V (f P_{n-2}) - \tau_m \varrho_{n-2}(z)\delta(V - V_{re}), \quad n \geq 2. \tag{3.17}$$

Equations (3.15) through (3.17) can be solved order by order to get terms in the κ expansion of the probability density.

3.4.2 Corrections to the probability density and firing rate

We first integrate Eq. (3.9) with respect to V and z and use the fact that $\int \mathcal{L}P \, \mathrm{d}z = 0$. This produces

$$\int_{-\infty}^{V} \int_{-\infty}^{\infty} \partial_V \left[(f + \frac{\sigma}{\kappa} z) P \right] \mathrm{d}z \mathrm{d}V = r\tau_m \Theta(V - V_{re}), \tag{3.18}$$

where r is the total steady-state firing rate defined by $r = \int \varrho(z) \, \mathrm{d}z$ and Θ is the Heaviside function. Then, introducing the notation

$$\langle \cdot \rangle_n = \int_{-\infty}^{\infty} \cdot P_n \, \mathrm{d}z,$$

one can simplify Eq. (3.18) and obtain the following relation between $P_n(V,z)$ and r_n

$$\langle f \rangle_n + \sigma \langle z \rangle_{n+1} = r_n \tau_m \Theta(V - V_{re}), \quad n \geq 0. \tag{3.19}$$

Using even-odd properties of $P_n(V,z)$, it is straightforward to conclude that for n odd, the left-hand side of Eq. (3.19) is zero, resulting $r_{2n+1}=0$. This simplifies our calculations to just finding even-order corrections to the firing rate.

For even-order corrections to the firing rate, we need to calculate $\langle z\rangle_{2n+1}$. Using Eq. (3.17) for odd order, multiplying both sides by z and integrating with respect to z, we determine $\langle z\rangle_{2n+1}$ based on the lower-order terms

$$\langle z\rangle_{2n+1}=-\partial_V\left[\sigma\langle z^2\rangle_{2n}+f\langle z\rangle_{2n-1}\right]+\tau_m\left\{z\right\}_{2n-1}\delta(V-V_{re}), \tag{3.20}$$

where the following definition has been used

$$\left\{z^m\right\}_n=\int_{-\infty}^{\infty}z^m\varrho_n(z)\,\mathrm{d}z. \tag{3.21}$$

Similarly, $\langle z^2\rangle_{2n}$ is obtained by considering Eq. (3.17) for even order, multiplying both sides by z^2, and integrating with respect to z, this gives

$$\langle z^2\rangle_{2n}=\langle 1\rangle_{2n}-\frac{1}{2}\partial_V\left[\sigma\langle z^3\rangle_{2n-1}+f\langle z^2\rangle_{2n-2}\right]+\frac{\tau_m}{2}\left\{z^2\right\}_{2n-2}\delta(V-V_{re}). \tag{3.22}$$

These equations imply that to find the nth order correction to the firing rate, we must calculate the probability density up to order n. This is easier than the similar case in the QIF model [18] where the probability density was calculated up to order $n+2$. In what follows, we compute the first three terms in the κ-expansion of the probability density, namely, P_0, P_1, and P_2 from which we are able to approximate the firing rate as $r=r_0+\kappa^2 r_2$.

Zeroth order

We begin with zeroth order in κ. The solution to Eq. (3.15) can be written as the linear combination of two solutions φ_0 and φ_1 given by

$$\begin{aligned}\varphi_0(z) =& \frac{1}{\sqrt{2\pi}} e^{-z^2/2},\\ \varphi_1(z) =& \sqrt{2\pi} e^{-z^2/2} \int_0^z e^{u^2/2}\, \mathrm{d}u.\end{aligned}$$

Since P_0 is an even function, it is only proportional to $\varphi_0(z)$. Therefore, we conclude

$$P_0(V, z) = Q_0(V)\varphi_0(z), \tag{3.23}$$

where Q_0 needs to be determined. Combining Eqs. (3.19) and (3.20) for $n = 0$ and using Eq. (3.23), we obtain

$$-\partial_V Q_0(V) = -\frac{f(V)}{\sigma^2} Q_0(V) + r_0 \frac{\tau_m}{\sigma^2} \Theta(V - V_{re}). \tag{3.24}$$

The solution to this equation is

$$Q_0(V) = r_0 \frac{\tau_m}{\sigma^2} \int_V^\infty \exp\big(\psi(u, V)\big) \Theta(u - V_{re})\, \mathrm{d}u, \tag{3.25}$$

where

$$\psi(u, V) = \int_u^V \frac{f(w)}{\sigma^2}\, \mathrm{d}w. \tag{3.26}$$

Now, the normalization of the zero-order probability density, Eq. (3.12) implies $\int_{-\infty}^{\infty} Q_0(V)\, \mathrm{d}V = 1$, therefore Eq. (3.25) gives

$$r_0 = \frac{\sigma^2}{\tau_m} \Big[\int_{-\infty}^{\infty} \int_V^\infty \exp\big(\psi(u, V)\big) \Theta(u - V_{re})\, \mathrm{d}u \mathrm{d}V \Big]^{-1}. \tag{3.27}$$

In Appendix A, we will show how to treat this double integral numerically.

First order

Using Eq. (3.23), one can conclude the right hand side of Eq. (3.16) and write

$$\mathcal{L}P_1(V,z) = \sigma z\varphi_0(z)\partial_V Q_0. \tag{3.28}$$

The solution to this equation is given by the sum of the solution of the homogeneous equation $\mathcal{L}P_1 = 0$ and of particular solution of it. Therefore, we find

$$P_1(V,z) = Q_1(V)\varphi_0(z) + \sigma\partial_V Q_0(V)\mathcal{L}^{-1}z\varphi_0(z), \tag{3.29}$$

where

$$\mathcal{L}^{-1}z^m\varphi_0(z) = -\frac{z^m}{m}\varphi_0(z) + (m-1)\mathcal{L}^{-1}z^{m-2}\varphi_0(z), \quad m \geq 1. \tag{3.30}$$

Since P_1 is an odd function and $\mathcal{L}^{-1}z\varphi_0(z) = -z\varphi_0(z)$, we conclude

$$P_1(V,z) = -\sigma z\varphi_0(z)\partial_V Q_0(V). \tag{3.31}$$

Second order

Using the same method as in the first order and combining Eqs. (3.23), (3.30) and (3.31), one can find the solution to Eq. (3.17) for $n = 2$

$$\begin{aligned} P_2(V,z) =& Q_2(V)\varphi_0(z) + \frac{\sigma^2}{2}z^2\varphi_0(z)\partial_V^2 Q_0(V) + \mathcal{L}^{-1}\varphi_0(z)\times \\ & \partial_V\Big[f(V)Q_0(V) - \sigma^2\partial_V Q_0(V) - r_0\tau_m\Theta(V - V_{re})\Big], \end{aligned} \tag{3.32}$$

where we have used the fact that $\varrho_0(z) = r_0\varphi_0(z)$. From Eq. (3.24), the term in brackets on the right-hand side of Eq. (3.32) is zero, hence P_2 becomes

$$P_2(V,z) = Q_2(V)\varphi_0(z) + \frac{\sigma^2}{2}z^2\varphi_0(z)\partial_V^2 Q_0(V). \tag{3.33}$$

Below, we explain how to derive Q_2 from Eq. (3.19). First, we calculate $\langle z\rangle_3$. By noting that $r_0\tau_m = \lim_{V\to\infty} fQ_0$, Eqs. (3.8) and (3.31) result in

$$\varrho_1(z) = \frac{1}{\tau_m}\lim_{V\to\infty} fP_1 = r_0\frac{\sigma}{\Delta_T}z\varphi_0(z),$$

where the second equality follows because in large V limit, $f\partial_V Q_0 \sim -r_0(\tau_m/\Delta_T)$ and consequently $\{z\}_1 = r_0(\sigma/\Delta_T)$. Also, Eq. (3.22) gives

$$\langle z^2\rangle_2 = Q_2 + \frac{3}{2}\sigma^2\partial_V^2 Q_0. \tag{3.34}$$

Replacing the above results into Eq. (3.20), we conclude

$$\langle z\rangle_3 = \sigma\partial_V(f\partial_V Q_0) - \sigma\partial_V Q_2 - \frac{3}{2}\sigma^3\partial_V^3 Q_0 + \sigma r_0\frac{\tau_m}{\Delta_T}\delta(V-V_{re}). \tag{3.35}$$

Now, combining Eqs. (3.19), (3.33) and (3.35), we arrive at

$$\begin{aligned}-\partial_V Q_2 =& -\frac{f}{\sigma^2}Q_2 - \frac{3}{2}f\partial_V^2 Q_0 - \partial_V f\partial_V Q_0 + \frac{3}{2}\sigma^2\partial_V^3 Q_0\\ &- r_0\frac{\tau_m}{\Delta_T}\delta(V-V_{re}) + r_2\frac{\tau_m}{\sigma^2}\Theta(V-V_{re}).\end{aligned} \tag{3.36}$$

After simplifying the right-hand side of Eq. (3.36), we write the solution to the equation as

$$\begin{aligned}Q_2(V) =& \int_V^\infty \Big[\frac{3}{2}\partial_u^2 f(u)Q_0(u) + 2\partial_u f(u)\partial_u Q_0(u)\Big]\exp\big(\psi(u,V)\big)\,\mathrm{d}u\\ &- r_0\tau_m\Big[\frac{1}{\Delta_T} + \frac{3}{2}\frac{f(V_{re})}{\sigma^2}\Big]\exp\big(\psi(V_{re},V)\big)\Theta(V_{re}-V)\\ &+ \frac{r_2}{r_0}Q_0(V) + \frac{3}{2}r_0\tau_m\delta(V-V_{re}).\end{aligned} \tag{3.37}$$

Since $\int\int P_2(V,z)\,\mathrm{d}V\mathrm{d}z = 0$ and $\int \partial_V^2 Q_0(V)\,\mathrm{d}V = 0$, it is easy to see from Eq. (3.33) that $\int Q_2(V)\,\mathrm{d}V = 0$. Therefore by integrating Eq. (3.37) with respect to V, we find the second-order correction to the firing rate

$$\begin{aligned}r_2 =& -r_0\int_{-\infty}^{\infty}\int_V^\infty \Big[\frac{3}{2}\partial_u^2 f(u)Q_0(u) + 2\partial_u f(u)\partial_u Q_0(u)\Big]\exp\big(\psi(u,V)\big)\,\mathrm{d}u\mathrm{d}V\\ &+ r_0^2\tau_m\Big[\frac{1}{\Delta_T} + \frac{3}{2}\frac{f(V_{re})}{\sigma^2}\Big]\int_{-\infty}^{V_{re}}\exp\big(\psi(V_{re},V)\big)\,\mathrm{d}V - \frac{3}{2}r_0^2\tau_m.\end{aligned} \tag{3.38}$$

Using Eqs. (3.27) and (3.38), the steady-state firing rate ca be approximated by

$$r = r_0 + \kappa^2 r_2, \tag{3.39}$$

where the second order contribution to it, r_2 would be negative. In this case, increasing κ decreases r and can lead to a negative firing rate. To treat this problem, we use an alternative expression as in [18] which has the same behavior as Eq. (3.39) up to second order in κ and is defined by

$$r = \frac{r_0}{1 - \kappa^2 (r_2/r_0)}. \tag{3.40}$$

The advantage of this expression is that it stays positive for any τ_s.

In Fig. 3.1, Eqs. (3.39) and (3.40) are plotted together with the results from numerical simulations. The calculations of r_0 and r_2 were done using threshold integration method [135, 136], see Appendix A, and for numerical simulations, Euler-Maruyama method with $dt = 10^{-4}\tau_m$ was used [67]. In Fig. 3.1 (a), we show the firing rate as a function of mean input E for three different values of the noise intensity with short synaptic time constant $\tau_s = 2$ ms. As we see, increasing E and σ increases the firing rate. We also show the steady-state firing rate as a function of τ_s/τ_m for three different regimes: suprathreshold ($E = -45$ mV), subthreshold ($E = -60$ mV), and threshold ($E = -56$ mV) respectively in Figs. 3.1 (b), (c), and (d). In the subthreshold regime, the firing rate decreases monotonically with τ_s, while in suprathreshold regime, it first decreases and then increases with τ_s. As can be seen, the analytical solutions give an accurate approximation to the firing rate of the neuron with fast synapses (such as those with AMPA receptors) with $\tau_s \approx 2$ ms.

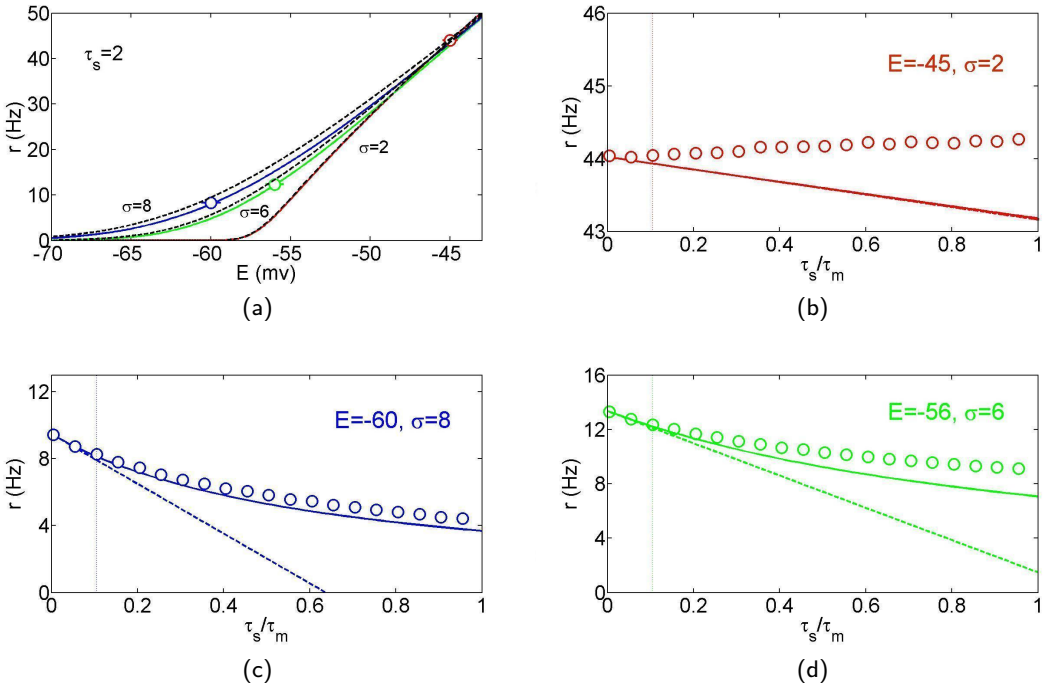

Figure 3.1: Effect of synaptic filtering on the steady-state firing rate. (a) Steady-state firing rate $r = r_0 + \kappa^2 r_2$ (solid lines) as a function of mean input E for three different values of noise intensity σ with synaptic time constant $\tau_s = 2$ ms. The corresponding white noise ($\tau_s = 0$) cases are plotted (dashed lines) for comparison. To exhibit the firing rate as a function of τ_s/τ_m, three different regimes [indicated by full circles (simulation) in panel (a)] are chosen: (b) suprathreshold ($E = -45$ mV and $\sigma = 2$ mV), (c) subthreshold ($E = -60$ mV and $\sigma = 8$ mV), and (d) threshold ($E = -56$ mV and $\sigma = 6$ mV) regimes in which solid lines are Eq. (3.40), dashed lines are Eq. (3.39), and full circles are simulations (the error bars are smaller than the size of symbols). Other parameters are $\tau_m = 20$ ms, $\Delta = 3$ mV, $V_T = -53$ mV, $V_{th} = 0$ mV, and $V_{re} = -60$ mV.

3.5 Slow synaptic inputs

Spikes arriving at many central neurons can be filtered by fast or slow synapses. In this section, we consider the case that presynaptic inputs are filtered by slow synapses e.g., NMDA receptors ($\tau_s \sim 50 - 150$ ms).

We calculate the steady-state firing rate in large τ_s limit ($\kappa \gg 1$) using the

same method as in the case of fast synaptic input but instead of expansions in powers of κ, we expand the probability and rate density in $1/\kappa$

$$P(V,z) = \sum_{0}^{\infty} (1/\kappa)^n P_n(V,z), \tag{3.41}$$

$$\varrho(z) = \sum_{0}^{\infty} (1/\kappa)^n \varrho_n(z). \tag{3.42}$$

Consequently, the even-odd property of $P_n(V,z)$ and $\varrho_n(z)$ are still held. This implies that the odd-order corrections to the firing rate, r_{2n+1} are zero and similar to the fast synaptic case we just calculate firing rate through second order (the lowest non-vanishing order).

We insert Eqs. (3.41) and (3.42) into Fokker Planck equation (3.9) and match powers of κ, this leads to the following equations

$$\partial_V \big[f P_0 - \tau_m \varrho_0(z) \Theta(V - V_{re}) \big] = 0, \tag{3.43}$$

$$\partial_V \big[f P_1 - \tau_m \varrho_1(z) \Theta(V - V_{re}) \big] = -\sigma z \partial_V P_0, \tag{3.44}$$

$$\partial_V \big[f P_n - \tau_m \varrho_n(z) \Theta(V - V_{re}) \big] = -\sigma z \partial_V P_{n-1} + \mathcal{L} P_{n-2}, \quad n \geq 2 \tag{3.45}$$

Before solving these equations, notice that integrating Eq. (3.9) over V and imposing conditions (3.14), result in

$$\int_{-\infty}^{\infty} P_n(V,z) \mathrm{d}V = \delta_{n,0} \varphi_0(z), \quad n \geq 0. \tag{3.46}$$

This states that the probability distribution of z is a normalized Gaussian as we saw in the previous section.

3.5.1 Probability density and rate density

In what follows, we separate two different regimes of suprathreshold and subthreshold and follow the techniques given in [18, 116, 118] to find correction to

the probability density and rate density. In suprathreshold regimes, the depolarizing input E is above threshold level $(E \geq V_T - \Delta_T)$ so that the neuron fires mainly by the mean input current and is not very sensitive to synaptic fluctuations, see Fig. 3.2(b). However in subthreshold regime, the neuron fires only if synaptic input z is greater than the threshold $z_{th} = (\kappa/\sigma)(V_T - E - \Delta_T)$. Because for τ_s large the probability density of z_{th} is low $(z_{th} \to \infty)$, the neuron fires when large (σ large) and rare $(z \geq z_{th})$ fluctuations occur. This situation is shown in Fig. 3.2(a) where for τ_s small, the neuron does not always detect $z(t) > z_{th}$ while for τ_s large, it detects when low probability fluctuations occur. This behavior was also observed for the LIF neuron [116] with long synaptic time constant and in the subthreshold regime.

Suprathreshold

The method for solving Eqs. (3.43)-(3.45) is identical to that used for Eqs. (3.15)-(3.17). Here, solutions can be found easier as the differential operator on the left-hand side of Eqs. (3.43)-(3.45) has a simple form of $\partial_V[\cdot]$ which is straightforward to invert comparing with the operator $\mathcal{L}[\cdot]$ in the previous section.

The solution to Eq. (3.43) for $V \leq V_{th}$ satisfies

$$f(V)P_0(V,z) = \tau_m \varrho_0(z)\Theta(V - V_{re}) + g_0(z),$$

where $g_0(z)$ is constant of integration. Definition of the rate density, Eq. (3.8), results in $g_0(z) = 0$ and therefore

$$P_0(V,z) = \tau_m \varrho_0(z)\frac{\Theta(V - V_{re})}{f(V)}. \tag{3.47}$$

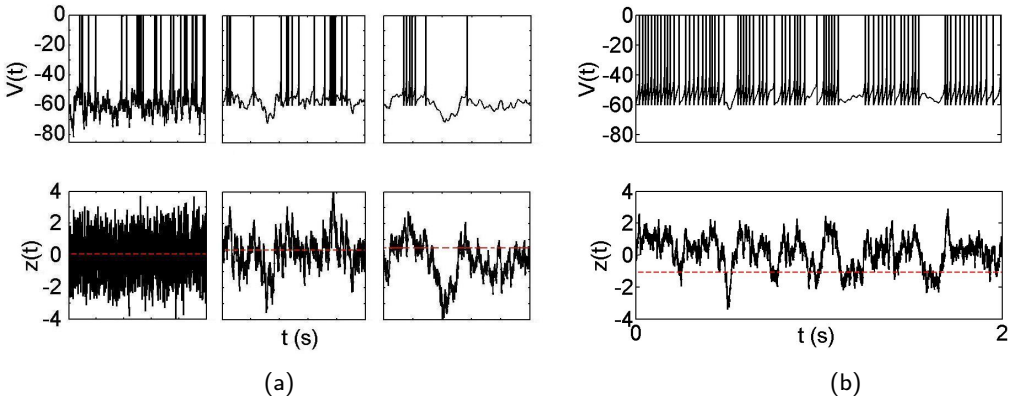

Figure 3.2: Membrane potential $V(t)$ and synaptic fluctuations $z(t)$ for the EIF neuron in subthreshold and suprathreshold regimes. (a) Subthreshold regime with $E = -58$ mV and synaptic time constants $\tau_s = 2$, 40, and 80 ms from left to right. For large τ_s, the neuron fires whenever $z(t)$ is larger than the threshold z_{th} (dashed horizontal line). The time interval for each plot is 2.5 s. (b) Suprathreshold regime with $E = -50$ mV and $\tau_s = 40$ ms. The neuron is not very sensitive to the value of $z(t)$ and is mostly driven by its mean input. Notice that z_{th} is negative. For all cases $\sigma = 8$ mV and the rest of parameters are as before.

Using condition (3.46) and the fact that $r_0 = \int \varrho_0(z)\mathrm{d}z$, we find

$$r_0 = \left[\tau_m \int_{V_{re}}^{\infty} \frac{\mathrm{d}V}{f(V)}\right]^{-1}, \tag{3.48}$$

and

$$\varrho_0(z) = r_0 \varphi_0(z). \tag{3.49}$$

Note that r_0 is the firing rate of the EIF neuron driven with a noiseless current.

Solving Eq. (3.44) gives the first order correction to the probability density as

$$P_1(V,z) = \tau_m \frac{\Theta(V - V_{re})}{f(V)} \left[\varrho_1(z) - \sigma z \frac{\varrho_0(z)}{f(V)}\right]. \tag{3.50}$$

Substituting this into condition (3.46) and noting that

$$\int \frac{\Theta(V - V_{re})}{f^2(V)}\,\mathrm{d}V = -\partial_E \int \frac{\Theta(V - V_{re})}{f(V)}\,\mathrm{d}V,$$

one can conclude

$$\varrho_1(z) = \sigma z \varphi_0(z) \partial_E r_0. \tag{3.51}$$

For the second-order probability density, the solution to Eq. (3.45) is given by

$$\begin{aligned} P_2(V,z) =& \tau_m \frac{\Theta(V-V_{re})}{f(V)}\Big[\varrho_2(z) - \sigma z \frac{\varrho_1(z)}{f(V)} + \sigma^2 z^2 \frac{\varrho_0(z)}{f^2(V)}\Big] \\ &+ \tau_m \frac{\mathcal{L}\varrho_0(z)}{f(V)} \int \frac{\Theta(V-V_{re})}{f(V)}\, \mathrm{d}V. \end{aligned} \tag{3.52}$$

Combining Eqs. (3.49) and (3.51) and using the fact that $\mathcal{L}\varrho_0(z) = 0$, we obtain

$$P_2(V,z) = \tau_m \frac{\Theta(V-V_{re})}{f(V)}\Big[\varrho_2(z) - \sigma^2 \partial_E r_0 \frac{z^2\varphi_0(z)}{f(V)} + \sigma^2 r_0 \frac{z^2\varphi_0(z)}{f^2(V)}\Big]. \tag{3.53}$$

Now the normalization condition, $\int\int P_2\, \mathrm{d}V\, \mathrm{d}z = 0$ implies

$$r_2 = r_0^3\sigma^2\tau_m^2\Big[\int \frac{\Theta(V-V_{re})}{f^2(V)}\, \mathrm{d}V\Big]^2 - r_0^2\sigma^2\tau_m \int \frac{\Theta(V-V_{re})}{f^3(V)}\, \mathrm{d}V. \tag{3.54}$$

Therefore, the second-order correction to the firing rate can be simplified and written as

$$r_2 = \sigma^2 r_0 \partial_E r_0 + \frac{\sigma^2}{2}\big[\partial_E^2 r_0 - 2\frac{(\partial_E r_0)^2}{r_0}\big]. \tag{3.55}$$

Using Eqs. (3.48) and (3.54), the firing rate is approximated through second order in $1/\kappa$ as

$$r = r_0 + \frac{1}{\kappa^2} r_2. \tag{3.56}$$

Here, the same problem as in Eq. (3.39) exists: the firing-rate can become negative with decreasing κ. The alternative expression is

$$r = \frac{r_0}{1 - r_2/(\kappa^2 r_0)}, \tag{3.57}$$

which stay positive for small κ and is equivalent with Eq. (3.56) up to second order in $1/\kappa$.

Subthreshold

Below threshold ($E < V_T - \Delta_T$) the firing of the neuron is mainly controlled by input fluctuations. In this regime, the perturbative expansion in $1/\kappa$ is not defined

and Eqs (3.43)-(3.45) are not valid. We first need to keep the membrane-voltage fluctuations fixed and then use the perturbative approach. This technique was first introduced in [116] to study the effect of thr synaptic filtering on the LIF model without reversal potential and then in [117, 118] for the model with at least one slow synaptic input.

We implement this idea by replacing κ in Eq. (3.6) with a new parameter ϵ and write the steady-state flux as

$$\tau_m J_V(V,z) = \big[f(V) + \frac{\sigma}{\epsilon} z\big] P(V,z),$$

then the steady-state Fokker-Planck equation (3.9) can be rewritten as

$$\mathcal{L}P = \kappa^2 \partial_V \Big[(f + \frac{\sigma}{\epsilon} z)P\Big] - \kappa^2 \tau_m \varrho(z)\delta(V - V_{re}). \tag{3.58}$$

Using expansions (3.41) and (3.42) and to leading order, we have

$$\partial_V \big[(f + \frac{\sigma}{\epsilon} z)P_0 - \tau_m \varrho_0(z)\Theta(V - V_{re})\big] = 0. \tag{3.59}$$

The solution to this equation gives the probability density at zero order as

$$P_0(V,z) = \varrho_0(z)\tau_m \frac{\Theta(V - V_{re})}{f(V) + (\sigma/\epsilon)z} + \varphi_0(z)\delta(V - V^*)\Theta(z_{th} - z), \tag{3.60}$$

where V^* is the stable fixed point of $f(V) + (\sigma/\epsilon)z = 0$. The joint probability density $P_0(V,z)$ has two terms. If input fluctuations are strong enough, $z \geq z_{th}$, the neuron continuously fires with rate density $\varrho_0(z)$, see the first term. In contrast, when $z < z_{th}$, the membrane potential converges very quickly to its resting potential and the probability density has a delta-function form (second term). Replacing Eq. (3.60) into condition (3.46) results in

$$\varrho_0(z) = \varphi_0(z)\Big[\int_{-\infty}^{\infty} \tau_m \frac{\Theta(V - V_{re})}{f + (\sigma/\epsilon)z}\, \mathrm{d}V\Big]^{-1} \Theta(z - z_{th}). \tag{3.61}$$

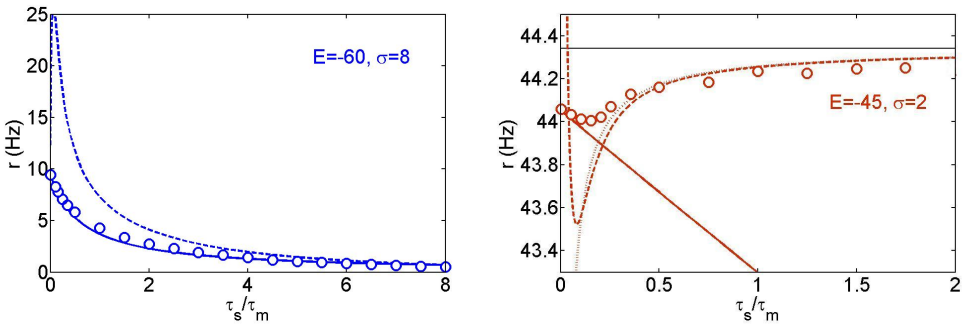

Figure 3.3: Effect of slow synaptic noise on the steady-state firing rate as a function of τ_s/τ_m in sub- and suprathreshold regimes. Dashed lines are slow noise limit given by Eq. (3.62), solid lines are fast noise limit predicted from Eq. (3.40), and symbols are the corresponding numerical simulations. (a) Subthreshold regime ($E = -60$ mV, $\sigma = 8$ mV) and (b) suprathreshold regime ($E = -45$ mV, $\sigma = 2$ mV), dotted line is the firing rate prediction from Eq. (3.57) and the straight line is the limit of $\tau_s \to \infty$.

Now, we can put $\epsilon = 1/\kappa$ and write the firing rate as

$$r_0 = \int_{z_{th}}^{\infty} \varphi_0(z) \Big[\int_{-\infty}^{\infty} \tau_m \frac{\Theta(V - V_{re})}{f + (\sigma/\kappa)z} \, \mathrm{d}V \Big]^{-1} \mathrm{d}z. \tag{3.62}$$

This result indicates that for τ_s large, since the synaptic filter makes the input fluctuations very weak and slow, the synaptic input z can be considered as constant during a time period τ_m. Therefore, it can be assumed that the neuron is driven with input $f(V) + (\sigma/\kappa)z$ with constant z.

Figure 3.3 shows the neuron response as a function of τ_s/τ_m in two regimes of subthreshold, Eq. (3.62), and suprathreshold, Eq. (3.57), together with results from numerical simulations. The corresponding firing rate for $\kappa \ll 1$, given by Eq. (3.40) is also plotted and compared with those for slow noise regime. As we see, the synaptic time constant has different effects on the firing rate in the subthreshold and suprathreshold cases. While in the subthreshold regime (left plot) the firing rate decreases monotonically, in the suprathreshold regime (right plot) firing rate

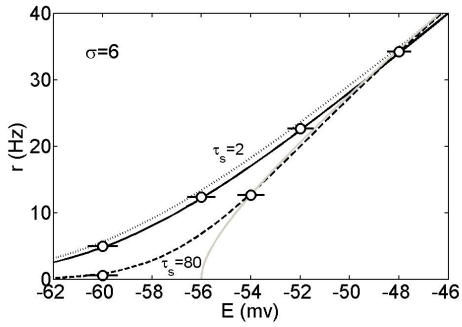

Figure 3.4: Steady-state firing rate as a function of input E when $\sigma = 6$ mV. Dotted line is white noise response, gray solid line is the response to noiseless input, and symbols are simulation results. Firing rate are also plotted in two different limits of synaptic time constants: $\tau_s = 80$ ms (dashed line) calculated from Eq. (3.62) and $\tau_s = 2$ ms (solid line) given by Eq. (3.40). The rest of parameters are as before.

decreases with synaptic time constant for small τ_s but increases with large τ_s and in between there is a minimum. The differences between the firing rate in slow and fast synaptic inputs is also shown in Fig. 3.4. In the suprathreshold regime, the firing rate of the neuron with coloured or white noise are mostly identical. However, in the subthreshold regime the white noise (dotted line) produces larger firing rate compared with coloured noise and as expected, the fast-synaptic noise (black solid line) gives higher firing rate relative to the slow-synaptic noise (dashed line). Noise has also different effects on the firing rate. In short synaptic inputs, the firing rate increases with noise level, while in long synaptic inputs, it decreases with the noise amplitude, see Eq (3.55).

3.6 Discussion

We calculated the steady-state firing rate of the EIF neuron with synaptic fluctuations in two limits of short and long synaptic time constants, τ_s. The calculation were done using expansions of the Fokker-Planck equation in the ratio of τ_s to the

membrane time constant, τ_s/τ_m and finding corrections at each order. In particular, we found that the first correction to the firing rate in small τ_s limit was of order τ_s/τ_m. This implies that the EIF neuron is less sensitive to filtered noise than the LIF neuron in which the firing rate decreases as $\sqrt{\tau_s/\tau_m}$ [51]. For τ_s large, we found a zero-order approximation for the firing rate in subthreshold regime. In this regime, the neuron responds only if large and low probability synaptic fluctuations exist. For both fast and slow filtered fluctuations, the steady-state firing rate increases monotonically with mean inputs and for large noise intensity. It decreases with τ_s in subthreshold regimes and first decreases and then increases in suprathreshold regimes. Similar behavior was observed for LIF neurons [14, 116].

The methods we used here were similar to those for the QIF model with fast synaptic input [18] and for the LIF model with slow synaptic input [116]. Our calculations for the EIF neuron were complicated because of the finite resetting potential imposed in the model leading to a delta function in the Fokker-Planck equation and that the model is less analytically tractable. Although the response properties of the EIF models do not have an analytical solution, they can be extracted via an efficient numerical method [135, 136] allowing for fast calculation.

The influence of the filtering input fluctuations on the neuronal response has been studied for the LIF [14, 17, 51, 115, 116] and QIF models [18, 123, 124]. However, these neuron models lack many dynamical features exhibited by real neurons. The LIF model suffers from unrealistic spike generation mechanism and a pathological behavior close to threshold [52]. The QIF model lacks a crucial dynamical feature: the fast action-potential onset dynamics exhibited by conductance-based neurons [124].

The EIF neuron acts as a neuron model between the LIF and type I HH-type models. Its firing rate in the absence of noise scales as $\sqrt{I - I_{th}}$ where I_{th} is the threshold current [52]. This is the characteristic of type I HH-type neurons near threshold. The EIF model also provides an accurate description of the spike generation mechanism of the HH model. Further, the sharpness of the action potential can be controlled by the parameter Δ_T (for $\Delta_T \to 0$ the LIF is recovered).

As the EIF model is a simple phenomenological, yet dynamically realistic model, it is suitable for further studies of cortical neurons from spike timing to network studies. Another interesting work would be studying the effect of synaptic shot noise on the response properties of the EIF neuron. It is also worth using the results of this chapter to extend the work to more realistic biological conditions, including either the presence of different types of synaptic receptors or a rise time of postsynaptic currents.

Chapter 4

The dynamics response of the EIF neuron with synaptic filtering

4.1 Introduction

The previous chapter studied the steady-state response of the EIF neuron to filtered synaptic fluctuations. Here, our concern is to study the firing-rate dynamics of the model subject to fast synaptic fluctuations when an additional small oscillating signal is added. This allows one to determine the response of the neuron to any time-dependent input with weak temporal variations by using Fourier decomposition.

The response of stochastic neurons (current-based or conductance-based noise) to periodic stimuli has been intensely studied, see [99] and references therein. The investigations are mostly focused on models driven by additive periodic inputs [15, 16, 99, 51, 52, 135] or by noise coded periodic inputs [99, 100, 123, 148, 124, 135]. For cortical neurons which receive trains of excitatory and inhibitory spikes, such an additive periodic input may arise due to temporal changes of the

mean value of these components and for noise coded, the intensity of the noise is assume to be periodic [99].

So far, based on the pioneering work of Knight [84], the firing-rate response of the leaky and perfect IF neurons [21] with white noise in response to the input mean [99, 17, 51] and noise intensity [15, 99, 100, 148] oscillations are analytically obtained. These results are based on population density methods and hypergeometric functions along with numerical simulations. For a simplified noise model, Knight [84] and Gerstner [58] had shown that IF neurons have a finite response to small changes in mean inputs with frequency ω. They found the amplitude of the response was independent of ω and with no phase shift. Interestingly for the IF neuron with white noise, it has been shown [17] that in response to the small oscillatory input mean, the response amplitude decreases as $1/\sqrt{\omega}$ when $\omega \to \infty$ with phase shift decaying to $-\pi/4$, whereas in response to the small amplitude oscillations of the noise intensity, the neuron is able to transmit all input frequencies with phase shift decaying to zero [99]. This finite response at high frequency might account for the high speed processing found, e.g., in visual system [149]. Filtered noise, however, improves the accuracy of the LIF response to the mean input oscillations and introduces a finite response to the high frequent signals [17, 51]. Other works and methods dealing with the firing-rate dynamics of θ-neurons with filtered noise are given in [123, 124].

The firing-rate response of the EIF neuron with white noise is only available numerically using threshold integration method [135, 136] and filtering properties have been computed in [52, 53] in both low- and high-frequency limits. At high-frequency inputs, the EIF response to oscillations in both input mean and noise

intensity decreases as $1/w$, and its phase shifts reach $-\pi/2$. However, a full description of the firing-rate response of the EIF neuron with coloured noise for the whole range of the input frequency is still missing. In particular, it is not clear whether the results found for the white noise case are preserved if one considers coloured noise. The knowledge of the response at all frequencies allows one to determine the response of the neuron to arbitrary stimuli in the linear approximation.

The aim of this chapter is to find the firing-rate response of the EIF model neuron with fast synaptic input to oscillations in both mean inputs and noise intensity. The outline of this chapter is as follows. In Sec. 4.2, we return to the EIF model introduced in the previous chapter and include a small amplitude oscillatory component of mean inputs and noise intensity. Then in Sec. 4.3, the corresponding Fokker-Planck equation is given. Assuming that the driving noise is fast ($\tau_s \ll \tau_m$), the Fokker-Planck equation is solved in the low-frequency limit for both mean inputs and noise intensity oscillations. This is done in Sec 4.4 using similar methods as in Chapter 3 as well as the tools of the dynamical linear response theory [84, 58, 17]. Then, we utilize the threshold integration method to derive linear correction to the firing-rate response. The analytical response in the high-frequency limit is also provided in Sec 4.5 and compared with numerical simulations. Comparison between the responses to mean inputs and noise intensity oscillations is given in Sec 4.6. This chapter ends with a discussion in Sec. 4.7.

4.2 The model

Recalling the EIF neuron model given in Eq. (3.1), we define a small time-dependent perturbation of parameters E and σ respectively as $E(t)$ and $\sigma(t)$ and write the

dynamics of the membrane voltage and synaptic current as

$$\begin{aligned}\tau_m \frac{dV}{dt} &= E(t) - V + \Delta_T \exp((V - V_T)/\Delta_T) + W, \\ \tau_s \frac{dW}{dt} &= -W + \sigma(t)\sqrt{2\tau_m}\xi(t).\end{aligned} \tag{4.1}$$

Similar to the steady-state case, defining the small parameter $\kappa = \sqrt{\tau_s/\tau_m}$ and the new variable $z = \big(\kappa/\sigma(t)\big)W$, system (4.1) can be rewritten as

$$\begin{aligned}\tau_m \frac{dV}{dt} &= E(t) - V + \Delta_T \exp\big((V - V_T)/\Delta_T\big) + \frac{\sigma(t)}{\kappa} z, \\ \tau_s \frac{dz}{dt} &= -z\Big(1 + \tau_s \frac{\sigma'(t)}{\sigma(t)}\Big) + \kappa\sqrt{2\tau_m}\xi(t),\end{aligned} \tag{4.2}$$

where a prime denotes a derivative. The input mean $E(t)$ and noise intensity $\sigma(t)$ are usually assumed to be oscillatory in the following form

$$E(t) = E + \hat{E}\exp(i\omega t), \tag{4.3}$$

$$\sigma(t) = \sigma + \hat{\sigma}\exp(i\omega t), \tag{4.4}$$

where $\hat{E} \ll E$, $\hat{\sigma} \ll \sigma$ and ω is the input frequency (throughout this chapter, a hat always refers to the amplitude of the oscillatory part of the variable).

Considering that the neuron is firing with average rate r, the weak oscillatory component of the input causes a weak oscillations in the firing rate. Since the membrane potential is modeled with a stochastic process, we will consider in the following a population of neurons and a population averaged firing rate, $r(t)$. For each neuron in this population, the membrane potential fluctuations are independent, every neuron, however receives the same oscillatory input. Figure 4.1 shows an example of a numerical simulations of 3000 EIF neurons receiving a common oscillatory current $E(t)$ but with noise inputs that are uncorrelated from neuron to neuron (top panel). By averaging over all responses, the instantaneous firing rate (bottom panel) oscillates in time with the same frequency as the input frequency.

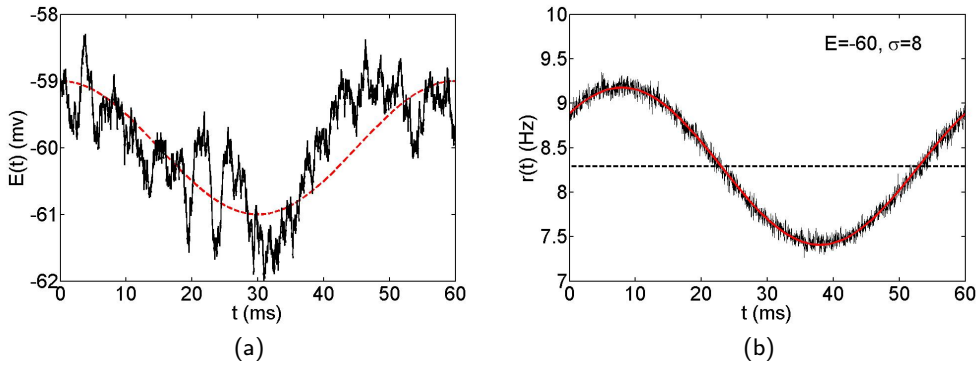

Figure 4.1: Firing rate of the EIF neuron receiving oscillatory current with noise. (a) The scaled noisy input (solid) with $\sigma = 8$ mV together with oscillatory component $E(t) = -60 + \cos(2\pi/60)t$ shown with dashed line. (b) Instantaneous firing rate, $r(t)$ of the neuron averaged over 3000 repetition of the input current with independent noise sources. The steady-state firing rate (dashed line) is $r = 8.29$ Hz.

To linear order, the instantaneous firing rate takes the form of $r(t) = r + \hat{r}(\omega)\exp(i\omega t)$, where r represents the steady-state firing rate and $\hat{r}(\omega)$ is the complex-valued frequency response defined by $\hat{r}(\omega) = \hat{r}\exp(i\theta(\omega))$ in which $\hat{r}$ is the gain of the frequency response and $\theta(\omega)$ is the phase difference between input and response oscillations. We calculate the frequency response using a similar method used for calculating the steady-state firing rate.

4.3 The Fokker-Planck equation

The dynamical Fokker-Planck equation associated with stochastic equations (4.2) satisfies

$$\partial_t \mathcal{P} + \partial_V \mathcal{J}_V + \partial_z \mathcal{J}_z = \nu(z,t)\left\{\delta(V - V_{re}) - \delta(V - V_{th})\right\}, \tag{4.5}$$

where $\mathcal{P}(V,z,t)$ is the probability density and $\mathcal{J}_V(V,z,t)$ and $\mathcal{J}_z(V,z,t)$ are the probability fluxes respectively in V and z direction at time t. From system (4.2),

the probability fluxes are

$$\tau_m \mathcal{J}_V = \left[E(t) - V + \Delta_T \exp\left((V - V_T)/\Delta_T\right) + \frac{\sigma(t)}{\kappa} z\right]\mathcal{P}, \tag{4.6}$$

$$-\tau_s \mathcal{J}_z = z\mathcal{P} + \partial_z \mathcal{P} + \tau_s \frac{\sigma'(t)}{\sigma(t)} z\mathcal{P}. \tag{4.7}$$

Any solution $\mathcal{P}(V, z, t)$ of Eq. (4.5) must obey the boundary conditions

$$\begin{aligned} &\mathcal{P}(V_{th}, z, t) = 0, \\ &\lim_{V \to -\infty} V\mathcal{P}(V, z, t) = 0, \\ &\mathcal{J}_V(V_{th}, z, t) = \nu(z, t). \end{aligned} \tag{4.8}$$

The EIF threshold-crossing and resetting mechanism is captured by the Fokker-Planck equation (4.5) with the source term at $V = V_{re}$ given by $\nu(z,t)\delta(V - V_{re})$, with $\nu(z,t)$ being the rate density of absorption. The rate density is defined by

$$\nu(z, t) = \frac{1}{\tau_m} \lim_{V \to \infty} f(V)\mathcal{P}(V, z, t). \tag{4.9}$$

Using the linear dynamical response [84, 58, 17], we note

$$\mathcal{P}(V, z, t) = P(V, z) + \hat{P}(V, z, \omega)e^{i\omega t}, \tag{4.10}$$

where P is the steady-state component of $\mathcal{P}$ and $\hat{P}$ is a complex quantity describing the oscillatory component at the frequency input ω of $\mathcal{P}$. Similarly, the fluxes and the rate density can be written as

$$\mathcal{J}_z(V, z, t) = J_z(V, z) + \hat{J}_z(V, z, \omega)e^{i\omega t}, \tag{4.11}$$

$$\mathcal{J}_V(V, z, t) = J_V(V, z) + \hat{J}_V(V, z, \omega)e^{i\omega t}, \tag{4.12}$$

$$\nu(z, t) = \varrho(z) + \hat{\varrho}(z, \omega)e^{i\omega t}. \tag{4.13}$$

The steady-state components were obtained in the previous chapter by solving the steady-state Fokker-Planck equation. Here, the linear correction to $\mathcal{P}(V, z, t)$

and $\nu(z,t)$ can be obtained by solving the oscillatory part of the Fokker-Planck equation. Using Eqs. (4.5) and (4.10)-(4.13), the oscillatory part of the Fokker-Planck equation satisfies

$$i\omega\hat{P} + \partial_V \hat{J}_V + \partial_z \hat{J}_z = \hat{\varrho}(z,\omega)\delta(V - V_{re}). \tag{4.14}$$

The techniques to solve Eq. (4.14), similar to the steady-state case, are based on expansions of $\hat{P}(V,z,\omega)$ and $\hat{\varrho}(z,\omega)$ in powers of κ. Therefore, we write

$$\begin{aligned} \hat{P}(V,z,\omega) &= \sum_{n=0}^{\infty} \kappa^n \hat{P}_n(V,z,\omega), \\ \hat{\varrho}(z,\omega) &= \sum_{n=0}^{\infty} \kappa^n \hat{\varrho}_n(z,\omega), \end{aligned} \tag{4.15}$$

Consequently, $\hat{J}_V$ has similar form of expansion in κ. It is straightforward to see that the probability density $\hat{P}_n$ also satisfies the even-odd property obtained for the steady-state probability density P_n.

We reduce the dimension of Eq. (4.14) by integrating both sides of it with respect to z which results in

$$-\partial_V \hat{g} = i\omega \int \hat{P}\, \mathrm{d}z - \hat{r}(\omega)\delta(V - V_{re}), \tag{4.16}$$

where $\hat{g} = \int \hat{J}_V \, \mathrm{d}z$ and

$$\hat{r}(\omega) = \int \hat{\varrho}(z,\omega)\, \mathrm{d}z. \tag{4.17}$$

Using expansions (4.15), we obtain

$$-\partial_V \hat{g}_n = i\omega \langle \hat{1} \rangle_n - \hat{r}_n(\omega)\delta(V - V_{re}), \tag{4.18}$$

where the following notation has been used

$$\langle \hat{\cdot} \rangle_n = \int \cdot \hat{P}_n \, \mathrm{d}z.$$

We shall back to Eq. (4.18) and use it in our calculations. Next, we find solution to Fokker-Planck equation (4.14) in two opposite limits of low frequencies ($\omega \sim 1/\tau_s$) and high frequencies ($\omega \gg 1/\tau_s$).

4.4 Low-frequency regime

We show that in this regime, the first order correction of the firing-rate response to both mean inputs and noise amplitude oscillations vanishes.

4.4.1 Mean inputs oscillations

Considering $E(t) = E + \hat{E}\exp(i\omega t)$, $\sigma(t) = \sigma$ and Eqs. (4.6) and (4.7), the probability fluxes $\hat{J}_V$ and $\hat{J}_z$ are

$$\tau_m \hat{J}_V(V,z,\omega) = \big[f(V) + \frac{\sigma}{\kappa} z\big]\hat{P}(V,z,\omega) + \hat{E}P(V,z), \tag{4.19}$$

$$-\tau_s \hat{J}_z(V,z,\omega) = z\hat{P}(V,z,\omega) + \partial_z \hat{P}(V,z,\omega). \tag{4.20}$$

Therefore, Eq. (4.14) can be rewritten in the form of

$$\mathcal{L}\hat{P} = \kappa\sigma z\partial_V \hat{P} + \kappa^2\big[\partial_V(f\hat{P}) + i\omega\tau_m\hat{P} + \hat{E}\partial_V P\big] - \kappa^2\tau_m\hat{\varrho}(z,\omega)\delta(V - V_{re}). \tag{4.21}$$

Now replacing expansions (4.15) into Eq. (4.21), we obtain the following set of equations

$$\mathcal{L}\hat{P}_0 = 0, \tag{4.22}$$

$$\mathcal{L}\hat{P}_1 = \sigma z\partial_V \hat{P}_0, \tag{4.23}$$

$$\mathcal{L}\hat{P}_n = \partial_V\big[\sigma z\hat{P}_{n-1} + f\hat{P}_{n-2}\big] + i\omega\tau_m\hat{P}_{n-2} + \hat{E}\partial_V P_{n-2} \tag{4.24}$$

$$- \tau_m\hat{\varrho}_{n-2}(z,\omega)\delta(V - V_{re}), \qquad n \geq 2.$$

As explained below, we solve these recurrent equations up to second order to find corrections to the probability-density modulation. Then, the next step will be computing corrections to frequency response, $\hat{r}(\omega)$ using the threshold integration method. By integrating Eq. (4.19) with respect to z, we obtain

$$\tau_m \hat{g}_n = \langle \hat{f} \rangle_n + \sigma \langle \hat{z} \rangle_{n+1} + \hat{E} \langle 1 \rangle_n, \quad n \geq 0. \tag{4.25}$$

This equation together with Eq. (4.18) will be used to derive corrections to $\hat{r}(\omega)$.

Zeroth order

The solution to Eq. (4.22) is given by

$$\hat{P}_0 = \hat{Q}_0(V, \omega)\varphi_0(z), \tag{4.26}$$

where $\hat{Q}_0$ is to be determined. Consequently, one can obtain the solution to Eq. (4.23) as $\hat{P}_1 = \hat{Q}_1(V, \omega)\varphi_0(z) - \sigma z \varphi_0(z)\partial_V \hat{Q}_0(V)$. Since $\hat{P}_1$ is an odd function, therefore $\hat{Q}_1(V, \omega) = 0$ and we conclude

$$\hat{P}_1 = -\sigma z \varphi_0(z) \partial_V \hat{Q}_0. \tag{4.27}$$

Now, Eqs. (4.18) and (4.25) for zero order lead to the following system

$$\begin{aligned} -\partial_V \hat{Q}_0 &= -\frac{f}{\sigma^2}\hat{Q}_0 + \frac{\tau_m}{\sigma^2}\hat{g}_0 - \frac{\hat{E}}{\sigma^2}Q_0, \\ -\partial_V \hat{g}_0 &= i\omega \hat{Q}_0 - \hat{r}_0(\omega)\delta(V - V_{re}), \end{aligned} \tag{4.28}$$

which can be solved to determine $\hat{Q}_0(V, \omega)$ and $\hat{g}_0(V, \omega)$. Boundary conditions $\hat{P}(V_{th}, z, \omega) = 0$ and $\hat{J}_V(V_{th}, z, \omega) = \hat{\varrho}(z, \omega)$ determine the corresponding initial conditions of the system as $\hat{Q}_0(V_{th}, \omega) = 0$ and $\hat{g}_0(V_{th}, \omega) = \hat{r}_0(\omega)$. This system is numerically solved by separating the solution into homogeneous and inhomogeneous parts, indicated respectively by subscripts h and p in the following changing

variables

$$\begin{aligned}\hat{Q}_0 &= \hat{r}_0\hat{Q}_{0,h} + \hat{Q}_{0,p},\\ \hat{g}_0 &= \hat{r}_0\hat{g}_{0,h} + \hat{g}_{0,p},\end{aligned} \tag{4.29}$$

where $\hat{Q}_{0,h}(V_{th},\omega) = 0$, $\hat{g}_{0,h}(V_{th},\omega) = 1$, $\hat{Q}_{0,p}(V_{th},\omega) = 0$ and $\hat{g}_{0,p}(V_{th},\omega) = 0$. Once $\hat{Q}_0$ is obtained, it can be used to find the zero-order correction to the firing-rate response as

$$\hat{r}_0(\omega) = -\frac{\int \hat{Q}_{0,p}\,\mathrm{d}V}{\int \hat{Q}_{0,h}\,\mathrm{d}V}, \tag{4.30}$$

where we have used the fact that $\int \hat{Q}_0\,\mathrm{d}V = 0$. See Appendix A for the details of the numerical method. It is, then, straightforward to see that Eqs. (4.18) and (4.25) for $n = 1$ result in $\hat{r}_1(\omega) = 0$.

Second order

We write the solution to Eq. (4.24) as

$$\hat{P}_2 = \hat{Q}_2(V,\omega)\varphi_0(z) + \hat{P}_2^p, \tag{4.31}$$

where $\hat{P}_2^p$ is the particular solution of it. By noting that

$$\tau_m\hat{\varrho}_0(z,\omega) = \varphi_0(z)\lim_{V\to\infty} f\hat{Q}_0, \tag{4.32}$$

we obtain

$$\begin{aligned}\hat{P}_2^p = \frac{1}{2}\sigma^2 z^2\varphi_0(z)\partial_V^2\hat{Q}_0 + \Big[&\partial_V(f\hat{Q}_0) - \sigma^2\partial_V^2\hat{Q}_0 + i\omega\tau_m\hat{Q}_0 + \hat{E}\partial_V Q_0\\ &- \hat{r}_0\tau_m\delta(V - V_{re})\Big]\mathcal{L}^{-1}\varphi_0(z).\end{aligned} \tag{4.33}$$

From system (4.28), the coefficient of $\mathcal{L}^{-1}\varphi_0(z)$ is zero and thus

$$\hat{P}_2 = \hat{Q}_2(V,\omega)\varphi_0(z) + \frac{1}{2}\sigma^2 z^2\varphi_0(z)\partial_V^2\hat{Q}_0(V,\omega). \tag{4.34}$$

Now, $\hat{r}_2(\omega)$ can be derived using system of equations (4.18) and (4.25) for $n = 2$. For this, we first need to compute $\langle \hat{f} \rangle_2$ and $\langle \hat{z} \rangle_3$. From Eq. (4.34), one can conclude

$$\langle \hat{f} \rangle_2 = f\hat{Q}_2 + \frac{\sigma^2}{2} f \partial_V^2 \hat{Q}_0. \tag{4.35}$$

To compute $\langle \hat{z} \rangle_3$, we consider Eq. (4.24) for $n = 3$

$$\mathcal{L}\hat{P}_3 = \partial_V \left[\sigma z \hat{P}_2 + f\hat{P}_1 \right] + i\omega\tau_m \hat{P}_1 + \hat{E}\partial_V P_1 - \tau_m \hat{\varrho}_1(z,\omega)\delta(V - V_{re}). \tag{4.36}$$

Noting that $\tau_m \hat{\varrho}_1(z,\omega) = -\sigma z \varphi_0(z) \lim_{V\to\infty} f\partial_V \hat{Q}_0$ and inserting it into Eq. (4.36), multiplying the result by z and integrating over z, we find, after some calculations

$$\begin{aligned} \langle \hat{z} \rangle_3 =& \sigma\partial_V(f\partial_V\hat{Q}_0) - \sigma\partial_V\hat{Q}_2 - \frac{3}{2}\sigma^3\partial_V^3\hat{Q}_0 + i\omega\tau_m\sigma\partial_V\hat{Q}_0 + \hat{E}\sigma\partial_V^2 Q_0 \\ &+ \sigma\hat{r}_0\frac{\tau_m}{\Delta_T}\delta(V - V_{re}). \end{aligned} \tag{4.37}$$

Using Eqs. (4.34), (4.35), and (4.37), we write system (4.18) and (4.25) as

$$\begin{aligned} -\partial_V\hat{Q}_2 &= -\frac{1}{\sigma^2} f\hat{Q}_2 + \frac{\tau_m}{\sigma^2}\hat{g}_2 + \hat{\mathcal{E}}_2 + \mathcal{E}_2, \\ -\partial_V\hat{g}_2 &= i\omega\hat{Q}_2 + \mathcal{H}_2 - \hat{r}_2(\omega)\delta(V - V_{re}), \end{aligned} \tag{4.38}$$

where

$$\begin{aligned} \hat{\mathcal{E}}_2(V,\omega) =& -\frac{3}{2} f\partial_V^2\hat{Q}_0 - \partial_V f\partial_V\hat{Q}_0 + \frac{3}{2}\sigma^2\partial_V^3\hat{Q}_0 - i\omega\tau_m\partial_V\hat{Q}_0 \\ &- \hat{r}_0\frac{\tau_m}{\Delta_T}\delta(V - V_{re}), \end{aligned} \tag{4.39}$$

$$\mathcal{E}_2(V) = -\frac{1}{\sigma^2}\hat{E}Q_2 - \frac{3}{2}\hat{E}\partial_V^2 Q_0, \tag{4.40}$$

$$\mathcal{H}_2(V) = i\omega\frac{\sigma^2}{2}\partial_V^2\hat{Q}_0. \tag{4.41}$$

The initial conditions of the system are $\hat{Q}_2(V_{th},\omega) = 0$ and $\hat{g}_2(V_{th},\omega) = \hat{r}_2$. In the same way as for zero order, system (4.38) is numerically solved by changing

variables

$$\begin{aligned}\hat{Q}_2 &= \hat{r}_2\hat{Q}_{2,h} + \hat{Q}_{2,p},\\ \hat{g}_2 &= \hat{r}_2\hat{g}_{2,h} + \hat{g}_{2,p},\end{aligned} \tag{4.42}$$

such that $\hat{Q}_{2,h}(V_{th},\omega) = 0$, $\hat{g}_{2,h}(V_{th},\omega) = 1$, $\hat{Q}_{2,p}(V_{th},\omega) = 0$ and $\hat{g}_{2,p}(V_{th},\omega) = 0$. Therefore, using the fact that $\int \hat{Q}_2 \, \mathrm{d}V = 0$, the second-order correction to the firing-rate response is given by

$$\hat{r}_2(\omega) = -\frac{\int \hat{Q}_{2,p} \, \mathrm{d}V}{\int \hat{Q}_{2,h} \, \mathrm{d}V}. \tag{4.43}$$

Using Eqs. (4.30) and (4.43), the frequency response is approximated by

$$\hat{r}(\omega) = \hat{r}_0(\omega) + \kappa^2\hat{r}_2(\omega). \tag{4.44}$$

4.4.2 Noise amplitude oscillations

In this section, the firing-rate response to oscillations of the noise intensity is discussed. We consider $\sigma(t) = \sigma + \hat{\sigma}\exp(i\omega t)$ and $E(t) = E$. Here, our calculations follow exactly those given for the mean input oscillations so we pass over the details.

Using the fact that $\hat{\sigma} \ll \sigma$, one can approximate $\sigma'(t)/\sigma(t) \approx (\hat{\sigma}/\sigma)i\omega\exp(i\omega t)$ that together with Eqs. (4.6) and (4.7) define the fluxes as

$$\tau_m\hat{J}_V(V,z,\omega) = \big[f(V) + \frac{\sigma}{\kappa}z\big]\hat{P}(V,z,\omega) + \frac{\hat{\sigma}}{\kappa}zP(V,z), \tag{4.45}$$

$$-\tau_s\hat{J}_z(V,z,\omega) = z\hat{P}(V,z,\omega) + \partial_z\hat{P}(V,z,\omega) + \frac{\hat{\sigma}}{\sigma}i\omega\tau_s zP(V,z). \tag{4.46}$$

Now, we rewrite Fokker-Planck equation (4.14) in the form of

$$\begin{aligned}\mathcal{L}\hat{P} =& \kappa z\partial_V\big(\hat{\sigma}P + \sigma\hat{P}\big) + \kappa^2\partial_V(f\hat{P}) + \kappa^2 i\omega\tau_m\hat{P}\\ &- \kappa^2\frac{\hat{\sigma}}{\sigma}i\omega\tau_m\partial_z(zP) - \kappa^2\tau_m\hat{\varrho}(z,\omega)\delta(V - V_{re}),\end{aligned} \tag{4.47}$$

and use expansions (4.15) to obtain the following set of equations

$$\mathcal{L}\hat{P}_0 = 0, \tag{4.48}$$

$$\mathcal{L}\hat{P}_1 = \sigma z \partial_V \hat{P}_0 + \hat{\sigma} z \partial_V P_0, \tag{4.49}$$

$$\begin{aligned}\mathcal{L}\hat{P}_n =& \partial_V z\left[\hat{\sigma} P_{n-1} + \sigma \hat{P}_{n-1}\right] + \partial_V (f \hat{P}_{n-2}) + i\omega\tau_m \hat{P}_{n-2} \\ &- \frac{\hat{\sigma}}{\sigma} i\omega\tau_m \partial_z (z P_{n-2}) - \tau_m \hat{\varrho}_{n-2}(z,\omega)\delta(V - V_{re}), \qquad n \geq 1.\end{aligned} \tag{4.50}$$

Also, integrating Eq. (4.45) over z results in

$$\tau_m \hat{g}_n = \langle \hat{f} \rangle_n + \sigma \langle \hat{z} \rangle_{n+1} + \hat{\sigma} \langle z \rangle_{n+1}, \quad n \geq 0. \tag{4.51}$$

We will use this equation to obtain corrections to $\hat{r}(\omega)$.

Zeroth order

The solution to Eqs. (4.48) and (4.49) can be written, respectively, as

$$\hat{P}_0 = \hat{Q}_0(V,\omega)\varphi_0(z), \tag{4.52}$$

$$\hat{P}_1 = -\left[\sigma \partial_V \hat{Q}_0(V,\omega) + \hat{\sigma}\partial_V Q_0(V)\right] z\varphi_0(z). \tag{4.53}$$

We determine $\hat{Q}_0$ by solving Eqs. (4.18) and (4.51) for zero order

$$\begin{aligned}-\partial_V \hat{Q}_0 &= -\frac{f}{\sigma^2}\hat{Q}_0 + \frac{\tau_m}{\sigma^2}\hat{g}_0 + \frac{2\hat{\sigma}}{\sigma}\partial_V Q_0, \\ -\partial_V \hat{g}_0 &= i\omega\hat{Q}_0 - \hat{r}_0(\omega)\delta(V - V_{re}),\end{aligned} \tag{4.54}$$

with initial conditions $\hat{g}_0(V_{th},\omega) = \hat{r}_0(\omega)$ and $\hat{Q}_0(V_{th},\omega) = 0$. Since $\int \hat{Q}_0 \mathrm{d}V = 0$, the zero-order contribution to the firing-rate response is given by

$$\hat{r}_0(\omega) = -\frac{\int \hat{Q}_{0,p}\, \mathrm{d}V}{\int \hat{Q}_{0,h}\, \mathrm{d}V}, \tag{4.55}$$

where $\hat{Q}_{0,p}$ and $\hat{Q}_{0,h}$ are as in Eq. (4.29).

For first-order correction, $\hat{r}(\omega)$, it is easy to conclude from even-odd property of $\hat{P}$ and Eqs. (4.18) and (4.51) that $\hat{r}_1(\omega) = 0$.

Second order

For $n = 2$, the solution to Eq. (4.50) is given by

$$\begin{aligned}\hat{P}_2 = \hat{Q}_2(V,\omega)\varphi_0(z) + \frac{1}{2}z^2\varphi_0(z)\big[\sigma^2\partial_V^2\hat{Q}_0(V,\omega) + 2\sigma\hat{\sigma}\partial_V^2 Q_0(V) \\ - \frac{\hat{\sigma}}{\sigma}i\omega\tau_m Q_0(V)\big].\end{aligned} \tag{4.56}$$

In the same way as in the previous section, we calculate $\hat{\langle z\rangle}_3 = \hat{\mathcal{Z}} + \mathcal{Z}$ where

$$\begin{aligned}\hat{\mathcal{Z}} =& \sigma\partial_V(f\partial_V\hat{Q}_0) - \sigma\partial_V\hat{Q}_2 - \frac{3}{2}\sigma^3\partial_V^3\hat{Q}_0 + i\omega\tau_m\sigma\partial_V\hat{Q}_0 \\ &+ \sigma\hat{r}_0\frac{\tau_m}{\Delta_T}\delta(V - V_{re}),\end{aligned} \tag{4.57}$$

$$\begin{aligned}\mathcal{Z} =& \hat{\sigma}\partial_V(f\partial_V Q_0) - \hat{\sigma}\partial_V Q_2 - \frac{9}{2}\sigma^2\hat{\sigma}\partial_V^3 Q_0 + \frac{7}{2}i\omega\tau_m\hat{\sigma}\partial_V Q_0 \\ &+ \hat{\sigma}r_0\frac{\tau_m}{\Delta_T}\delta(V - V_{re}).\end{aligned} \tag{4.58}$$

Therefore, substituting Eqs. (4.56)-(4.58) into system of equations (4.18) and (4.51) with $n = 2$, we obtain

$$\begin{aligned}-\partial_V\hat{Q}_2 &= -\frac{1}{\sigma^2}f\hat{Q}_2 + \frac{\tau_m}{\sigma^2}\hat{g}_2 + \hat{\mathcal{E}}_2 + \mathcal{E}_2, \\ -\partial_V\hat{g}_2 &= i\omega\hat{Q}_2 + \mathcal{H}_2 - \hat{r}_2(\omega)\delta(V - V_{re}),\end{aligned} \tag{4.59}$$

where $\hat{\mathcal{E}}_2$ is given in Eq. (4.39) and

$$\begin{aligned}\mathcal{E}_2(V,\omega) =& -\frac{3\hat{\sigma}}{\sigma}f\partial_V^2 Q_0 - \frac{2\hat{\sigma}}{\sigma}\partial_V f\partial_V Q_0 + \frac{2\hat{\sigma}}{\sigma}\partial_V Q_2 + 6\hat{\sigma}\sigma\partial_V^3 Q_0 \\ &+ \frac{\hat{\sigma}}{2\sigma^3}i\omega\tau_m f Q_0 - \frac{7}{2}\frac{\hat{\sigma}}{\sigma}i\omega\tau_m\partial_V Q_0 - \frac{2\hat{\sigma}}{\sigma}r_0\frac{\tau_m}{\Delta_T}\delta(V - V_{re}),\end{aligned} \tag{4.60}$$

$$\mathcal{H}_2(V,\omega) = i\omega\big[\frac{\sigma^2}{2}\partial_V^2\hat{Q}_0 + \sigma\hat{\sigma}\partial_V^2 Q_0 - \frac{\hat{\sigma}}{2\sigma}i\omega\tau_m Q_0\big]. \tag{4.61}$$

In order to find $\hat{r}_2(\omega)$, we solve system (4.59) with initial conditions $\hat{Q}_2(V_{th},\omega) = 0$ and $\hat{g}_2(V_{th},\omega) = \hat{r}_2$. Since $\int \hat{Q}_2\,\mathrm{d}V = (\hat{\sigma}/2\sigma)i\omega\tau_m$, we find

$$\hat{r}_2(\omega) = \frac{(\hat{\sigma}/2\sigma)i\omega\tau_m - \int \hat{Q}_{2,p}\,\mathrm{d}V}{\int \hat{Q}_{2,h}\,\mathrm{d}V}, \tag{4.62}$$

where $\hat{Q}_{2,p}$ and $\hat{Q}_{2,h}$ are as in Eq. (4.42).

4.5 High-frequency inputs

We now explain how to analytically calculate the asymptotic decay of $\hat{r}(\omega)$ in high-frequency limits [52, 53].

4.5.1 Mean inputs oscillations

From Eqs. (4.9) and (4.17), the firing-rate response is given by

$$\hat{r}(\omega) = \frac{1}{\tau_m} \lim_{V\to\infty} f(V) \int \hat{P}(V, z, \omega)\, \mathrm{d}z. \tag{4.63}$$

In the limit of high-frequency inputs ($\omega\tau_s \gg 1$), expanding Fokker-Planck equation (4.21) in powers of $1/\omega$ and keeping only the leading order give

$$\hat{P}(V, z, \omega) = -\frac{\hat{E}}{i\omega\tau_m}\partial_V P(V, z) + O(\frac{1}{\omega^2}). \tag{4.64}$$

Since in large V limit, $f(V)P(V, z) \sim \varrho(z)\tau_m$, therefore

$$\int \partial_V P(V, z)\, \mathrm{d}z \sim \lim_{V\to\infty} -r\tau_m \frac{f'(V)}{f^2(V)}. \tag{4.65}$$

Now, combining Eqs. (4.63)-(4.65), one can write the first term in expansion in $1/\omega$ of $\hat{r}(\omega)$ as

$$\hat{r}(\omega) \sim \frac{r\hat{E}}{i\omega\tau_m\Delta_T}, \tag{4.66}$$

resulting a phase shift of $-\pi/2$ at large ω. The response is inversely proportional to Δ_T, this can be implicated as the faster the neuron can spike, the better it can transmit high frequent inputs.

This result holds for both white and coloured noise input [52] as well as for multiplicative noise (corresponding to conductance-based synaptic inputs). Thus, the qualitative behavior of the high-frequency response is independent of the noise

level or model, in contrast with the LIF model. Rather, it is determined by the shape of function $f(V)$. The reason is that the spike-generating current completely determines the dynamics at sufficiently large voltage and the dynamics becomes independent of the noise fluctuations at such large voltage [52].

In Fig. 4.2, the amplitude and phase of the EIF neuron response to oscillations in E are plotted. We show the results for low- and high-frequency limits and compare them with the results of numerical simulations. At low frequency, the calculations of $\hat{r}_0$ and $\hat{r}_2$, given by Eqs. (4.30) and (4.43), were done using threshold integration method (see Appendix A). For comparison, we also plotted the response of the EIF model with white noise [135].

These results show that at high-noise level (upper panels), the firing events become irregular and the response to an oscillation in E becomes that of a low-pass filter. At low-noise level (lower panels), the response displays resonances at frequencies multiple of the steady-state firing rate r. This is because in this regime the firing events are close to periodic and hence the frequency response resonates with inputs at frequency multiple of the firing rate r. The maximum transmission frequency is approximately determined by r (straight line in panel (c)). The responses to white and coloured noise are very similar. At high-noise levels, the amplitude of the response to coloured noise is slightly smaller than the one to white noise. It should be noted that the low-input frequency attenuation is similar to that of the LIF neuron, while the high-frequency attenuation is induced by spike-generating mechanism [52].

In the high-frequency limit (dashed lines), the amplitude of the frequency response in both cases of high and low-noise levels decays like $1/\omega$ according to

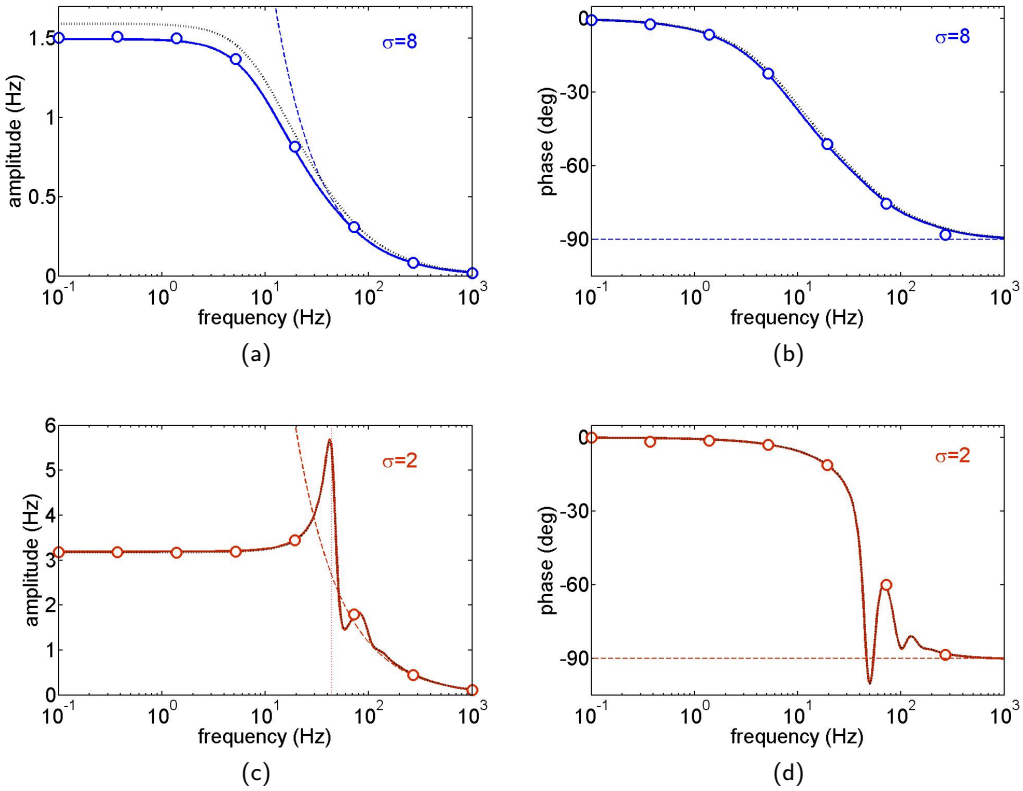

Figure 4.2: Effect of fast synaptic input ($\tau_s = 2$ ms) on the amplitude and phase of the EIF neuron response to mean input oscillations. Solid lines indicate the numerical solutions using Eqs. (4.30) and (4.43) for $\hat{r}(\omega) = \hat{r}_0(\omega) + \kappa^2 \hat{r}_2(\omega)$, symbols represent simulation results, dashed lines indicate the high-frequency limit predicted by Eq. (4.66), and dotted lines are the numerical solution for the corresponding white noise cases. (a,b) Subthreshold high noise regime ($E = -60$ mV, $\hat{E} = 1$ mV, $\sigma = 8$ mV, $r = 7.98$ Hz) and (b,c) suprathreshold low-noise regime ($E = -45$ mV, $\hat{E} = 1$ mV, $\sigma = 2$ mV, $r = 43.93$ Hz), the straight line in (c) indicates firing frequency r at which the first peak of the resonance occurs. The rest of parameters are as in the caption of Fig. 3.1.

Eq. (4.66) and the phase shift of the response approaches $-\pi/2$ as $\omega \to \infty$.

4.5.2 Noise amplitude oscillations

Similar to the mean input case, one can determine the first-order term of the expansion in $1/\omega$ of the model in response to high-frequency oscillations of the

noise intensity. Using Eq. (4.47), we obtain

$$\hat{P}(V,z,\omega) = -\frac{\hat{\sigma}}{i\omega\tau_m\kappa} z\partial_V P(V,z) + \frac{\hat{\sigma}}{\sigma}\partial_z(zP(V,z)) + O(\frac{1}{\omega^2}). \tag{4.67}$$

Therefore, combining Eqs. (4.17) and (4.67), we find

$$\hat{r}(\omega) \sim \frac{\sigma\hat{\sigma}}{i\omega\tau_m\Delta_T^2}\left[r_0 + \kappa^2 r_2\right], \tag{4.68}$$

resulting a phase shift of $-\pi/2$ at sufficiently large ω. This result is completely different from that of the simple LIF model where the high-frequency response is finite [148, 99]. Again, the $1/\omega$ asymptotic behavior of the EIF model holds for both white and coloured noise input [53].

In Fig. 4.3, the amplitude and phase of $\hat{r}(\omega)$ in response to σ oscillations are plotted. We show numerical solutions (solid lines) for low-frequency limit using Eqs. (4.55) and (4.62), the high frequency prediction (dashed lines) using Eq. (4.68), numerical simulations (symbols), and the corresponding numerical solutions for the white noise case (dotted lines). These results show that at high-noise levels, the response to an oscillation of σ is that of a band-pass filter [53]. The system responds best to intermediate frequency inputs, while both low- and high-frequency inputs are suppressed. Similar to the results in E oscillations, at low-input noise (lower panels), resonance occurs with the first peak at the steady-state firing rate r (straight line in panel (c)). As can be seen, coloured noise increases the amplitude of the linear response (left panels) at low-input frequency.

Further for low-noise level, the response to low-frequency inputs has a phase advance to that of inputs (panel (d)) which can be understood from the following argument [53]: at sufficiently low frequencies, the firing-rate response can be calculated directly from the $I-V$ curve of the neuron such that

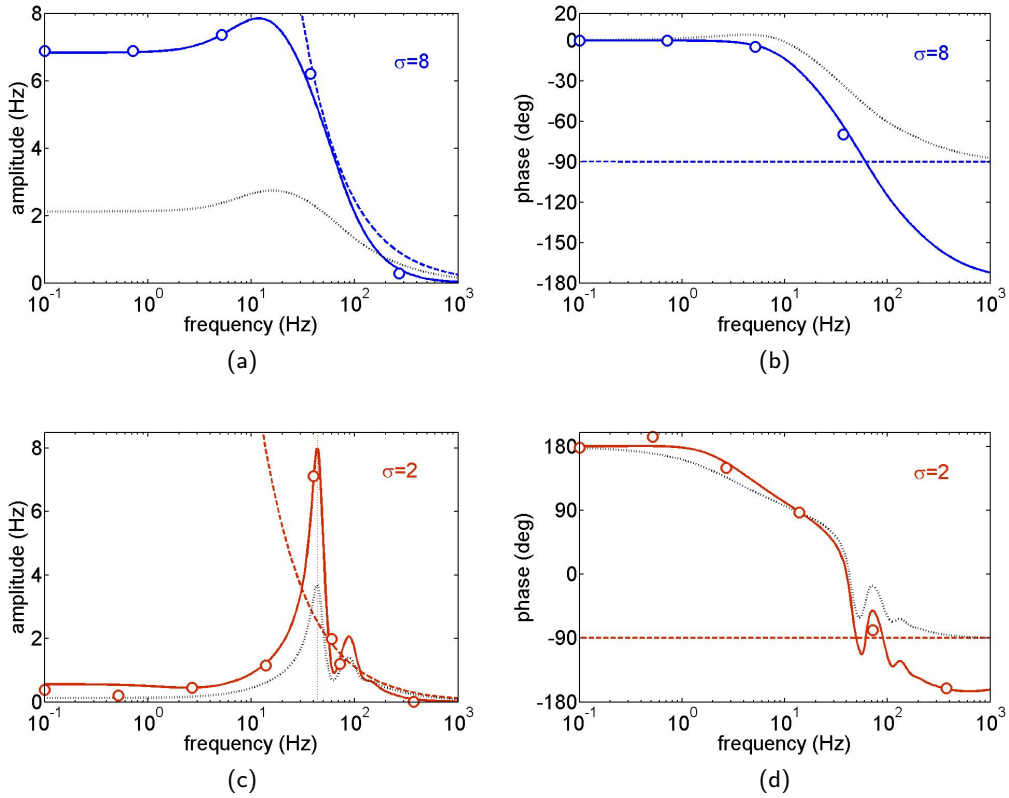

Figure 4.3: The amplitude and phase of the EIF response to oscillations in noise intensity σ in the presence of fast synaptic fluctuations with $\tau_s = 2$ ms. Solid lines are numerical results in low frequency using Eqs. (4.55) and (4.62), dashed lines indicate the high-frequency limit predicted by Eq. (4.68), and symbols represent simulation results. These results are compared with the corresponding white noise cases [135] (dotted lines). (a,b) Subthreshold high noise regime ($E = -60$ mV, $\sigma = 8$ mV, $\hat{\sigma} = \sqrt{18}$ mV, $r = 7.98$ Hz) and (c,d) suprathreshold low-noise regime ($E = -45$ mV, $\sigma = 2$ mV, $\hat{\sigma} = \sqrt{2}$ mV, $r = 43.93$ Hz), the straight line shows the resonance frequency which is equal to r. The rest of parameters are as in the caption of Fig. 3.1.

$$\hat{r}(\omega \to 0) = \hat{\sigma}\frac{\partial r}{\partial \sigma}. \tag{4.69}$$

It can be shown from Eqs. (3.27) and (3.38) that in suprathreshold regime and when the noise level is low, the firing rate $r = r_0 + \kappa^2 r_2$ decreases with σ resulting a phase lag equal π.

4.6 Comparison between the asymptotic response of mean input and noise-intensity oscillations

The high-frequency behavior in both cases of oscillations in E and σ are qualitatively similar, see Eqs. (4.66) and (4.68), they both decay to zero as $1/\omega$ at large ω. An important implication of the decay of the amplitude to zero is that the response to transient stimulus is not instantaneous as predicted for the LIF response to the mean input oscillations with coloured noise [17, 51]. This feature is expected [91] if one considers the impulse response function (inverse Fourier transform of the temporal-frequency response). When a brief current that delivers a total charge of order ϵ is injected into every neuron in the population, the voltage of every neuron jumps instantaneously by ΔV, where $\Delta V = \epsilon q/C$ with q the input charge. Thus, the voltage of any neuron within the interval $[V_{th} - \epsilon q/C, V_{th}]$ jumps instantaneously across the threshold. The total probability (fraction of neurons in the population) that crosses the threshold instantaneously is given by the corresponding area under the density curve. This area is of order ϵ^2 because of the absorbing boundary condition at V_{th}. Consequently, there is no first order (order ϵ) instantaneous component of the impulse response function. This implies that the frequency response does not converge to a constant, but rather decays to zero (see Figs. 4.3 and 4.2, left panels).

The high-frequency response to oscillatory σ has an additional factor of σ/Δ_T with respect to the response to oscillatory E. Hence, when $\Delta_T \ll \sigma$ (very sharp spike and/or large background noise fluctuations), the system is more susceptible to high-frequency σ oscillations than to the high-frequency E oscillations. The $\Delta_T \to 0$ limit is consistent with the results of the LIF neuron with σ oscilla-

tions [148, 99]. In the opposite situation $\sigma \ll \Delta_T$, the system is more susceptible to high-frequency oscillations in E rather than in σ. Intuitively, the dependence of the dynamics on Δ_T and σ can be understood from the following arguments: at small noise levels, the EIF model spends most of its time in the region close to the voltage threshold V_T around which the voltage dynamics is well approximated by the QIF model, which is more susceptible to rapid oscillations in E, see [53]. However, at high noise levels, the EIF membrane potential visits a large voltage range around V_T and is less sensitive to the dynamics close to threshold. Thus, at high noise levels, the model has a LIF-type behavior, i.e. it responds better to fast oscillations in σ than in E [53].

4.7 Discussion

We have used a combination of analytical and numerical methods to study the influence of filtered synaptic fluctuations on the dynamics of the firing rate of EIF neurons. The analytical methods consisted of a perturbative approach of the probability density which was used previously in [14, 17, 51, 52] and dynamical linear response theory [84, 58, 17]. These methods were used to derive the linear correction of the firing-rate response to both mean input and noise intensity oscillations. Then, the numerical threshold integration method was extended from white noise driven EIF neuron [135] to the coloured noise case to compute this correction. Compared to previous studies on dynamical response of other neuron models [17, 51, 52, 53, 124], our work allowed for fast computation of the linear response properties that would be hard to obtain by analytical methods and/or direct numerical simulations.

Here, we showed that the firing-rate response of the EIF neuron to oscillations in mean E and noise intensity σ have the following characteristic: in suprathreshold regimes, the response amplitude shows resonances at input frequencies which are integer multiple of the steady-state firing frequency. The response to high-frequency inputs does not have an instantaneous component and is independent of the noise level. It only depends on the properties of the spike-generating current, in contrast with the LIF neuron where the asymptotic response is dependent on the noise level and can have a finite value [99, 51, 148]. This finite transmission of high-frequency inputs in the LIF model, however, is known [52] to be more consequence of the oversimplification of the model rather than property of neurons.

The qualitative behavior of the linear response to oscillations in E and σ had the following differences: the response amplitude to σ oscillations is typically larger than the response amplitude to the E oscillations. At high-noise levels, the response to E oscillations becomes a low-pass filter while the response to σ oscillations is that of a band-pass filter. Further, the firing rate always lags behind E oscillations while at low frequencies, it usually shows a phase advance to σ oscillations. These results together with the asymptotic results given in this chapter hold in both white [52, 53, 135] and coloured [53] noise as well as for current-based or conductance-based fluctuations [52, 135].

The EIF model has received increasing interest in recent years. This is because of its realistic spike generating mechanism and having the same properties as many type I HH-type neurons when firing rate is low [52]. The dynamical properties of the EIF model with white noise (current-based and conductance-

based synaptic input) was studied in [135] and in a recent study the response of the model with slow voltage-activated transmembrane current was investigated in [137]. The EIF neuron was also used to study the response properties of recurrent networks [136] in the presence of white noise.

The methods used here (both numeric and analytic) can be extended to the analysis of the dynamics of recurrent neuronal networks in the presence of filtered noise. Naundorf et al., [124] used a novel sparse matrix representation of the Fokker-Planck equation to evaluate the dynamics of the θ-model to small time-varying inputs. It is worth using their method for the EIF neuron models. Finally, it would be interesting to include currents leading to subthreshold resonance [76, 138, 19] into the EIF model in order to capture the dynamics of many types of real neurons.

Chapter 5

The EIF model with fast inactivation

5.1 Intoduction

In neurons, voltage-gated sodium channels are primarily associated with spike generation at the axon initial segment and hence, with control of neuronal output [50]. The fraction of sodium channels available to respond to input depolarization is affected by fast and slow inactivation variables. These variables can cause variation in spike threshold, refractoriness and spike-frequency adaptation. The goal of this chapter is to study the impact of fast sodium inactivation on neuronal response properties.

Spike-frequency adaptation is a specialized feature of many types of neurons. It has been observed in neurons of various systems from several species, including vertebrates as well as invertebrates. In mammals, spike-frequency adaptation has been identified in peripheral, pyramidal and central neurons, see [10, 55] and references therein. Adaptation may have important role in information pro-

cessing of neurons and it can turn a neuron into a high-pass filter [10]. Other possible roles of adaptation include the phenomena of forward masking and selective attention [161].

Adaptation has been also studied in different neuron models. In LIF model with an adaptive ionic current [55], with a dynamics threshold [25] and with an adaptive threshold [101], in θ neuron [75], in the EIF model with additive adaptation variable [137], in conductance-based models with adaptation ionic currents [161, 10] and in type I neurons [46]. Most of these studies assume that the dynamics of adaptation variables are long compared to that of the voltage. Here, we consider a different situation in which fast inactivation of the sodium current influences spike generation of the neuron. Our concern is to study the significance of such fast adaptation in modulating input-output properties of the EIF neuron in the presence of filtered synaptic inputs.

Fast inactivation of the sodium current, represented by the h gating variable in the HH equations, is characterized by rapid offset upon depolarizing and rapid recovery following a brief hyperpolarizing interval [68]. We want to understand the effect of the h gating variable and its steady-state variable, h_∞ on the response of the EIF neuron, therefore we introduce two modified models of the EIF neuron referred to as the EIFh and EIFh$_\infty$. In the EIFh and EIFh$_\infty$ neurons, the spike generating current is scaled by the dynamics of the h variable and the steady-state variable h_∞ respectively. We examine the response of these models to constant and fluctuating synaptic inputs and study the neuronal signal transmission.

The chapter is organized as follows. We introduce the EIFh and EIFh$_\infty$ models in Sec. 5.2 and study their subthreshold dynamics in Sec. 5.3. The EIFh

and EIFh$_\infty$ neurons with a synaptic filtering are considered in Sec. 5.4 and their responses to constant and weak time-dependent inputs are obtained in Secs. 5.5 and 5.6 respectively. Here, we will make use of analytical and numerical methods developed in Chapters 3 and 4 along with numerical simulations to determine the steady-state and the dynamical response of neurons. The chapter ends with results given in Sec. 5.7 and a discussion in Sec. 5.8.

5.2 The EIFh and EIFh$_\infty$ model neurons

In Chapters 3 and 4, we studied the EIF model that originated from the conductance-based WB [160] model in which the sodium current responsible for action potential generation was modeled by an exponential term. In such a description, the sodium activation is assumed to be instantaneous and its inactivation variable, the h gating variable, is set to a constant (one). The h gating variable, however, has a voltage-dependent dynamics with fast kinetics which could potentially affect the spike-generation mechanism. Here, we introduce the EIFh neuron by including the dynamics of the HH-type inactivation variable h to the EIF neuron. The EIFh dynamics is governed by

$$\tau_m \frac{dV}{dt} = E - V + \Delta_T h \exp\left(\frac{V - V_T}{\Delta_T}\right) + W, \tag{5.1}$$

$$\tau_h \frac{dh}{dt} = h_\infty - h, \tag{5.2}$$

where V is the membrane potential with time constant τ_m, E is the resting potential, V_T is the threshold potential, Δ_T is the speed of action potential onset and W is the synaptic input current. The equation for the h variable is the well-known equation for voltage-gated variables in the HH equations. The dynamics of h is

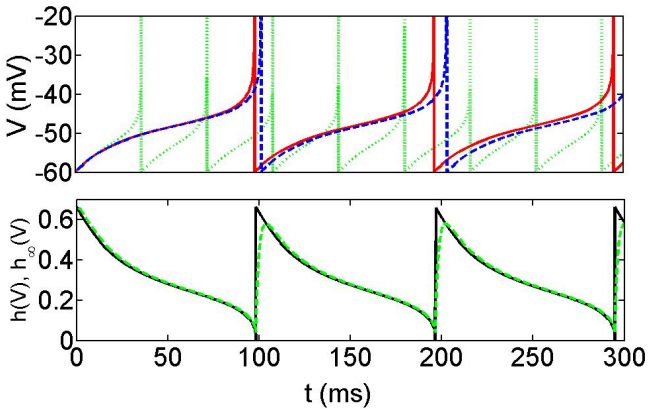

Figure 5.1: The dynamics of the EIFh and EIFh$_\infty$ for constant input $E = -50$ mV. Top panel: voltage trace of the EIFh (solid line), EIFh$_\infty$ (dashed line), and EIF with $h = 1$ (dotted line) neurons. Bottom panel: the inactivation gating-variable h (dashed) and its steady-state variable $h_\infty(V)$ (solid). Parameters are $\tau_m = 20$ ms, $\Delta_T = 3$ mV, $V_T = -53$ mV, $V_{th} = 0$ mV, and $V_{re} = -60$ mV.

a simple relaxation toward a voltage-dependent steady-state value $h_\infty(V)$ with a time constant $\tau_h(V)$ that depends on the membrane potential. h_∞ and τ_h are empirical functions defined in Appendix B.

The h gating variable operates on time scales of about $\tau_h \approx 2$ to 4 ms. If it is considered as instantaneous ($\tau_h \to 0$), the EIFh neuron is reduced to a one-dimensional differential equation defining the EIFh$_\infty$ neuron model

$$\tau_m \frac{dV}{dt} = E - V + \Delta_T h_\infty(V) \exp\left(\frac{V - V_T}{\Delta_T}\right) + W. \tag{5.3}$$

Both the EIFh and EIFh$_\infty$ models are supplemented with a threshold voltage, V_{th} above which firing occurs, followed by a reset to the reset potential, V_{re}.

In Fig. 5.1 (top panel), the voltage traces of the EIFh and EIFh$_\infty$ models are compared with the voltage trace of the EIF model. In the EIFh model, the rate of the membrane potential depolarization is suppressed by the h gating variable resulting slow action potential onset relative to the EIF and an increase in the

effective threshold potential. The behavior of the EIFh$_\infty$ neuron is similar to that of the EIFh neuron, but with even slower action potential onset which is the effect of instantaneous deactivation of $h_\infty(V)$ at threshold potential, see the bottom panel. The existence of the h and h_∞ variables modify the subthreshold behavior of the EIF neuron. The next section studies the subthreshold dynamics of the EIFh and EIFh$_\infty$ neurons.

5.3 Subthreshold dynamics

We first look at the subthreshold dynamics of the EIFh$_\infty$ neuron. The fixed points of the neuron are determined by the zeros of the function $f(V)$, where $f(V) = E - V + \Delta_T h_\infty(V) \exp\big((V - V_T)/\Delta_T\big)$. Similar to the EIF dynamics, in subthreshold regimes, the EIFh$_\infty$ neuron has a stable fixed point at $V \approx E$ and an unstable fixed point with $V > V_T$. Figure 5.2(a) shows the $I - V$ curve of the model compared with that of the EIF model. For membrane potentials above the stable fixed point, $f(V)$ is suppressed by $h_\infty(V)$ resulting an increase in the effective threshold potential and a slower onset of action potential.

For the EIFh neuron, we write nullclines of the system as

$$h_1 = \frac{V - E}{\Delta_T} \exp\left(\frac{-(V - V_T)}{\Delta_T}\right), \tag{5.4}$$

$$h_2 = h_\infty(V), \tag{5.5}$$

where h_2 is a sigmoidal function of the membrane potential with values between zero and one. In Fig. 5.2(b), h_1 and h_2 are plotted in the subthrehold regime where there exist two fixed points, a stable node ($\bullet$) and a saddle point ($\circ$). Upon increasing E, fixed points coalesce at the critical current and give rise to

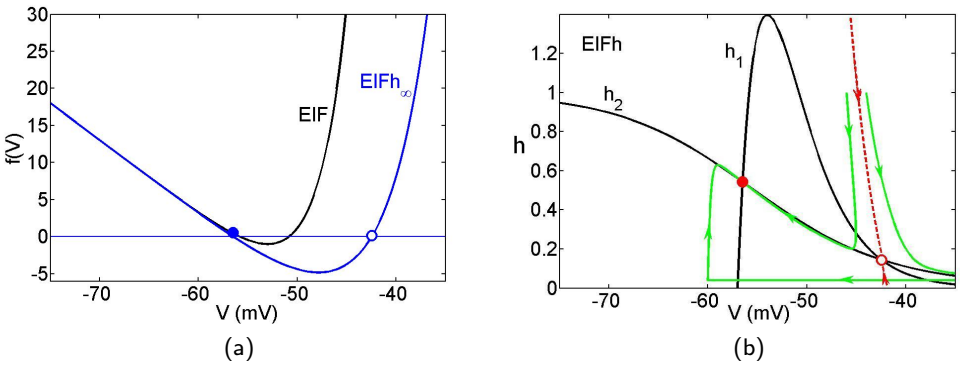

Figure 5.2: (a) $I-V$ curves of the EIF and EIFh$_\infty$ neurons and (b) the EIFh phase-plane. (a) The subthreshold dynamics of the EIFh$_\infty$ neuron has two fixed points, a stable and an unstable. At depolarized membrane potentials, the h_∞ variable increases the effective threshold potential leading to a shift in the unstable fixed point relative to that of the EIF neuron. (b) The phase-plane of the EIFh neuron in the subthreshold regime showing the nullclines $dV/dt = 0$ and $dh/dt = 0$, two sample trajectories (green lines), and the stable manifold of the saddle point (red line). In both panels, ($\bullet$) represents a stable point and ($\circ$) shows an unstable point. $E = -57$ mV and the rest of parameters are as in Fig. 5.1.

a saddle-node bifurcation. Increasing E further causes both to disappear and the neuron begins repetitive firing (suprathreshold regime). The intersection of the nullclines (5.4) and (5.5) gives the following equation from which fixed points can be determined

$$E - V^* + \Delta_T h_\infty(V^*) \exp\left(\frac{V^* - V_T}{\Delta_T}\right) = 0. \tag{5.6}$$

It should be noted that solutions of Eq. (5.6) also correspond to fixed points of the EIFh$_\infty$ model. Therefore, the fixed points of both models occur at identical membrane voltages, resulting in identical critical currents above which repetitive firing occurs.

The stability type of fixed points of the EIFh model can be found by studying

the linearized system. We write the Jacobian matrix as

$$\begin{pmatrix} -1/\tau_m + (h_\infty/\tau_m)\exp\big((V-V_T)/\Delta_T\big) & (\Delta_T/\tau_m)\exp\big((V-V_T)/\Delta_T\big) \\ h'_\infty(V)/\tau_h & -1/\tau_h \end{pmatrix}, \tag{5.7}$$

with trace $T = -(1/\tau_h + 1/\tau_m) + (h_\infty/\tau_m)\exp\big((V-V_T)/\Delta_T\big)$ and determinant

$$D = \frac{1}{\tau_h\tau_m}\Big(1 - \exp\big((V-V_T)/\Delta_T\big)\Big)\big(h_\infty(V) + \Delta_T h'_\infty(V)\big). \tag{5.8}$$

It is easy to see that $\tau_h D = -f'(V)$. At the fixed point with $V \approx E$, the derivative of the $I-V$ curve of the EIFh$_\infty$ is negative, resulting $D > 0$, and also we have $T \approx -(1/\tau_h + 1/\tau_m)$, therefore the fixed point is stable (resting point). For the second fixed point, the $I-V$ curve has a positive slope, therefore $D < 0$, resulting a saddle point. Figure 5.2(b) shows the EIFh phase-plane in the subthreshold regime. Any perturbation from the resting state that is not large enough to cross the stable manifold of the saddle point eventually dies away, but perturbations that cross the stable manifold result in an action potential followed by a reset to V_{re} and then converging to the resting state.

It is known that the shape of the frequency-input ($f-I$) curve is an important factor in the neuronal signal transmission [10, 52]. The derivative of the $f-I$ curve determines the amplitude of the response at sufficiently low frequencies. We represent in Fig. 5.3(a) the $f-I$ curve of the EIFh (red line) and EIFh$_\infty$ (blue line) neurons for constant input currents. As can be seen, input currents below the threshold current, I_c are not transmitted at all. The firing rate for inputs near I_c scales as $\sqrt{I-I_c}$ which is an essential property of type I neurons. The $f-I$ curve of both models matches well near the onset of the firing and their difference at higher firing frequencies is not significant.

Under in *vivo* conditions, where spontaneous activity of presynaptic neurons causes strong background fluctuations in the membrane potential, constant inputs represent unrealistic inputs to a neuron. Therefore, in the next section, we explore the behavior of this adapting neuron in response to synaptic fluctuating inputs.

5.4 The EIFh and EIFh$_\infty$ neurons with synaptic filtering

A realistic model of synaptic input is usually described by filtered white noise (see Chapter 1). Therefore, we consider the EIFh model subject to the synaptic input W satisfies Eqs. (5.1) and (5.2) in which W obeys

$$\tau_s \frac{dW}{dt} = -W + \sigma\sqrt{2\tau_m}\xi(t), \tag{5.9}$$

where τ_s is the synaptic time constant and ξ is the Gaussian white noise with zero mean and autocorrelation $\langle \xi(t)\xi(s)\rangle = \delta(t-s)$. Similarly, the EIFh$_\infty$ with filtered synaptic input satisfies Eqs. (5.3) and (5.9).

Recalling from Chapters 3 and 4, the firing-rate response of the EIF neuron with synaptic filtering was obtained in the framework of the Fokker-Planck operator and by using both analytical and numerical methods. In the steady-state case, a perturbative expansion of the Fokker-Planck equation as well as the effective threshold integration method allowed us to determine the firing rate in two limits of fast ($\tau_s \ll \tau_m$) and slow ($\tau_s \gg \tau_m$) synaptic inputs. Similarly, we determined the dynamical response of the neuron for fast synaptic inputs. Here, we can follow an identical approach to calculate the steady-state and firing-rate response of the EIFh$_\infty$ neuron. The Fokker-Planck equation of the EIFh neuron, however, is a three-dimensional nonlinear differential equation which is difficult to solve

analytically. We can only use these methods to obtain the response in long τ_s limits. In short τ_s limits, the existence of two fast variables, h and W, complicates the calculations and it is not possible to proceed analytically. Instead, we constrain ourselves to numerical simulations.

5.4.1 The Fokker-Planck equation

This section contains a review of methods which will be used for the steady-state response and the response to oscillatory inputs of the EIFh$_\infty$ neuron. We consider the EIFh$_\infty$ neuron receiving small amplitude oscillatory currents in the presence of synaptic fluctuations. Following the methods given in Chapters 3 and 4, we apply the changing variable $z = (\kappa/\sigma)W$ with $\kappa = \sqrt{\tau_s/\tau_m}$ on Eqs. (5.3) and (5.9). The dynamics Fokker-Planck equation of the resulting system reads

$$\kappa^2\tau_m\partial_t\mathcal{P}(V,z,t) = -\kappa^2\partial_V\big[(f+\frac{\sigma}{\kappa}z)\mathcal{P}\big] + \mathcal{L}\mathcal{P} + \kappa^2\tau_m\nu(z,t)\delta(V-V_{re}), \quad (5.10)$$

where $\mathcal{P}$ is the probability density with $\mathcal{L}\mathcal{P} = \partial_z^2\mathcal{P} + \partial_z(z\mathcal{P})$ and $\nu(z,t)$ is the rate density. $\nu(z,t)$ is defined by

$$\nu(z,t) = \lim_{V\to\infty}\Delta_T h_\infty(V)\exp\big((V-V_T)/\Delta_T\big)\mathcal{P}(V,z,t). \quad (5.11)$$

Any solution to Eq. (5.10) should satisfies boundary conditions given in Eq. (4.8). From linear response theory [84, 58, 17], the steady-state and dynamics components of the probability density and rate density satisfy Eqs. (4.10) and (4.13) respectively. The steady-state and dynamics parts of the rate density are obtained by solving the corresponding parts of the Fokker-Planck equation. As described in Chapters 3, the techniques to solve the steady-state Fokker-Planck equation in the fast synaptic limit are based on the perturbative expansion of the steady-state

probability density and rate density in powers of κ and finding the corresponding corrections at successive orders. Threshold integration method is then used to compute these corrections numerically. For slow synaptic inputs, using the fact that synaptic fluctuations can be considered as a constant input within a time period of τ_m, we can find the firing rate of the neuron using Eq. (3.62). Similar techniques are used to solve the dynamics Fokker-Planck equation for fast synaptic inputs and to find the linear correction to the firing rate dynamics, see Chapter 4.

The related calculations for the EIFh$_\infty$ neuron will be identical with those given for the EIF neuron, therefore we do not repeat them here unless there is a difference. We first determine the steady-state response.

5.5 Steady-state firing rate

The time-independent solution of the Fokker-Planck equation (5.10) can be calculated in two limits: fast and slow synaptic currents.

For fast-synaptic inputs, the steady-state firing rate of the EIFh$_\infty$ neuron is approximated by $r = r_0 + \kappa^2 r_2$ where r_0 is given by Eq. (3.27) and r_2 satisfies the following equation which is a modified version of Eq. (3.38)

$$\begin{aligned} r_2 = &- r_0 \int_{-\infty}^{\infty}\int_{V}^{\infty} \Big[\frac{3}{2}\partial_u^2 f(u)Q_0(u) + 2\partial_u f(u)\partial_u Q_0(u)\Big] \exp\big(\psi(u,V)\big)\,\mathrm{d}u\mathrm{d}V \\ &+ r_0^2\tau_m\Big[\frac{1}{\Delta_T} - \frac{1}{\Delta_h} + \frac{3}{2}\frac{f(V_{re})}{\sigma^2}\Big]\int_{-\infty}^{V_{re}} \exp\big(\psi(V_{re},V)\big)\,\mathrm{d}V - \frac{3}{2}r_0^2\tau_m. \end{aligned} \tag{5.12}$$

In the derivation of Eq. (5.12), we have used the fact that in the large V limit, $f(V) \sim h_\infty(V)\exp((V-V_T)/\Delta_T)$ and therefore

$$\lim_{V\to\infty}\frac{f'(V)}{f(V)} = \frac{1}{\Delta_T} + \lim_{V\to\infty}\frac{h'_\infty(V)}{h_\infty(V)} \sim [\frac{1}{\Delta_T} - \frac{1}{\Delta_h}], \quad \Delta_h > \Delta_T.$$

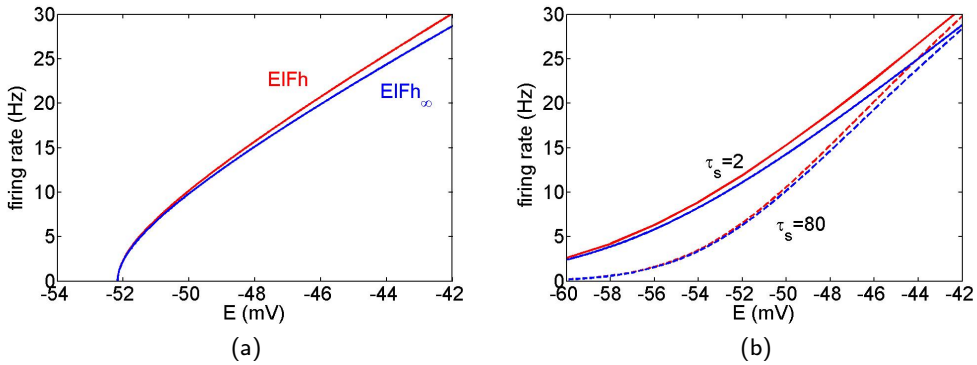

Figure 5.3: $f-I$ curves of the EIFh and EIFh$_\infty$ neurons for constant (a) and noisy input currents (b). (a) For constant inputs, $f-I$ curves of the EIFh (solid red) and EIFh$_\infty$ (solid blue) show good agreement near the onset of firing. (b) For synaptic noise inputs with $\sigma = 8$ mV, the steady-state firing rate is plotted in two limits of $\tau_s = 2$ (solid) and 80 ms (dashed). In both limits, the response of the EIFh (red) matches well with that of the EIFh$_\infty$ (blue) neuron at low firing rates. Other parameters are as in the caption of Fig. 5.1.

Figure 5.3(b) shows the steady-state firing rate of the EIFh and EIFh$_\infty$ models with synaptic time constants $\tau_s = 2$ and 80 ms. In subthreshold regimes, the difference between the firing rate of models in both limits is not significant, while for larger E, the EIFh neuron gives slightly higher firing rate. As expected, the response of neurons to short-synaptic currents is larger than the response to long-synaptic currents. For $\tau_s = 2$ ms, the calculation of the EIFh$_\infty$ is done using threshold integration methods (see Appendix A) and the response of the EIFh neuron is obtained by numerical simulations. For slow-synaptic inputs, the response of both neurons are calculated using an equation equivalent to Eq. (3.62).

5.6 The frequency response

In this section, we examine the signal transmission of the EIFh and EIFh$_\infty$ neurons. As for Chapter 4, we consider a weak time-dependent perturbation of parameters

E and σ satisfying Eqs. (4.3) and (4.4) and find the response of neurons in two limits of low- and high-frequency inputs.

5.6.1 Low-frequency inputs

We follow the calculations presented in Chapter 4 to find the linear correction to the dynamics response of the EIFh$_\infty$ neuron. The response in low frequencies is approximated by $\hat{r}(\omega) = \hat{r}_0(\omega) + \kappa^2 \hat{r}_2(\omega)$. For the case of E oscillations, the pair of $\hat{r}_0$ and $\hat{r}_2$ are predicted by Eqs. (4.30) and (4.43) and for σ oscillations, they are given by Eqs. (4.55) and (4.62).

It should be noted that since in the large V limit, the function $f(V)$ is scaled by $h_\infty(V)$, our calculations will be slightly different from those given in Chapter 4. In particular Eqs. (4.39) and (4.60), which were used to derive $\hat{r}_2(\omega)$ respectively in the cases of E and σ oscillations, will change to

$$\begin{aligned}\hat{\mathcal{E}}_2(V,\omega) = &-\frac{3}{2} f \partial_V^2 \hat{Q}_0 - \partial_V f \partial_V \hat{Q}_0 + \frac{3}{2}\sigma^2 \partial_V^3 \hat{Q}_0 - i\omega\tau_m \partial_V \hat{Q}_0 \\ &- \hat{r}_0 \tau_m \left(\frac{1}{\Delta_T} - \frac{1}{\Delta_h}\right)\delta(V - V_{re}),\end{aligned} \tag{5.13}$$

$$\begin{aligned}\mathcal{E}_2(V,\omega) = \frac{\hat{\sigma}}{\sigma}\Big[&-3 f \partial_V^2 Q_0 - 2\partial_V f \partial_V Q_0 + 6\sigma^2 \partial_V^3 Q_0 + \frac{\tau_m}{2\sigma^2} i\omega f Q_0 \\ &+ 2\partial_V Q_2 - \frac{7}{2} i\omega\tau_m \partial_V Q_0 - 2 r_0 \tau_m \left(\frac{1}{\Delta_T} - \frac{1}{\Delta_h}\right)\delta(V - V_{re})\Big].\end{aligned} \tag{5.14}$$

Similar to the steady-state case, we use numerical simulations to determine the response of the EIFh neuron to both mean and noise-intensity oscillations.

5.6.2 High-frequency inputs

For the EIFh$_\infty$ neuron, the high-frequency decay of $\hat{r}(\omega)$ in both cases of E and σ oscillations can be calculated analytically.

Mean input oscillations

From Eqs. (4.63)-(4.65), the high-frequency response of the EIFh$_\infty$ satisfies

$$\begin{aligned}\hat{r}(\omega) &= \frac{1}{\tau_m}\lim_{V\to\infty} f(V)\int \hat{P}(V,z,\omega)\mathrm{d}z \\ &\sim \frac{r\hat{E}}{i\omega\tau_m}\lim_{V\to\infty}\frac{f'(V)}{f(V)},\end{aligned} \tag{5.15}$$

where we have use

$$\hat{P}(V,z,\omega) \sim \frac{-\hat{E}}{i\omega\tau_m}\partial_V P(V,z). \tag{5.16}$$

In large V limit,

$$f(V) \sim h_\infty(V)\exp((V-V_T)/\Delta_T), \tag{5.17}$$

therefore, we conclude

$$\hat{r}(\omega) \sim \frac{r\hat{E}}{i\omega\tau_m}\Big(\frac{1}{\Delta_T}-\frac{1}{\Delta_h}\Big). \tag{5.18}$$

This indicates that the amplitude of the frequency response decays as $1/\omega$ at large ω and the phase shift of the response approaches $-\pi/2$ as $\omega\to\infty$.

Noise intensity oscillations

Using Eqs. (4.67) and (5.17), the high-frequency response to noise-intensity oscillations is given by

$$\hat{r}(\omega) \sim \frac{r_0\sigma\hat{\sigma}}{i\omega\tau_m}\Big(\frac{1}{\Delta_T}-\frac{1}{\Delta_h}\Big)^2, \tag{5.19}$$

resulting a $1/\omega$ asymptotic behavior and a phase shift of $-\pi/2$ at sufficiently large ω.

The above results show that in both cases of oscillations in the mean input and noise intensity, the behavior of the high-frequency response of the EIFh$_\infty$ is independent of the noise level, rather it depends on the properties of the sodium

current responsible for spike generation. The $1/\omega$ decay of the response with the phase shift approaching $-\pi/2$ at large ω are similar to the EIF neuron. However, comparing Eqs. (5.18) and (5.19) respectively with the response of the EIF model to high-frequency oscillations in mean input, Eq.(4.66), and noise intensity, Eq.(4.68), we find that the high-frequency response of the EIFh$_\infty$ decays faster than that of the EIF neuron.

5.7 Results

Figure 5.4 shows the amplitude and phase of the frequency response of the EIFh and EIFh$_\infty$ neurons to oscillations in input E. These results are compared with the corresponding ones in the EIF neuron. As can be seen, the response of the EIFh and EIFh$_\infty$ at high-noise levels becomes a low-pass filter and the firing rate always lags behind input oscillations. These are also the case in the EIF neuron. Further, the low-frequency attenuation of the response of the EIFh neuron is in good agreement with that of the EIFh$_\infty$ neuron, while the amplitude of its high-frequency response is similar to that of the EIF neuron which is the result of the history-dependent inactivation h.

In Fig. 5.5, a comparison of the filters of the EIFh-h$_\infty$ and EIF models in response to noise-intensity oscillations is shown. For the EIFh$_\infty$ and EIF neurons, we plot $\hat{r}(\omega) = \hat{r}_0(\omega) + \kappa^2 \hat{r}_2(\omega)$ (solid lines) using Eqs. (4.55) and (4.62) and the high-frequency prediction using, respectively, Eqs. (5.19) and (4.68). Further, we perform numerical simulations for the EIFh (◯), EIFh$_\infty$ (△) and EIF (□) neurons.

In both cases of the response to E and σ oscillations, the h and h_∞ variables have significant effects on the response at low-input frequencies. However, the

amplitude of the response at high frequencies decreases again as $1/\omega$ as for the EIF model. The h_∞ variable causes an overall reduction of the gain at high frequencies. This effect is in agreement with analytical calculations (Eqs. (5.19) and (5.18)), which predict that in the limit $\omega \to \infty$, the firing-rate response decreases as $(1/\Delta_T - 1/\Delta_h)$ for changes in E and as $(1/\Delta_T - 1/\Delta_h)^2$ for changes in σ. The h gating variable, however, attenuates the response slightly less for frequencies beyond several hundred Hertz and gives the amplitude similar to the EIF response. Similar to the EIF neuron, at low noise levels (right panels), the response to an oscillation of either E or σ displays resonances at frequencies multiple of the steady-state firing rate r.

5.8 Discussion

We studied the effect of fast inactivation of the sodium current on neuronal response properties using the EIFh and EIFh$_\infty$ neuron models. The response of these inactivating neurons to both constant and fluctuating synaptic inputs was examined. We showed that the response of neurons to constant inputs matches well near the critical current and for larger inputs, the EIFh neuron gives slightly larger firing rate. The response of both neurons near the critical current, I_c scales as $\sqrt{I - I_c}$ which was also the case for the EIF neuron. The response of the EIFh and EIFh$_\infty$ to synaptic fluctuations was given in two opposite limits of short and long synaptic inputs. In both limits, their responses agree for low firing frequencies and the discrepancy between responses increases with the firing frequency.

The effect of inactivation variables on information processing of neurons was also studied using both analytical and numerical techniques which were previously

used in Chapters 3 and 4. We computed the response of neurons to oscillations in mean input E and noise intensity σ in the presence of fast synaptic filtering and found the following results: inactivation variables have significant effects on the response at low frequencies. At high frequencies, the gain of the response decreases again as $1/\omega$ as in the EIF model. A comparison between the high-frequency response of the EIFh$_\infty$ neuron given in Eqs. (5.18) and (5.19) with the corresponding ones in the EIF neuron, Eqs. (4.66) and (4.68), reveals that the gain of the EIFh$_\infty$ has an overall reduction. This reduction is given by $(1/\Delta_T - 1/\Delta_h)$ for E oscillations and $(1/\Delta_T - 1/\Delta_h)^2$ for σ oscillations. Further, the low-frequency attenuation of the response of the EIFh neuron is similar to that of the EIFh$_\infty$ neuron, while the high-frequency attenuation is suppressed and is more similar to that of the EIF neuron. For both the EIFh and EIFh$_\infty$ models, high-frequency oscillations in E and σ produce negative phase shift of the response such that the response phase is always delayed to that of inputs. In the suprathreshold regime and for weak background fluctuations, low-frequency oscillations of σ produce a positive phase shift such that between low and high frequencies, there is a frequency in which no phase shift occurs. The existence of this property is due to the negative effect of noise on higher firing rates and is different from the one observed in adapting neurons [55, 137] which was the consequence of the negative effect of slow adapting variables.

Unlike other studies of spike-frequency adaptation [55, 10, 137] in which adaptation variables are additive in the membrane equation and have time scales slower than the voltage dynamics, we considered a fast adaptation (inactivation) variable which directly scales the sodium current responsible for spike generation.

This would be important as it is known that the response of a neuron to high-frequency inputs depends only on the properties of the current leading to spike generation, see [52] and discussion in Chapter 4. Here, the sodium current responsible for spike generation is suppressed by the h variable, therefore one would expect to find qualitatively different asymptotic behavior. It is known [125, 53] that all NLIF family models (including The EIFh$_\infty$ model) with spike emission defined at $V \to \infty$ and resetting occurring thereafter show a $1/\omega$ decay at high frequencies. This is because the probability flux at large V has a nonvanishing first order term in large ω expansion (see Eq. (5.16) for the case of the EIFh$_\infty$ model). Our analytical calculations (Eqs. (5.18) and (5.19)) are in agreement with this prediction. Our numerical simulations for the EIFh filter also show the $1/\omega$ decay at high frequencies and we do not see any significant difference between the gain of the EIFh and EIF filters in this asymptotic regime. The effect of the history-dependent inactivation h on high-frequency filtering becomes rather obvious by comparing it with the h_∞ inactivation. The h inactivation increases the susceptibility of the neuronal response to high-frequency inputs relative to the h_∞ inactivation. Further, in experimental studies [50] a slowly developing and much longer lasting suppression of the sodium current is observed when neuron is subjected to prolonged periods of depolarization. This suggests that considering such a mechanism would have different functional impacts on the EIF neuronal responses. It is of great interest to modify the EIF (or EIFh and EIFh$_\infty$) model to include the dynamics of the slow sodium inactivation and study filtering properties of this model subject to filtered synaptic fluctuations. This would considerably increase our understanding of the response properties of neurons in particular in

the region of action-potential generation. It is also known that neurons with slow adaptation variables determine a preferred input frequency at which the response shows a zero phase shift relative to the input oscillations. This frequency is a crucial factor in setting the frequency of oscillations of a population for which synchronization could occur [157]. Therefore, once the response of the EIF neuron with a slow inactivation of the sodium current is known, it can be used to predict the stability of synchronization in neuronal network. Finally, the stability of asynchronous firing in large networks of interacting neurons has been studied in LIF [15, 16] and QIF [63, 64] neuronal networks. It is worth studying this for neurons with more realistic dynamics such as the EIFh and EIFh$_\infty$ neurons.

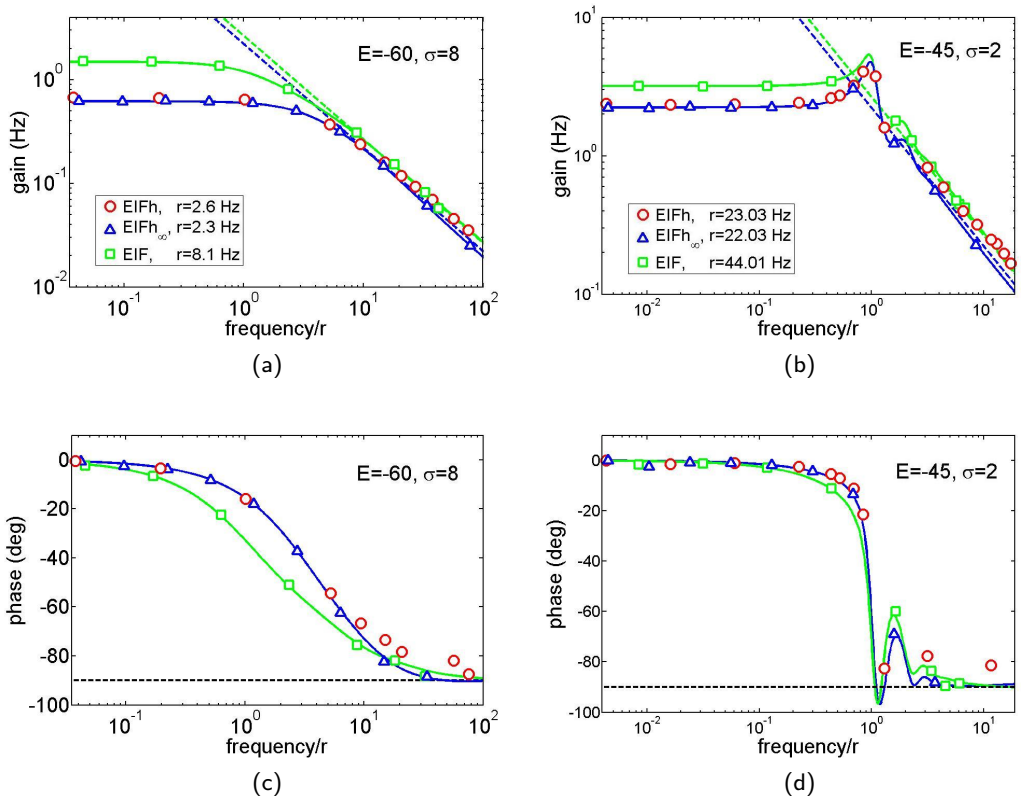

Figure 5.4: Effect of the sodium current inactivation on filtering properties of the EIF neuron in response to oscillations in input E. We plot the gain and phase shift of the firing-rate response of the EIFh, EIFh$_\infty$ and EIF neurons with fast synaptic input $\tau_s = 2$ ms in two regimes: (a,c) subthreshold low-noise regime ($E = -60$ mV, $\hat{E} = 1$ mV, $\sigma = 8$ mV) and (b,d) suprathreshold high-noise regime ($E = -45$ mV, $\hat{E} = 1$ mV, $\sigma = 2$ mV). Solid lines are numerical results for the EIFh$_\infty$ (blue) and EIF (green) models plotted using Eqs. (4.30) and (4.43), dashed lines are their high-frequency asymptotic results predicted, respectively, by Eqs. (5.18) and (4.66), and symbols represent numerical simulations of the EIFh, EIFh$_\infty$ and EIF models. For these models, the gain of the filter decays as $1/\omega$ in large ω limits, with an overall reduction for the EIFh$_\infty$ neuron. The h and h_∞ variables do not modify the high-frequency filtering properties. However, they shape the firing-rate dynamics at low frequencies. Note that for each plot, the frequency is normalized to the average firing rate of the corresponding model. Other parameters are as in the caption of Fig.5.1.

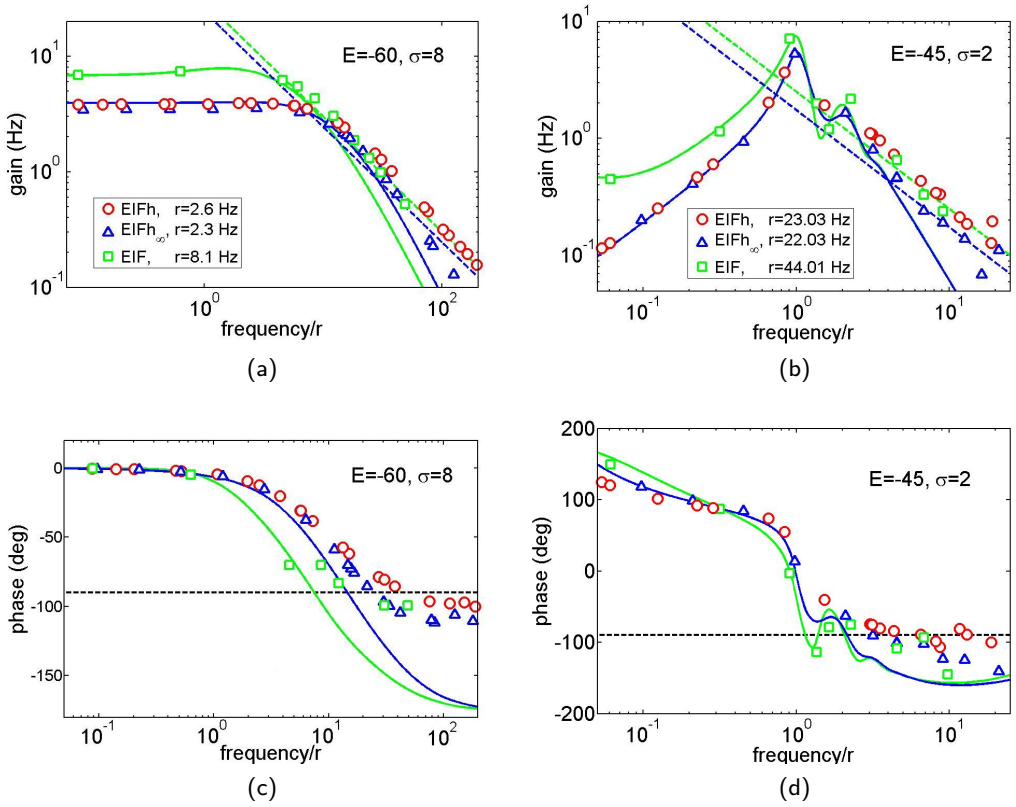

Figure 5.5: Amplitude and phase of the firing-rate response to noise-intensity oscillations for the EIFh and EIFh$_\infty$ neurons with fast synaptic filter, $\tau_s = 2$ ms. (a,c) High-noise subthreshold regime ($E = -60$ mV, $\sigma = 8$ mV, $\hat{\sigma} = \sqrt{18}$ mV) and (c,d) low-noise suprathreshold regime ($E = -45$ mV, $\sigma = 2$ mV, $\hat{\sigma} = \sqrt{2}$ mV). For the EIFh$_\infty$, we plot $\hat{r}(\omega)$ (solid lines) using Eqs. (4.55) and (4.62), the high-frequency prediction (dashed lines) using Eq. (5.19), and numerical simulations ($\triangle$). The results for the EIFh neuron are presented by numerical simulations ($\bigcirc$) over the full range of input frequencies. The corresponding analytical results and numerical simulations ($\square$) for the EIF neuron are also plotted for comparison. Other parameters are as in the caption of Fig.5.1.

Chapter 6

Mode locking in the EIF model

In this chapter, we look at two cases of deterministic and stochastic mode locking of the EIF neuron model. First we consider periodically driven EIF neuron and use numerical simulations to represent Arnol'd tongues structure. Then we add a stochastic input to the model and see its effect on the locking solutions.

6.1 Arnol'd tongues of the EIF model

In this section, we consider the periodically driven EIF neuron model and plots its Arnol'd tongues structure. The EIF model satisfies Eqs. (1.21) and (1.23). It proves convenient to write the model in dimensionless units by expressing time in units of τ_m and by rescaling the voltage $\bar{V} = (V - V_T)/\Delta_T$. This gives

$$\frac{d\bar{V}}{dt} = \bar{E} - \bar{V} + \exp(\bar{V}) + I_{app}(t), \tag{6.1}$$

where $\bar{E} = (E - V_T)/\Delta_T$ and I_{app} is a periodic input. Here, we use sinusoidal forcing $I_{app}(t) = I_0 + \epsilon \sin(2\pi\omega t)$, where I_0 is a constant current and ϵ is the amplitude of the forcing with frequency ω. Equation (6.1) is supplemented with a threshold and reset potential represented by $\bar{V}_{th}$ and $\bar{V}_{re}$, respectively. A spike is

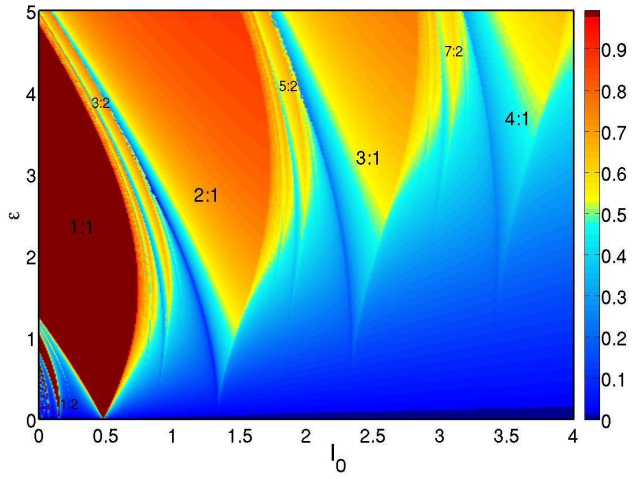

Figure 6.1: Arnol'd tongue structure of the EIF model (6.1) as a function of I_0 and ϵ. We plot the vector strength $r = \langle \exp(2\pi i \phi_n) \rangle$, computed over 4000 spike phases ϕ_n on a mesh of size 500×500. Parameters are $\bar{E} = -1$, $\bar{V}_{th} = 18$, $\bar{V}_{re} = -2.5$, and $\omega = 0.2$.

registered when the voltage reaches the threshold $\bar{V}_{th}$ after which it is immediately reset to $\bar{V}_{re}$.

Similar to the RF model, the Arno'ld tongues structure of the EIF model can be found. To find stability regions of mode-locked solutions, we constrain ourselves to numerical simulations and use *vector strength* as in [92] as a measure of synchronisation between periodic input and firing times. It is defined by $r = \langle \exp(2\pi i \phi_n) \rangle$, where $0 \leq \phi_n < 1$ is the phase of the nth firing time and $\langle . \rangle$ denotes the average over all occurring firing phases. r can take values between zero and one, where $r = 1$ shows all spikes occur at one specific phase. Therefore, it should be noted that for a $p : q$ mode-locking pattern with $p, q \neq 1$, although spikes repeat for each q cycles of the input at exactly p phases $(\phi_0, \ldots, \phi_{p-1})$, the vector strength is not one. The result, Fig. 6.1, displays Arno'ld tongues in the (ϵ, I_0)-parameter plane. All the $p : q$ firing patterns, with $p, q > 1$, are found over smaller regions of the parameters space compared to the p:1 patterns. Some

examples of $p:q$ locking solutions are indicated in the plot. As expected, between a $p:q$ and $p':q'$ locking solution, there exists the $p+p':q+q'$ locking solution, e.g., between 1:1 and 2:1, the 3:2 tongue, between 2:1 and 3:1, the 5:2 tongue, and between 3:1 and 4:1, the 7:2 tongue can be seen. When constant input, I_0 increases, one can go from the $p:q$ tongues with $p<q$, e.g., the 1:2 tongue, to the 1:1 tongue and then to the $p:q$ tongue with $p>q$.

6.2 Stochastic mode locking

Effect of stochastic input on neuronal response is another important topic of research. Stochastic forcing turns a quiescent excitable system into a stochastic oscillator and in suprathreshold regimes, turns the deterministic oscillator into a noise-perturbed oscillator [91]. Noise also smooths the input-output curve and can significantly alter $p:q$ deterministic mode-locking structures [109, 60, 153, 106, 107, 151, 104]. Recently, stochastic mode locking has been studied in ventral cochlear nucleus chopper and onset neurons [92]. In stochastic mode locking, firing are caused by the combination of noise and periodic forcing. While noise randomly creates firing in the subthreshold regime, it can also destroy firing that are otherwise mode locked to a periodic input in the suprathreshold regime. It can cause *skipping* which is a mode-locked solution with firing phase jitter and a random integer number of input periods are skipped between firing [107]. Skipping has been observed in mechanoreceptors [42], the hair cells of the auditory system, receptors of the electrosensory systems, and in the primary visual cortices [108]. The presence of the noise significantly alter the firing pattern of any periodically driven cell [106]. For a periodically driven pacemaker, noise can make the

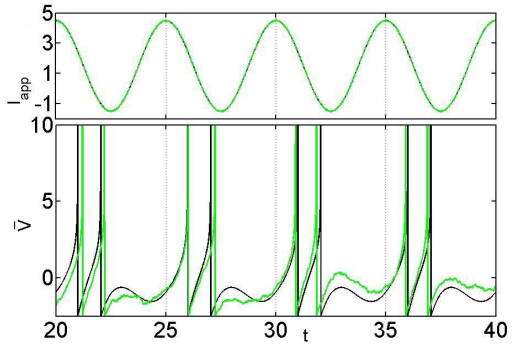

Figure 6.2: Effect of noise on a 2:1 mode-locked solution arising in a sinusoidally driven EIF model (6.1). The membrane voltage trajectory (bottom panel) in the non-noisy case (black line) shows two spikes with phases ϕ_0 and ϕ_2 for every one cycle of $I_{app}(t) = 1.5 + 3\sin(2\pi\omega t)$, $\omega = 0.2$. Adding noise, $\sigma = 0.05$, alters the voltage trajectory (green line) and the firing phases are varied stochastically. Other parameters are as in the caption of Fig. 6.1.

firing pattern irregular and blur the transition between different mode-locked behaviors as parameters are varied [60]. In this section, we introduce the stochastic mode-locking and gives examples from the periodically driven noisy EIF model.

We consider the periodically driven EIF model with additive noise satisfying Eq. (6.1) with $I_{app}(t) = I_0 + \epsilon\sin(2\pi\omega t) + \sqrt{2\sigma}\xi(t)$, where $\xi(t)$ is a Gaussian white noise with zero mean and autocorrelation $\langle\xi(t)\xi(s)\rangle = \delta(t-s)$ and σ denotes the intensity of the noise. The response properties of the system can be studied by describing the firing times statistics.

As explained in Sec. 2.7, for deterministic system, a $p : q$ mode-locked solution is defined by the p firing phases, $\Phi = (\phi_0, \ldots, \phi_{p-1})$ within q periods of the periodic input, e.g., in Fig. 6.2 the voltage trajectory of the non-noisy EIF model ($\sigma = 0$) in response to $I_{app} = 1.5 + 3\sin(2\pi\omega t)$ with $\omega = 0.2$ shows a 2:1 mode-locking pattern (bottom panel, black line). That means two spikes within each cycle of the input (top panel, black line). In the presence of noise

(green lines) with $\sigma = 0.05$, the firings still seems to fall into synchronization with the driving period even though the firing phases are varied stochastically and the firing rate slightly differ from deterministic case. This phenomenon is referred to as stochastic mode-locking [152, 109, 153, 107]. It is important to note that in the presence of noise, the firing patterns are not strictly periodic, even though the spikes tend to occur over a small range of phases, see Fig. 6.3 (a). Therefore, the firing rate per cycle of the input would be defined as the average rate rather than p/q.

Therefore in the presence of noise, the firing times are random variables and instead of a set of finite firing phases for mode-locked solutions, we deal with the probability distribution of the firing phases. For this, the stochastic trajectory $\bar{V}(t)$ is analyzed. Assuming $\bar{V}(t)$ with initial condition $\bar{V}(0) = \bar{V}_0$, the time it takes to reach the threshold potential for the first time is a random variable defined by

$$T_{\theta_0} = \inf\left\{t | \bar{V}(t) \geq \bar{V}_{th}, \bar{V}(0) = \bar{V}_0\right\}, \tag{6.2}$$

where θ_0 is the initial phase of the periodic input. The random variable T_{θ_0} represents the first-passage-time (FPT) [134] which has a probability density function $g(t|\theta_0)$. The probability density of the next firing phase can then be described by transforming $g(t|\theta_0)$ into the phase form as [153]

$$f(\theta|\theta_0) = \sum_{n=0}^{\infty} g(T(n + \theta + \theta_0)|\theta_0), \tag{6.3}$$

where T is the period of the periodic input and $\int_0^1 f(\theta|\theta_0)\,\mathrm{d}\theta = 1,\ f(\theta|\theta_0) \geq 0$. Now, considering that the distribution of the initial phase θ_0, $0 \leq \theta_0 < 1$, is given by $h_0(\theta_0)$, then the distribution of the nth firing phase, $h_n(\theta)$ can be written as

$$h_n(\theta) = \int_0^1 f(\theta|\theta_0) h_{n-1}(\theta_0)\mathrm{d}\theta_0 \equiv P h_{n-1}(\theta), \quad 0 \leq \theta < 1,\ n \geq 1, \tag{6.4}$$

where P is called the Markov operator [151] with kernel $f(\theta|\theta_0)$. If the sequence of $\{P^n h_0\}$ is asymptotically stable [151, 152], it means that there exists a unique invariant density h^* such that $\lim_{n\to\infty} \|P^n h_0 - h^*\| = 0$. Therefore, the kernel $f(\theta|\theta_0)$ has all the information required to describe the dynamical evolution. For this, usually numerical methods are used to calculate FPT density [151, 153]. For the LIF model with periodic threshold, Tateno et al., [153] used a matrix representation for $f(\theta|\theta_0)$ and found the border of the stability regions of the stochastic mode locking (Arnol'd tongues).

The equivalent to the FPT densities are cycle histograms and/or interspike-interval histograms which we want to use here to show some examples of the stochastic mode-locking in the EIF neuron model. Furthermore, to evaluate the synchronisation of the firing times to the periodic input, we use the vector strength (see previous section). Another way to asses $p : q$ mod-locking solutions is using ISI scattergram which plot Δ^{n+1} against Δ^n.

The effect of noise on the firing trains can be classified to delaying or advancing the spike times (spike jitter) or/and spike adding or deleting [106, 92]. In the later case, for example, a 2:1 locking solution for a given $\sigma > 0$ may have one or more spikes per period of the input and others with no spikes, yet on average there is two spikes per two cycles of the input. In ISI scattergram, the effect of the spike jitter appears as a blur around the firing phases while the effect of spike addition or deletion appears as a new phase (point in the plot) where no corresponding point exist in the deterministic case [92]. In Fig. 6.3 (a), we show the ISI scattergram for the same parameters as in Fig. 6.2 (a 2:1 mode-locking solution) for $\sigma = 0$ (black circles) and $\sigma = 0.05$ (green circles). As can be seen,

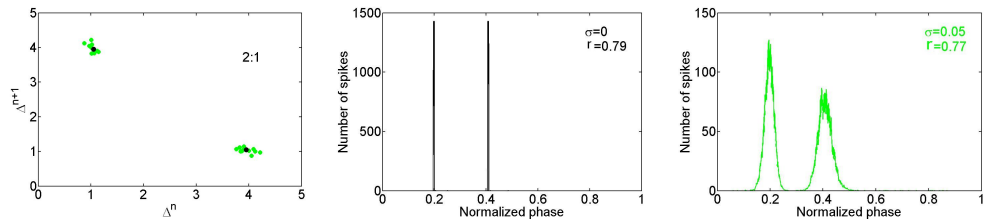

(a) (b) (c)

Figure 6.3: ISI and cycle histograms from numerical solutions of Eq. (6.1) for the same parameters as in Fig. 6.2. (a): interspike intervals for deterministic case are ≈ 4 and 1 which are jittered (green circles) by adding noise $(\sigma = 0.05)$ (b) and (c): the cycle histograms represent the unnormalized probability density of the firing as a function of the input phase. The corresponding vector strengths are also given in the plots.

noise blurs the two interspike intervals. The probability of firing as a function of the phase of the periodic input is known as a *cycle histogram*. Examples of such histograms for the 2:1 patterns are shown in Fig. 6.3 (b) and (c) for the same parameters as in panel (a). The non-noisy case, panel (b), shows two distinct firing phases, while noise, $\sigma = 0.05$, jitters the firing phases and widens their distribution, panel (c). These cycle histograms are constructed by dividing the normalized phase to 2×10^3 bins. Whenever a spike occurs at a phase of the sinusoidal input, the corresponding bin is incremented.

In Fig. 6.4, we show the effect of noise on the Arnol'd tongues structure and devil's stair case. As can be seen in the left panel, the ordered structure of the Arnol'd tongues is blurred by the stochastic input ($\sigma = 0.05$). Between the tongues the locking rotation numbers vary continuously as a function of the constant input I_0. Noise then allows for a smooth transition between mode-locking regions which are no longer limited to ratios of integers (rational number)[106]. This can also be seen in the average firing rate of the EIF model (right panel). The non-noisy case (black line) corresponds to the Arnol'd tongue structure in

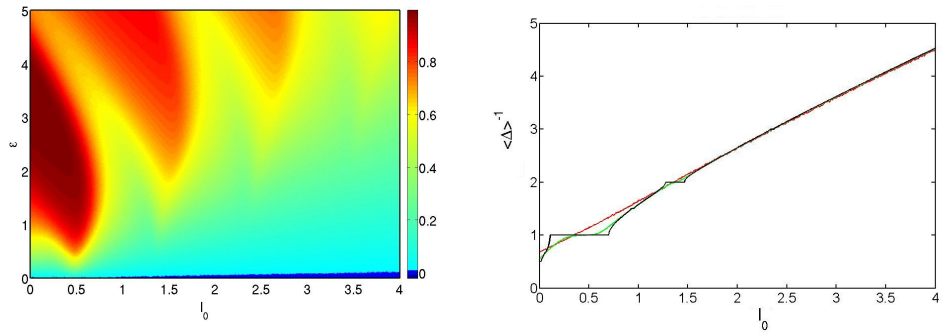

(a) (b)

Figure 6.4: Effect of noise on the Arnol'd tongues structure and devil's staircase of the EIF model as a function of I_0 and for $\epsilon = 1$. (a): vector strength is plotted for the EIF model receiving stochastic input I_{app} with $\sigma = 0.05$. The structure of Arnol'd tongues is blured, though the dominant locking solutions are still clear. (b): the firing rate of the non-noisy EIF model (black line) which each step corresponds to a rational number. By adding a small noise (green line), $\sigma = 0.05$, the dominant mode-locked solutions are still 1:1 and 2:1, although each step becomes smoother. For large noise intensity (red line), $\sigma = 0.5$, the steps disappear and the slope becomes smooth. Other parameters are as in Fig. 6.1.

Fig. 6.1. Adding noise, $\sigma = 0.05$ has the effect of smoothing the devil's staircase (green line) which corresponds to the Arnol'd tongues in panel (a) and as the noise intensity increases ($\sigma = 0.5$), the step-like structures change into a smooth slope (red line).

Chapter 7

Conclusion

I have already closed each chapter with a brief summary and discussion of results. Here, I complete the discussion with the outlook of each chapter. First the central findings of each chapter is reviewed.

In Chapter 2, I studied the response of the periodically driven RF neuron model in terms of mode-locking solutions as well as chaotic solutions. The main result of this chapter is that the existence of the subthreshold resonance causes chaotic responses when the input frequency is close to the resonance frequency. This is an important result as it was shown that the periodically driven leaky IF oscillators fail to reproduce chaotic behavior [30]. Although other modified IF neuron models such as the ghostbursting model [90] and IF with threshold fatigue [26] under periodic forcing can exhibit chaotic behavior, they cannot describe subthreshold resonant behavior. Furthermore, It is shown [19, 138] that the periodically driven RF model with additive noise would exhibit firing-rate resonance if the noise level is sufficiently large. Our result highlights that even in the absence of the noise, the subthreshold resonance reveals itself by generating chaotic firing pattern.

In Chapter 3, the EIF model was considered and the effect of fast and slow synaptic fluctuations on the steady-state firing rate was examined. The following main findings were obtained: similar to the response of the QIF model [18], the first order correction to the steady-state firing rate for fast synaptic inputs is of order of τ_s/τ_m (the ratio of synaptic time constant to the membrane time constant). This means the EIF model is less sensitive to fast filtered noise than the LIF neuron in which the firing rate decreases as $\sqrt{\tau_s/\tau_m}$ [51]. For slow noise, I approximated the firing rate in both sub- and suprathreshold regimes. In subthreshold regime, the neuron responds only if large and rare synaptic fluctuations exist. Similar behavior was observed for LIF neurons [14, 116].

In Chapter 4, I addressed the dynamics response of the EIF model subject to fast synaptic filtering when an additional weak oscillatory input is added. The central finding was deriving the linear correction of the firing-rate response to both mean input and noise intensity oscillations. Although the dynamics response of the IF neurons subject to white or coloured noise [15, 17, 51, 58, 99, 100, 148] as well as the EIF neuron with white noise [135, 141] have been previously studied, a full description of the firing-rate response of the EIF neuron with coloured noise for the whole range of the input frequency was missing. Our results in both low and high input frequencies showed similar dynamical response as for the EIF model with white noise [135].

Introducing the EIFh model in Chapter 5, I studied the effect of fast sodium inactivation on the response properties of the neuron. The important results in this chapter were: as for the EIF and QIF models [52] in the steady-state case, the response of the neuron near the critical current showed a square root dependency

on the input current. In the dynamics case, we found that fast sodium inactivation has significant effect on the response at low frequencies while at high frequencies, the amplitude of the response decreases as $1/\omega$ as in the EIF model [51, 52, 135].

Finally examples of the deterministic and stochastic mode-locking of the EIF model are given in Chapter 6.

Chapter 2:

In Chapter 2, the RF model was used to examine the effect of subthreshold resonance on the response of neurons to periodic inputs. The response to periodic inputs included $p:q$ mode-locked patterns as well as chaotic firing patterns which were the result of interaction between the internal time scales and time scales of the input. Using a one-dimensional time map arising through the study of the RF system together with smooth and nonsmooth bifurcations, we determined mode-locked solutions and found their stability regions (Arnol'd tongues) analytically. The existence of the subthreshold resonance caused chaotic responses when the input frequency was close to the resonant frequency. A resetting function imposed on the RF system was defined to map both the voltage and the resonant current. If the resonant current has time scales slower than the voltage dynamics, it is more realistic to reset just the voltage. This results in a two-dimensional firing-time map. The study of this map and the dynamics of the firing times in terms of periodic and chaotic still need to be done. The RF model has the advantage of being piecewise linear which we used in our analysis, however, as for the LIF model, it does not generate real action potentials. A possible treatment would be adding a spike-generating current into the voltage dynamics. This current, as

for the EIF model [52], can have an exponential form representing the activation of the sodium current. In the context of mode locking, it is worth exploring how periodic forcing can be transduced in this modified model and how the underlying subthreshold resonance influences this transduction.

Experimental results show that cortical neurons in *vivo* are subject to a considerable amount of synaptic noise. The effect of such stochastic input on neuronal response is another important factor that should be taken into account. Stochastic forcing turns a quiescent excitable system into a stochastic oscillator and in suprathreshold regimes, turns the deterministic oscillator into a noise-perturbed oscillator [91]. Noise also smooths the input-output curve and can significantly alter $p : q$ deterministic mode-locking structures [109, 153, 107]. Recently, stochastic mode locking was studied in ventral cochlear nucleus chopper and onset neurons [92]. In stochastic mode locking, firing are caused by the combination of noise and periodic forcing. While noise randomly creates firing in the subthreshold regime, it can also destroy firing that are otherwise mode locked to a periodic input in the suprathreshold regime. It can cause *skipping* observed in mechanoreceptors [42], the hair cells of the auditory system, receptors of the electrosensory systems, and in the primary visual cortices [108]. Skipping was also shown [104] for the FitzHugh-Nagumo model in the suprathreshold regime, which was due to the action of noise on chaotic dynamics. It was also observed in a chaotic map based on excitable dynamics [80]. It is worth studying stochastic mode locking, skipping, and the underlying stochastic bifurcations for periodically forced RF neurons with filtered synaptic inputs. Apart from this, noise may enhance the regularity of firing (*coherence resonance*) [105, 97, 98, 100, 128], can allow encoding subthreshold

inputs via *stochastic resonance* [56, 99], and produce *mean-frequency locking* [96]. These phenomena can be studied by means of ISI histograms and power spectral density [96, 100] which would help in the understanding of the following questions: does the noise regularize the neural firing with or without forcing? under which conditions is the periodic forcing best expressed in the output spike train given that without noise, it does not cause firing? how does the underlying subthreshold resonance influence the noise-induced firing? and how can noise help coding aperiodic signals [24, 27]. Further studies are required to answer these questions for RF neurons. It was also shown that in a periodically forced RF neuron fluctuating synaptic inputs helps the subthreshold resonance properties to be revealed [19], i.e., a sufficiently large amount of noise is necessary for the subthreshold resonance to be able to create a firing-rate resonance. This result was obtained in the limit of slow resonant current compared to the membrane potential dynamics by using a probability density approach similar to the method we used in Chapters 3 and 4. It would be interesting to use this approach and obtain the effect of filtered synaptic fluctuations on the firing-rate response of the RF neuron in the limit of fast resonant currents. The study of the RF neuron with or without noise is also important at the network level where underlying conditions for synchronized and desynchronized states need to be investigated. In conclusion, exploring these ideas and questions for the RF neuron would increase our understanding of the behavior of resonant neurons.

Chapters 3 and 4:

We examined the effects of filtered synaptic fluctuations on the input-output prop-

erties of a population of postsynaptic EIF neurons. Using a population density method [17, 51], we obtained an approximation to the steady-state firing rate in Chapter 3 and presented, in Chapter 4, the linear response theory for the firing rate of the model in response to both time-dependent input currents and time-dependent noise intensity. Population density methods are usually used to study stochastic models of neurons theoretically and numerically. These methods in principle turn the liability of a large number of stochastic single neurons into an advantage. If the stochastic behavior of thousands of single neurons should be followed, the number of related equations can be huge. Solving such a large system of equations would be a computational problem. Instead, one may track the distribution of neurons over state space. The population density method used here utilized the Fokker-Planck formalism and a perturbative approach [15, 16, 51, 116] from which the steady-state and dynamics distribution of the membrane potential and the rate density were approximated. The threshold integration method [135] was then adapted to calculate these approximations. There are other approaches on the probability density such as implicit methods for numeric solving of the Fokker-Planck equation [127, 66]. By considering realistic synaptic kinetics and/or several types of excitation and inhibition and also different types of ionic currents, the dimension of state variables increases and there would be a real concern on the computation time of the numerical solution using implicit methods [22, 127, 70] or direct numerical simulations. Therefore, a computationally efficient and tractable method is a real need. One possible candidate is the threshold integration method. Many important quantities that characterize the dynamics of networks of EIF neurons can also be obtained using this method [136, 137]. There-

fore, we hope that the threshold integration method would serve as a time-saving computational tool especially if it is applied to large-scale modeling of neuronal networks.

In the majority of theoretical and experimental works, diffusion approximation (due to high presynaptic rates and low postsynaptic potential amplitude) are used to model fluctuating synaptic inputs with a Gaussian noise and the effects of shot noise (due to low rate poisson distributed presynaptic inputs) are ignored. It has recently been shown [69, 139, 140, 141] that shot noise gives substantial improvement over the results given by the conventional Fokker-Planck equation that assumes Gaussian noise. Further, temporal correlation of synaptic inputs [23, 36] has significant impacts on firing properties of neurons. Câteau and Reyes [23] modeled synaptic noise with a coloured noise whose autocorrelation had a negative component. This is different from the coloured noise we used here in which the autocorrelation decays exponentially without a negative component. Therefore, developing the methods used here to take into account such temporal correlations in synaptic input or synaptic shot noise is worth pursuing. It would be particularly interesting to study how they influence the firing-rate response of the EIF neuron and the collective response of networks of EIF neurons. As for the RF neuron, similar discussion from the stochastic resonance point of view can be given here. Whether a synaptic noise can enhance the sensitivity of the EIF neuron to weak inputs and in the context of coherence resonance, can regularize the spike train of the neuron still need to be examined. Understanding how the properties of single neurons affect the collective properties of networks of neurons is also crucial. The linear firing-rate response of the EIF neuron determined in

Chapter 4 is a key quantity in the analysis of this question and the determination of the conditions of network oscillations as was previously studied for LIF neurons [15, 16, 20, 57] and for networks of excitatory neuron with adaptation current [55]. Therefore, the methods and results obtained in Chapters 3 and 4 would allow for an analysis of the role of synaptic noise in the collective behavior of networks of EIF neurons. Similar discussions as in Chapter 2 regarding deterministic and stochastic mode locking can be given here, whether the periodically forced EIF neuron model can exhibit chaotic behaviour is also worth studying. Finally, our findings reveal that the EIF model retains the dynamical behavior of type I HH-type neurons while still being tractable (analytically and numerically). An important feature of the EIF model is the spike-generating mechanism which is the main factor of the dynamics response of neurons. In the LIF model, which does not incorporate a dynamic action potential onset, the response to high-frequency inputs is instantaneous [17, 51]. This behavior disagrees with the response of conductance-based models [52, 123]. Our results on the linear response amplitude of the EIF model showed a $1/\omega$ decay at high frequencies such that increasing the action potential onset speed (by decreasing Δ_T) can cause lifting the response amplitude to a larger transmission amplitude, enabling the neuron to respond to larger frequencies. In conclusion, these features make the EIF model practically suitable for gaining a better understanding of response properties of cortical neurons, in particular in information processing. However, a major weakness of this model is that it does not produce the threshold potential variability observed in experimental studies of cortical neurons [126]. In Chapter 5, the EIF model was improved to capture this behavior.

Chapters 5:

We introduced a modified model of the EIF model referred to as the EIFh model which incorporates the dynamics of fast inactivation of the sodium current, h. The steady-state and dynamics response properties of the EIFh model with filtering synaptic inputs were studied. The results were also compared with those of the EIFh$_\infty$ model in which the inactivation variable is instantaneous. Both models showed similar steady-state characteristics. The results of the dynamic response of these models when subjected to fast synaptic fluctuations showed similar behaviors at low frequencies and a $1/\omega$ decay of the response amplitude in high-frequency limits which was the case for the EIF model. The response amplitude of the EIFh model at high frequencies, however, was shifted to a larger transmission amplitude relative to that of the EIFh$_\infty$ model and at the same level of the EIF response amplitude. For the computation of the linear response amplitude of the EIFh$_\infty$ model, we used the linear response theory and the perturbative approach given in Chapters 3 and 4, while for the corresponding result of the EIFh model, we restored to direct numerical simulations. It would be of great interest to develop the methods used for the EIFh$_\infty$ to compute the linear response of the EIFh model. Due to the existence of two small parameters, fast kinetics of the h variable (τ_h) and short synaptic time constant (τ_s), a possible way would be performing the perturbation in both τ_h/τ_m and τ_s/τ_m limits and finding the first order correction to the probability density in both parameters. The EIF model with fast inactivation can produce realistic action potentials with rapid dynamics as well as variable onset potential. These are key features of the initiation dynamics of cortical neuron action potential which play important role in encoding of fast signals [126]. Al-

though our results on the filtering properties derived in the framework of the EIFh and EIFh$_\infty$ models did not show any qualitative difference with the EIF neuron, another inactivating mechanism of sodium channels has been known experimentally [50, 113] which has slow onset and recovery and which is distinct from the fast inactivation. We expect it would have different effects on response properties of neurons. Such slow mechanisms of inactivation carry the memory of previous spikes and can increase the ISI after a spike. It can also cause slow spike-frequency adaptation [50, 10]. Further studies are required to determine functional impacts of slow inactivation on neuronal response properties, particularly on the response of neurons to rapidly varying inputs. We propose a new model based on the EIF model by including the slow inactivation dynamics. Similar to the EIFh model, this model can capture key features of the action potential of cortical neurons. It remains to examine the information processing of the EIF model with slow inactivation which would increase our understanding of the response properties of neurons in particular in the region of action potential generation. For a similar mechanism in which the threshold voltage carries memory [24], it is shown that the synaptic noise may enhance encoding of a periodic input. Another idea would be studying the effect of the slow inactivation on spike timing of the EIF model in terms of stochastic resonance and coherence resonance.

Appendix A

Threshold integration method

In this section, we describe the threshold integration method [135, 136]. This method allows for a fast computation and high numerical precision, hard to achieve by direct numerical simulations. We use this method to compute the steady-state and dynamics firing rate of the EIF neuron obtained in Chapters 3 and 4.

A.1 The steady-state firing rate

In the fast synaptic limit, the first- and second-order contribution to the steady-state firing rate, given by Eqs. (3.27) and (3.38), are composed of double integrals and hence not easy to compute. To deal with this problem, we first compute integrals in Eqs. (3.25) and (3.37) numerically. These integrals satisfy a differential equation of the form

$$-\partial_V Q = GQ + \mathcal{E}, \quad Q(V_{th}) = 0, \tag{A.1}$$

where $G(V) = -f(V)/\sigma^2$ and $\mathcal{E}$ is a function of voltage. Eq. $(A.1)$ can be solved by backward integration from V_{th} to a lower bound V_{lb} with step size δV and

writing the solution at each point as

$$Q(V_{k-1}) = Q(V_k)\exp\Big(\int_{V_{k-1}}^{V_k} G(u)\,\mathrm{d}u\Big) + \int_{V_{k-1}}^{V_k} \mathcal{E}(u)\exp\Big(\int_{V_{k-1}}^{u} G(w)\,\mathrm{d}w\Big)\,\mathrm{d}u, \tag{A.2}$$

where $V_0 = V_{lb}$, $V_n = V_{th}$ and $k = 0, \ldots, n$. By expanding G and $\mathcal{E}$ around the value V_k to zero order in δV, expression ($A.2$) is approximated by

$$Q(V_{k-1}) \simeq Q(V_k)A_k + \delta V B_k \mathcal{E}(V_k), \quad k = 0, \ldots, n \tag{A.3}$$

where $A_k = \exp\big(\delta V G(V_k)\big)$, $B_k = \big(\exp\big(\delta V G(V_k)\big) - 1\big)/\big(\delta V G(V_k)\big)$ and $B_k = 1$ when $G(V_k) = 0$.

In zero order, from Eq. (3.25), we have $\mathcal{E}(V) = (\tau_m/\sigma^2)\Theta(V - V_{re})$ and since $\int Q_0\ \mathrm{d}V = 1$, we obtain $r_0 = 1/\big(\delta V \sum_{k=0}^{n} Q(V_k)\big)$. Similarly, for the second order, Eq. (3.37) results in $\mathcal{E}(V) = (3/2)\partial_V^2 f Q_0 + 2\partial_V f \partial_V Q_0$. Therefore, combining the normalization condition, $\int Q_2\,\mathrm{d}V = 0$ and Eq. (3.38), we find

$$r_2 = -r_0\delta V \sum_{k=0}^{n} Q(V_k) + r_0^2\tau_m\delta_V\Big[\frac{1}{\Delta T} + \frac{3}{2}\frac{f(V_{re})}{\sigma^2}\Big]\sum_{k=0}^{m}\exp\big(\psi(V_{re}, V_k)\big) - \frac{3}{2}r_0^2\tau_m,$$

where $V_m = V_{re}$.

A.2 The dynamics response

In the dynamics case, the first- and second-order contribution to $\hat{r}(\omega)$ are obtained by solving systems of equations in the following form

$$\begin{aligned} -\partial_V\hat{Q} &= G\hat{Q} + \frac{\tau_m}{\sigma^2}\hat{g} + \mathcal{E}, \\ -\partial_V\hat{g} &= i\omega\hat{Q} + \mathcal{H} - \hat{r}\delta(V - V_{re}). \end{aligned} \tag{A.4}$$

This holds for both mean inputs (see systems of equations (4.28) and (4.38)) and noise intensity modulations (see systems of equations (4.54) and (4.59)). Systems

of this form are easily solved by separating solutions as

$$\hat{Q} = \hat{r}\hat{Q}_h + \hat{Q}_p, \quad \hat{g} = \hat{r}\hat{g}_h + \hat{g}_p. \tag{A.5}$$

Therefore, the pair $\hat{Q}_h$ and $\hat{g}_h$ satisfy the system

$$\begin{aligned} -\partial_V \hat{Q}_h &= G\hat{Q}_h + \frac{\tau_m}{\sigma^2}\hat{g}_h, \\ -\partial_V \hat{g}_h &= i\omega\hat{Q}_h - \delta(V - V_{re}), \end{aligned} \tag{A.6}$$

with initial conditions $\hat{Q}_h(V_{th}, \omega) = 0$ and $\hat{g}_h(V_{th}, \omega) = 1$. The pair $\hat{Q}_p$ and $\hat{g}_p$ address the non-homogeneous solution and satisfy the system

$$\begin{aligned} -\partial_V \hat{Q}_p &= G\hat{Q}_p + \frac{\tau_m}{\sigma^2}\hat{g}_p + \mathcal{E}, \\ -\partial_V \hat{g}_p &= i\omega\hat{Q}_p + \mathcal{H}, \end{aligned} \tag{A.7}$$

with initial conditions $\hat{Q}_p(V_{th}, \omega) = 0$ and $\hat{g}_p(V_{th}, \omega) = 0$.

Now, using the same integration scheme used for the steady state, one can integrate systems $(A.6)$ and $(A.7)$ from V_{th} to the lower bound V_{lb} and write the solution at each step. This produces, for the homogeneous part

$$\begin{aligned} \hat{Q}_h(V_{k-1}, \omega) &= \hat{Q}_h(V_k, \omega)A_k + \frac{\tau_m}{\sigma^2}\delta_V B_k \hat{g}_h(V_k, \omega), \\ \hat{g}_h(V_{k-1}, \omega) &= \hat{g}_h(V_k, \omega) + \delta_V \mathcal{H}(V_k, \omega) - \delta(V_k - V_{re}), \quad k = 0, \ldots, n \end{aligned}$$

with initial conditions $\hat{Q}_h(V_n, \omega) = 0$ and $\hat{g}_h(V_n, \omega) = 1$. For non-homogeneous part, we have

$$\begin{aligned} \hat{Q}_p(V_{k-1}, \omega) &= \hat{Q}_p(V_k, \omega)A_k + \delta_V B_k \Big(\frac{\tau_m}{\sigma^2}\hat{g}_p(V_k, \omega) + \mathcal{E}(V_k)\Big), \\ \hat{g}_p(V_{k-1}, \omega) &= \hat{g}_p(V_k, \omega) + \delta_V \mathcal{H}(V_k, \omega), \quad k = 0, \ldots, n \end{aligned}$$

with initial conditions $\hat{Q}_p(V_n, \omega) = 0$ and $\hat{g}_p(V_n, \omega) = 0$. Therefore, the corrections to the firing-rate response can be readily obtained for the mean inputs oscillations

from Eqs. (4.30) and (4.43), and for the noise intensity oscillations from Eqs. (4.55) and (4.62).

Appendix B

Gating variables of conductance-based models

B.1 Hodgkin-Huxley model

Introduced by Hodgkin and Huxley [68], the Hodgkin-Huxley (HH) model is a single compartment model with one sodium, potassium, and leakage current satisfying

$$C\frac{dV}{dt} = -I_L - I_{Na} - I_K + I_{app}, \tag{B.1}$$

where C is the membrane capacitance ($C = 1\ \mu\text{F/cm}^2$), $I_L = \bar{g}_L(V - E_L)$ is the leak current ($\bar{g}_L = 0.3$ mS/cm^2; $E_L = -68$ mV), $I_{Na} = \bar{g}_{Na}m^3h(V - E_{Na})$ is the sodium current, $I_K = \bar{g}_K n^4(V - E_K)$ is the potassium current, and I_{app} is the input current.

The dynamical equations for gating variables are

$$\frac{dw}{dt} = \alpha_w(V)(1 - w) - \beta_w(V)w, \tag{B.2}$$

where $w = n, m,\ h$. It is also conventional to write Eq. ($B.2$) as

$$\tau_w(V)\frac{dw}{dt} = w_\infty(V) - w, \tag{B.3}$$

where $\tau_w = [\alpha_w + \beta_w]^{-1}$ is the time constant of w and $w_\infty = \alpha_w/[\alpha_w + \beta_w]$ is the final (steady-state) value of w for a particular voltage.

The specific functions for α_w and β_w proposed by Hodgkin and Huxley are

$$\alpha_m = \frac{0.1(V+35)}{1-\exp[-0.1(V+35)]}, \qquad \beta_m = 4\exp[-(V+60)/18], \tag{B.4}$$

$$\alpha_h = 0.07\exp[-(V+58)/20], \qquad \beta_h = \frac{1}{\exp[-0.1(V+28)]+1}, \tag{B.5}$$

$$\alpha_n = \frac{0.01(V+34)}{1-\exp[-0.1(V+34)]}, \qquad \beta_n = 0.125\exp[-(V+44)/80]. \tag{B.6}$$

The maximum conductance densities and the reversal potentials of the ionic currents are $\bar{g}_{Na} = 120$ ms/cm^2, $E_{Na} = 55$ mV, $\bar{g}_K = 36$ ms/cm^2, and $E_K = -72$mV.

B.2 Wang-Buzsáki model

The Wang-Buzsáki (WB) model was introduced by Wang and Buzsáki [160] which is a modified version of the original HH model with type I dynamics.

The WB membrane voltage is governed by Eq. (B.1) where I_{Na} and I_K are identical to the HH equation except that WB model makes the simplifying assumption that the sodium activation is instantaneous. The dynamical equation of each gating variable satisfies Eq. (B.2) and the corresponding parameters of gating variables are given by Eqs (B.4)-(B.6).

B.3 Moris-Lecar model

The parameters values for the Moris-Lecar model are as follow: $E_K = -70$ mV, $E_L = -50$ mV, $E_{Ca} = 100$ mV, $\bar{g}_K = 2$ mS/cm^2, $\bar{g}_{Ca} = 1$ mS/cm^2, $g_L = 0.5$

mS/cm^2, $V_1 = -1$ mV, $V_2 = 15$ mV, $V_3 = 10$ mV, $V_4 = 14.5$ mV, and $\phi = 0.333$ (ms)$^{-1}$.

B.4 Pushchino model

The Pushchino model [82] is a piecewise linear model of the Fitzhugh-Nagumo model with $f(V)$ and $g(V)$ defined as follow

$$f(V) = \begin{cases} -30V, & V < V_1, \\ \gamma V - 0.12, & V_1 < V < V_2, \\ -30(V-1), & V > V_2, \end{cases} \tag{B.7}$$

$$g(V,w) = \frac{1}{\tau(V)}(V-w), \quad \tau(V) = \begin{cases} 2, & V < V_1, \\ 16.6, & V > V_1, \end{cases} \tag{B.8}$$

with $V_1 = 0.12/(30+\gamma)$ and $V_2 = 30.12/(30+\gamma)$.

Bibliography

[1] Abbott, L. F. & Kepler, T. B. (1990). "*Model neurons: from Hodgkin-Huxley to Hopfield*", In: Garridol (ed) Statistical mechanics of neural networks, Springer.

[2] Aihara, K., Matsumoto, G. & Ikegaya, Y. (1984). "Periodic and non-periodic responses of a periodically forced Hodgkin-Huxley oscillator", *J. Theor. Biol.* **109**, 249-269.

[3] Amit, D. J. & Tsodyks, M. V. (1991). "Quantitative study of attractor neural network retrieving at low spike rates I: Substrate-spikes, rates and neuronal gain", *Network*, **2**, 259-274.

[4] Amit, D. J. & Brunel, N. (1997). "Dynamics of a recurrent network of spiking neurons before and following learning", *Network*, **8**, 373-404.

[5] Amit, D. J. & Brunel, N. (1997). "Model of global spontaneous activity and local structured activity during delay periods in the cerebral cortex", *Cerebral Cortex*, **7**, 237-252.

[6] Anderson, J. S., Lampl, I., Gillespie, D. C. & Ferster, D. (2000). "The contribution of noise to contrast invariance of orientation tuning in cat visual cortex", *Science* **290**, 1968-1972.

[7] Ascoli, C., Barbi, M., Chillemi, S. & Petracchi, D. (1977). "Phase-locked responses in the limulus lateral eye. Theoretical and experimental investigation", *Biophys. J.* **19**, 219-240.

[8] Badel, L., Lefort, S., Brette, R., Petersen, C. C. H., Gerstner, W. & Richardson, M. J. E. (2008). "Dynamic I-V curves are reliable prediction of naturalistic pyramidal-neuron voltage traces", *J. Neurophysiol.* **99**, 656-666.

[9] Badel, L., Lefort, S., Berger, T. K., Petersen, C. C. H. Gerstner, W. & Richardson, M. J. E. (2008). "Extracting nonlinear integrate-and-fire models from experimental data using dynamic I-V curves", *Biol. Cybern.* **99**, 361-370.

[10] Benda, J. & Herz, A. V. M. (2003). "A universal model for spike-frequency adaptation", *Neural Comput.* **15**, 2523-2564.

[11] Bernardo, M. di, Budd, C. J., Champneys, A. R. & Kowalczyk, P. (2008). "*Piecewise-Smooth dynamical systems, theory and applications*", Applied mathematical sciences, Springer, New York.

[12] Bezzi, M., Nieus, T., Coenen, O. T. -M. & D'angelo, E. (2004). "An Integrate-and-fire model of a cerebellar granule cell", *Neurocomputing* **58-60**, 593-598.

[13] Boyland, P. L. (1986). "Bifurcations of circle maps, Arnol'd tongues, Bistability and rotation interval", *Commun. Math. Phys.* **106**, 353-381.

[14] Brunel, N. & Sergi, S. (1998). "Firing frequency of integrate-and-fire neurons with finite synaptic time constants", *J. Theor. Biol.* **195**, 87-95.

[15] Brunel, N. & Hakim, V. (1999). "Fast global oscillations in networks of integrate-and-fire neurons with low firing rates", *Neural Comput.*, **11**, 1621-1671.

[16] Brunel, N. (2000). "Dynamics of sparsely connected networks of excitatory and inhibitory spiking neurons", *J. Comput. Neurosci.* **8**, 183-208.

[17] Brunel, N., Chance, F., Fourcaud, N. & Abbott, L. (2001). "Effects of synaptic noise and filtering on the frequency response of spiking neurons", *Phys. Rev. Lett.* **86**, 2186-2189.

[18] Brunel, N. & Latham, P. (2003). "Firing rate of the noisy quadratic integrate-and-fire neuron", *Neural Comput.* **15**, 2281-2306.

[19] Brunel, N., Hakim, V. & Richardson, M. J. E. (2003). "Firing-rate resonance in generalized integrate-and-fire neuron with subthreshold resonance", *Phys. Rev. E* **67**, 051916-051939.

[20] Brunel, N. & Wang, X., J. (2003). "What determines the frequency of fast network oscillations with irregular neural discharges? I.

Synaptic dynamics and excitation-inhibition balance", *J. Neurophysiol.* **90**, 415-430.

[21] Burkitt, A. (2006), "A review of the integrate-and-fire neuron model. I. Homogeneous synaptic input", *Biol. Cybern.* **95**, 1-19.

[22] Casti, A. R., Omurtag, A., Sornborger, A., Kaplan, E., Knight, B., Victor, J. & Sirovich, L. (2002). "A population study of integrate-and-fire-or-burst neurons", *Naural Comput.* **14**, 957-986.

[23] Câteau, H. & Reyes, A. D. (2006). "Relation between single neuron and population spiking statistics and effects on network activity", *Phys. Rev. Lett.* **96**, 058101.

[24] Chacron, M. J., Longtin, A., St-Hilaire, M. & Maler, L. (2000). "Suprathreshold stochastic firing dynamics with memory in p-type electroreceptors", *Phys. Rev. Lett.* **85**, 1576-1579.

[25] Chacron, M. J., Pakdaman, K. & Longtin, A. (2003). "Interspike interval correlations, memory, adaptation, and refractoriness in a leaky integrate-and-fire model with threshold fatigue", *Neural Comput.* **15**, 253-278.

[26] Chacron, M. J., Longtin, A. & Pakdaman, K. (2004). "Chaotic firing in sinusoidally forced leaky integrate-and-fire model with threshold fatigue", *Physica D* **192**, 138-160.

[27] Chialvo. D. R., Longtin, A. & Müller-Gerking, J. (1997). "Stochastic resonance in models of neuronal ensembles", *Phys. Rev. E* **55**, 1798-1808.

[28] Cole, K. S. (1941). "Rectification and inductance in the squid giant axon", *J. Gen. Physyiol.* **25**, 29-51.

[29] Cole, K. S., Guttman, R. & Bezanilia, F. (1970). "Nerve membrane excitation without threshold", *Proc. Natl. Acad. Sci. U.S.A.* **65**, 884-891.

[30] Coombes, S. & Bressloff, P. C. (1999). "Mode-locking and Arnol'd tongues in Integrate-and-fire neural oscillators", *Phys. Rev. E* **60**, 2086-2096.

[31] Coombes, S. (1999). "Liapunov exponents and mode-locked solutions for Integrate-and-fire dynamical systems", *Phys. Lett. A* **255**, 49-57.

[32] Coombes, S. (2001) "Phase-locking in networks of pulse-coupled McKean relaxation oscillators", *Physica D* **2820**, 1-16.

[33] Coombes, S. (2008) "Neuronal networks with gap junctions: a study of piece-wise linear planar neurons", *SIAM J. Appl. Dyn. Syst.* **7**, 1101-1129.

[34] Coombes, S. & Bressloff, P. C. (2001). "Erratum: Mode-locking and Arnol'd tongues in Integrate-and-fire neural oscillators", *Phys. Rev. E* **63**, 059901.

[35] Coombes, S., Owen, M. R. & Smith, G. D. (2001). "Mode-locking in periodically forced Integrate-and-fire-or-burst neuron model", *Phys. Rev. E* **64**, 041914.

[36] de la Rocha, J., Doiron, B., Shea-Brown, E., Josic, K. & Reyes, A. (2007). "Correlation between neural spike trains increases with firing rate", *Nature* **448**, 802-806.

[37] Dayan, P. & Abbott, L. F. (2001). "*Theoretical Neuroscience Computational and Mathematical Modeling of Neural Systems*", The MIT Press.

[38] Destexhe, A., Mainen, Z. F. & Sejnowski, T. J. (1998). "Kinetic models of synaptic transmission. In C. Koch & I. Segev (Eds), *Methods in neuronal modelling* (2nd ed., pp.1-25)", Cambridge, MA: MIT Press.

[39] Destexhe, A. & Paré, D. (1999). "Impact of network activity on the integrative properties of neocortical pyramidal neurons in vivo", *J. Neurophysiol.* **81**, 1531-1547.

[40] Destexhe, A., Rudolph, M. & Sejnowski, T. J. (2001). "Fluctuating synaptic conductances recreate in *vivo*-like activity in neocortical neurons ", *Neuroscience* **107**, 13-24.

[41] Doedel, E. J., Champneys, A. R., Fairgrieve, T. F., Kuznetsov, Yu. A., Sandstede, B. & Wang, X. (1997). "*Auto97: Continuation and bifurcation software for ordinary differential equations*", Technical report, Concordia University.

[42] Douglass, J. K., Wilkens, L., Pantazelou, E. & Moss, F. (1993). "Noise enhancement of information transfer in crayfish mechanoreceptors by stochastic resonance", *Nature* **365**, 337-340.

[43] Doiron, B., Lindner, B., Longtin, A., Maler, L. & Bastian, J. (2004). "Oscillatory activity in electrosensory neurons increases with the spatial correlation of the stochastic input stimulus", *Phys. Rev. Lett.* **93**, 048101-048105.

[44] Ermentrout, G. B. & Kopell, N. (1986). "Parabolic bursting in an excitable system coupled with a slow oscillation", *SIAM J. Appl. Math.* **46**, 233-253.

[45] Ermentrout, G. B. (1996). "Type I membranes, phase resetting curves, and synchrony", *Neural Comput.* **8**, 979-1001.

[46] Ermentrout, G. B. (1998). "Linearization of *f-I* curves by adaptation", *Neural Comput.* **10**, 1721-1729.

[47] Ermentrout, B. (2002). "*Simulating, analysing, and animating dynamical systems: a guide to XPPAUT for researcher and students*", SIAM.

[48] Ermentrout, G. B. & Terman, D. H. (2010). "*Mathematical foundations of neuroscience*", Springer, New York.

[49] Fitzhugh, R. (1961). "Impulse and physiological stages in theoretical models of nerve membrane.", *Biophys. J.* **1**, 445-466.

[50] Fleidervish, I. A., Friedman, A. & Gutnick, M. J. (1996). "Slow inactivation of Na^+ current and slow cumulative spike adaptation in mouse and guinea-pig neocortical neurons in slices", *Journal of Physiology* **493**, 83-97.

[51] Fourcaud, N. & Brunel, N. (2002). "Dynamics of the firing probability of noisy integrate-and-fire neurons", *Neural Comput.* **14**, 2057-2110.

[52] Fourcaud, N., Hansel, D., Vreeswijk, C. & Brunel, N. (2003). "How spike generation mechanisms determine the neuronal response to fluctuating inputs", *J. Neurosci.* **23**, 11628-11640.

[53] Fourcaud, N. & Brunel, N. (2005). "Dynamics of the instantaneous firing rate in response to changes in input statistics", *J. Comput. Neurosci.* **18**, 311-321.

[54] French, A. S., Holden, A. V. & Stein, R. B. (1972). "The stimulation of the frequency response function of a mechanoreceptor", *Kybernetika* **11**, 15-23.

[55] Fuhrmann, G., Markram, H. & Tsodyks, M. (2002). "Spike frequency adaptation and neocortical rhythms", *J. Neurophysiol.* **88**, 761-770.

[56] Gammaitoni, L., Hänggi, P., Jung, P. & Marchesoni, F. (1998). "Stochastic resonance", *Reviews of Modern Physics*, **70**, 223-287.

[57] Geisler, C., Brunel, N. & Wang, X. J. (2005). "Contributions of intrinsic membrane dynamics to fast network oscillations with irregular neuronal discharges", *J. Neurophysiol.* **94**, 4344-4361.

[58] Gerstner, W. (2000). "Population dynamics of spiking neurons: fast transient, asynchronous states, and locking", *Neural Comput.* **12**, 43-89.

[59] Gerstner, W. & Kistler, W. (2002). "*Spiking neuron models single neurons, populations, plasticity*", Cambridge University Press.

[60] Glass, L., Graves, C., Petrillo, G. A. & Mackey, M. C. (1980). "Unstable dynamics of periodically driven oscillator in the presence of noise", *J. Theor. Biol.* **86**, 455-476.

[61] Gutfreund, Y., Yarom, Y. & Segev, I. (1995). "Subthreshold oscillations and resonant frequency in guinea-pig cortical neurons: physiology and modelling", *J. Physiol. (London)* **483**, 621-640.

[62] Hagan, P. S., Doering, C. R. & Levermore, C. D. (1989). "Mean exit times for particles driven by weakly colored noise", *SIAM J. App. Math.* **49**, 1480-1513.

[63] Hansel, D. & Mato, G. (2001). "Existence and stability of persistent states in large neuronal networks", *Phys. Rev. Lett.* **10**, 4175-4178.

[64] Hansel, D. & Mato, G. (2003). "Asynchronous states and the emergence of synchrony in large networks of interacting excitatory and inhibitory neurons", *Neural. Comput.* **15**, 1-56.

[65] Hayashi, H., Ishizuka, S., Ohta, M. & Hirakawa, K. (1982). "Chaotic behavior in the Onchidium giant neuron under sinusoidal forcing", *Phys. Lett. A* **88**, 435-438.

[66] Haskell, E., Nykamp, D. Q. & Tranchina, D. (2001). "A population density method for large-scale modelling of neuronal networks with realistic synaptic kinetics", *Neurocomputing* **38-40**, 627-632.

[67] Higham, D. (2001). "An Algorithmic introduction to numerical simulation of stochastic differential equations", *SIAM Review*, **43**, 525-546.

[68] Hodgkin, A. L. & Huxley, A. F. (1952). "A qualitative description of ion currents and its applications to conduction and excitation in nerve membranes", *J. Physiol. (London)* **117**, 500-544.

[69] Hohn, N. & Burkitt, A. N. (2001). "Shot noise in the leaky integrate-and-fire neuron", *Phys. Rev. E* **63**, 031902-031912.

[70] Huertas, M. A. & Smith, G. D. (2006). "A multivariate population density model of the dLGN/PGN relay", *J. Comput. Neurosci.* **21**, 171-189.

[71] Hutcheon, B., Miura, R. M., Yarom, Y. & Puil, E. (1994). "Low threshold calcium current and resonance in thalamic neurons: a model of frequency preference", *J. Neurophysiol.* **71**, 583-594.

[72] Hutcheon, B., Miura, R. M. & Puil, E. (1996). "Subthreshold membrane resonance in neurocortical neurons", *J. Neurophysiol.* **76**, 683-697.

[73] Hutcheon, B., Miura, R. M. & Puil, E. (1996). "Models of subthreshold membrane resonance in neocortical neurons", *J. Neurophysiol.* **26**, 698-714.

[74] Hutcheon, B. & Yarom, Y. (2000). "Resonance, oscillation and intrinsic frequency preferences of neurons", *Trends Neurosci.* **23**, 216-222.

[75] Izhikevich, E. (2000). "Neural excitability, spiking and bursting", *Int. J. Bifurcat. Chaos* **10**, 1171-1266.

[76] Izhikevich, E. (2001). "Resonate-and-fire neurons", *Neural Networks* **14**, 883-894.

[77] Izhikevich, E. (2002). "Resonance and selective communication via bursts in neuron having subthreshold oscillations", *Biosystems* **67**, 95-102.

[78] Izhikevich, E. (2007). "*Dynamical systems in neuroscience: The geometry of excitability and bursting*", The MIT Press.

[79] Jahnsen, H. & Karnup, S. (1994). "A Spectral analysis of the integration of artificial synaptic potentials in mammalian central neurons", *Brain Res.* **666**, 9-20.

[80] Kaplan, D. T., Clay, J. R., Manning, T., Glass, L., Guevara, M. R. & Shrier, A. (1996). "Subthreshold dynamics in periodically stimulated squid giant axons", *Phys. Rev. Lett.* **76** (21), 4074-4077.

[81] Keener, J. P., Hoppensteadt, F. C. & Rinzel, J. (1981). "Integrate-and-fire models of nerve membrane responses to oscillatory input", *SIAM J. Appl. Math.* **41** (3), 503-517.

[82] Keener, J. & Sneyd, J. (1998). "*Mathematical physiology*", Interdisciplinary applied mathematics, Springer.

[83] Kepler, T. B., Abbott, L. F. & Marder, E. (1992). "Reduction of conductance-based neuron models", *Biol. Cybern* **66**, 381-387.

[84] Knight, B. W. (1972). "Dynamics of encoding in a population of neurons", *J. Gen. Physiol.* **59**, 734-766.

[85] Knight, B. W., Omurtag, A. & Sirovich, L. (2000). "The approach of a neuron population firing rate to a new equilibrium: An exact theoretical result", *Neural Comput.* **12**, 1045-1055.

[86] Koch, C. (1984). "Cable theory in neurons with active, linearized membranes", *Biol. Cybern.* **50**, 15-33.

[87] Koch, C. (1999). "*Biophysics of computation, Information processing in single neurons*", Oxford University Press.

[88] Krinskii, V. I. & Kokoz, Y. M. (1973). "Analysis of equations of excitable membranes. 1. Reduction of the Hodgkin-Huxley equations to a second-order system", *Biofizika* **18**, 506-511.

[89] Kuznetsov, Yu A. (2004). "*Elements of applied bifurcation theory*", Springer Verlag, Applied Mathematical Sciences, New York, **112**.

[90] Laing, C. R. & Coombes, S. (2005). "Mode locking in a periodically forced "ghostbursting" neuron model", *Int. J. Bifurcat. Chaos Appl. Sci. Eng.* **15**, 1433-1444.

[91] Laing, C. R. & Lord, G. (2010). "*Stochastic Methods in Neuroscience*", Oxford University Press, Oxford, Chapter 7.

[92] Laudanski, J., Coombes, S., Palmer, A. R. & Sumner, C. J. (2010). "Mode-locked spike trains in responses of ventral cochlear nucleus chopper and onset neurons to periodic stimuli", *J. Neurophysiol.* **103**, 1226-1237.

[93] Leung, L. S. & Yu, H. W. (1998). "Theta-frequency resonance in hippocampal CA1 neurons in vitro demonstrated by sinusoidal current injection", *J. Neurophysiol.* **79**, 1592-1596.

[94] Lin, K. K. (2006). "Entrainment and chaos in pulse-driven Hodgkin-Huxley oscillator", *SIAM, J. Appl. Dyn. Syst.* **5**, 179-204.

[95] Lindner, B. (2004). "Interspike interval statistics of neurons driven by colored noise", *Phys. Rev. E* **69**,022901-022905.

[96] Lindner, B., Garcia-Ojalvo, J., Neiman, A. & Schimansky-Geier, L. (2004). "Effects of noise in excitable systems", *Phys. Rep.* **392**, 321-424.

[97] Lindner, B. & Schimansky-Geier, L. (1999). "Analytical approach to the stochastic FitzHugh-Nagumo system and coherence resonance", *Phys. Rev. E* **60**, 7270-7276.

[98] Lindner, B. & Schimansky-Geier, L. (2000). "Coherence and stochastic resonance in a two-state system", *Phys. Rev. E* **61**, 6103-6110.

[99] Lindner, B. & Schimansky-Geier, L. (2001). "Transmission of noise coded versus additive signals through a neuronal ensemble", *Phys. Rev. Lett.* **86**, 2934-2937.

[100] Lindner, B., Schimansky-Geier, L. & Longtin, A. (2002). "Maximizing spike train coherence or incoherence in the leaky integrate-and-fire model", *Phys. Rev. E* **66**, 031916-031922.

[101] Liu, Y. H. & Wang, X. J. (2001). "Spike-frequency adaptation of a generalized leaky integrate-and-fire model neuron", *J. Comput. Neurosci.* **10**, 25-45.

[102] Llinas, R. R. (1988). "The intrinsic electrophysiological properties of mammalian neurons: Insights into central neuron system function", *Science*, **242**, 1654-1664.

[103] Llinas, R. R., Grace, A. A. & Yaromange, Y. (1991). "In vitro neurons in mammalian cortical layer 4 exhibit intrinsic oscillatory activity in the 10- to 50- Hz frequency range", *Proc. Natl. Acad. Sci. U.S.A.* **88**, 897-901.

[104] Longtin, A. (1993). "Stochastic resonance in neuron models", *Journal of Statistical Physics* **70**, 309-327.

[105] Longtin, A. (1997). "Autonomous stochastic resonance in bursting neurons", *Pys. Rev. E* **55**, 868-876.

[106] Longtin, A. (2000). "Effect of noise on the tuning properties of excitable systems", *Chaos, Solitons and Fractals* **11**, 1835-1848.

[107] Longtin, A. (2002). "Phase locking and resonances for stochastic excitable systems", *Fluct. and Noise Lett.* **2**, 183-211.

[108] Longtin, A., Bulsara, A. & Moss, F. (1991). "Time-interval sequences in bistability systems and the noise-induced transmission of information by sensory neurons", *Phys. Rev. Lett.* **67**, 656-659.

[109] Longtin, A. & Chialvo, D. R. (1998). "Stochastic and deterministic resonances of excitable systems", *Phys. Rev. Lett* **81**, 4012-4015.

[110] Mackay, R. S. & Tresser, C. (1986). "Transition to topological chaos for circle maps", *Physica D* **19**, 206-237.

[111] McCormick, D., Connors, B., Lighthall, J. & Prince, D. (1985). "Comparative electrophysiology of pyramidal and sparsely spiny stellate neurons in the neocortex", *J. Neurophysiol.* **54**, 782-806.

[112] McKean, H. P. (1970). "Nagumo's equation", *Advanced in Mathematics*, 209-223.

[113] Mickus, T., Jung, H-Y. & Spruston, N. (1999). "Properties of slow, cumulative sodium channel inactivation in rat hippocampal CA1 pyramidal neurons", *Biophysical Journal* **76**, 846-860.

[114] Middleton, J. W., Chacron, M. J., Lindner, B. & Longtin, A. (2003). "Firing statistics of a neuron model driven by long-range correlated noise", *Phys. Rev. E* **68**, 021920-021928.

[115] Moreno, R., de la Rocha, J., Renart, A. & Parga, N. (2002). "Response of spiking neurons to correlated inputs", *Phys. Rev. Lett.* **89**, 288101-288105.

[116] Moreno-Bote, R. & Parga, N. (2004). "Role of synaptic filtering on the firing response of simple model neurons", *Phys. Rev. Lett.* **92**, 028102-028106.

[117] Moreno-Bote, R. & Parga, N. (2004). "Response of a LIF neuron to inputs filtered with arbitrary time scale", *Neurocomputing* **58-60**, 197-202.

[118] Moreno-Bote, R. & Parga, N. (2005). "Membrane potential and response properties of populations of cortical neurons in the high conductance state", *Phys. Rev. Lett.* **94**, 088103-088106.

[119] Morris, C. & Lecar, H. (1981). "Voltage oscillations in the barnacle giant muscle fiber", *Biophys. J.* **35**, 193-2 .

[120] Müller, P. C. (1995). "Calculation of Lyapunov exponents for dynamical systems with discontinuities", *Chaos, Solitons and Fractals* **5** (9), 1671-1681.

[121] Nakada, K., Miura, K. & Hayashi, H. (2008). " Burst synchronization and chaotic phenomena in two strongly coupled resonate-and-fire neurons", *Int. J. Bifurcat. Chaos Appl. Sci. Eng.* **18**, 1249-1259.

[122] Nagumo, J. S., Arimito, S. & Yoshizawa, S. (1962). "An active pulse transmission line simulating nerve axon", *Proc. IRE* **50**, 2061-2070.

[123] Naundorf, B., Geisel, T. & Wolf, F. (2003). "The intrinsic time scale of transient neuronal responses", *arXiv: physics*, 0307135.

[124] Naundorf, B., Geisel, T. & Wolf, F. (2005). "Action potential onset dynamics and the response speed of neuronal populations", *J. Comput. Neurosci.* **18**, 297-309.

[125] Naundorf, B., Geisel, T. & Wolf, F. (2005). "Dynamical response properties of a canonical model for type-I membranes", *Neurocomputing* **65-66**, 421-428.

[126] Naundorf, B., Wolf, F. & Volgushev, M. (2006). "Unique features of action potential initiation in cortical neurons", *Nature* **440**, 1060-1063.

[127] Nykamp, D. Q. & Tranchina, D. (2000). "A population density approach that facilitates large-scale modelling of neural networks:

Analysis and an application to orientation tuning ", *J. Comput. Neurosci.* **8**, 19-50.

[128] Pakdaman, K., Tanabe, S. & Shimokava, T. (2001). "Coherence resonance and discharge time reliability in neurons and neuronal models", *Neural Networks*, **14**, 895-905.

[129] Perez, R. & Glass, L. (1982). "Bistability, period doubling bifurcations and chaos in a periodically forced oscillator", *Physics Letters*, **90A** (9), 441-443.

[130] Pike, F. G., Goddard, R. S., Suckling, J. M., Ganter, P., Kasthuri, N. & Paulsen, O. (2000). "Distinct frequency preferences of different types of rat hippocampal neurons in response to oscillatory input currents", *J. Physiol.* **529**, 205-213.

[131] Puil, E., Meiri, H. & Yarom, Y. (1994). "Resonant behaviour and frequency preference of thalamic neurons", *J. Physiol.* **71**, 575-582.

[132] Rescigno, A., Stein, R. B., Purple, R. L. & Poppele, R. E. (1970). "A neuronal model for the discharge patterns produced by cyclic inputs", *Bull. Math. Biophys.* **32**, 337-353.

[133] Ricciardi, L. M. (1977). "*Diffusion processes and related topics on biology*", Springer-Verlag, Berlin.

[134] Ricciardi, L. M. & Sato, S. (1990). In: Ricciardi, L. M. (Ed.), "*Lectures in applied mathematics and informatics*", Manchester University Press, New York.

[135] Richardson, M. J. E. (2007). "Firing-Rate response of linear and non-linear integrate-and-fire neurons to modulated current-based and conductance-based synaptic drive", *Phys. Rev. E* **76**, 021919-021934.

[136] Richardson, M. J. E. (2008). "Spike-train spectra and network response functions for non-linear integrate-and-fire neurons", *Biol. Cybern.* **99**, 381-392.

[137] Richardson, M. J. E. (2009). "Dynamics of populations and networks of neurons with voltage-activated and calcium-activated currents", *Phys. Rev. E* **80**, 021928-021934.

[138] Richardson, M. J. E., Brunel, N. & Hakim, V. (2003). "From subthreshold to firing-rate resonance", *J. Neurophysiol.* **89**, 2538-2554.

[139] Richardson, M. J. E. & Gerstner, W. (2005). "Synaptic shot noise and conductance fluctuations effect the membrane voltage with equal significance", *Neural Comput.* **17**, 923-947.

[140] Richardson, M. J. E. & Gerstner, W. (2006). "Statistics of subthreshold neuronal voltage fluctuations due to conductance-based synaptic shot noise", *Chaos* **16**, 026106-026116.

[141] Richardson, M. J. E. & Swarbrick. R. (2010). "Firing-rate response of a neuron receiving excitatory and inhibitory synaptic shot noise", *Phys. Rev. Lett.* **105**, 178102-178105.

[142] Rieke, F., Warland, D., de Ruyter van Steveninck, R. & Bialek, W. (1997). "*Exploring the neural code*", MIT Press, Cambridge, MA.

[143] Rinzel, J. (1985). "excitation dynamics: insights from simplified membrane models", *Fed. Proc.* **44**, 2944-2946 .

[144] Risken, H. (1989). "*The Fokker-Planck equation: Methods of solution and applications*", Berlin: Springer-Verlag.

[145] Rose, R. M. & Hindmarsh, J. L. (1989). "The assembly of ionic currents in a thalamic neuron. I. three dimensional model", *Proc. R. Soc. Lond (Biol.)* **237**, 267-288.

[146] Schilder, F., Peckam, B. B. (2007). "The computing Arnol'd tongue scenarios", *J. Comput. Phys.* **220**, 932-951.

[147] Seydel, R. (1988). "*From equilibrium to chaos: practical stability analysis*", Springer Verlag, New York.

[148] Silberberg, G., Bethge, M., Markaram, H., Pawelzik, K. & Tsodyks, M. (2004). "Dynamics of population rate code in ensemble of neocortical neurons", *J. Neurophysiol.* **91**, 704-709.

[149] Spiridon, M. & Gerstner, W. (1999). "Noise spectrum and signal transmission through a population of spiking neurons", *Netw. Comput. Neural Syst.* **10**, 257-272.

[150] Stein, R. B., French, A. S. & Holden, A. V. (1972). "The frequency response, coherence, and information capacity of two neuronal models", *Biophys. J.* **12**, 295-322.

[151] Tateno, T., Doi, S., Sato, S. & Ricciardi, L. M. (1995). "Stochastic phase lockings in a relaxation oscillator forced by a periodic input with additive noise: a first-passage-time approach", *Journal of Statistical Physics* **78**, 917-935.

[152] Tateno, T. (1998). "Characterization of stochastic bifurcations in a simple biological oscillator", *Journal of Statistical Physics* **92**, 675-705.

[153] Tateno, T. & Jimbo, Y. (2000). "Stochastic mode-locking for a noisy integrate-and-fire oscillator", *Physics Letters A* **271**, 227-236.

[154] Tonnelier, A. (2002). "The McKean's caricature of the FitszHugh-Nagumo model I. the space-clamped system", *SIAM J. Appl. Math.* **63**, 459-484.

[155] Tonnelier, A. & Gerstner, W. (2003). "Piecewise linear differential equations and integrate-and-fire neurons: insights from two-dimensional membrane models", *Phys. Rev. E* **67**, 021908(1-16).

[156] Tuckwell, H. C. (1988). "*Introduction to theoretical neurobiology*", Cambridge University Press.

[157] Van Vreeswijk, C. & Hansel, D. (2001). "Patterns of synchrony in neural networks with spike adaptation", *Neural Comput.* **13**, 959-992.

[158] Vibert, J. F. & Segundo, J. P. (1979). "Slowly adapting stretch-receptor organs: periodic stimulation with and without perturbations", *Biol. Cybern.* **33**, 81-95.

[159] Yoshino, K., Nomura, T., Pakdaman, K. & Sato, S. (1999). "Synthetic analysis of periodically stimulated excitable & oscillatory membrane models", *Phys. Rev. E* **59** (1), 956-969.

[160] Wang, X., & Buzsuaki, G. (1996). "Gamma oscillation by synaptic inhibition in a hippocampal interneuronal network model", *J. Nurosci.* **16**, 6402-6413

[161] Wang, X. J. (1998). "Calcuim coding and adaptive temporal computation in cortical pyramidal neurons" *J. Neurophysiol.* **79**, 1549-1566,.